December 2020

Novel Low Dimensional Sensors for Rapid Disease Diagnosis and Efficient Biomolecular Detection

Bipin Sharma
Clemson University, bipins@g.clemson.edu

Recommended Citation

Sharma, Bipin, "Novel Low Dimensional Sensors for Rapid Disease Diagnosis and Efficient Biomolecular Detection" (2020). *All Dissertations*. 2726.
https://tigerprints.clemson.edu/all_dissertations/2726

NOVEL LOW DIMENSIONAL SENSORS FOR RAPID DISEASE DIAGNOSIS AND EFFICIENT BIOMOLECULAR DETECTION

A Dissertation
Presented to
the Graduate School of
Clemson University

In Partial Fulfillment
of the Requirements for the Degree
Doctor of Philosophy
Physics

---

by
Bipin Sharma
December 2020

Accepted by:
Dr. Ramakrishna Podila, Committee Chair
Dr. Apparao M. Rao
Dr. Terri Bruce
Dr. Jian He

ABSTRACT

Nanomaterials have been used in diverse biosensing applications over the years for their unique properties compared to their 'bulk' counterparts. The quantum effects observed in nanomaterials of different dimensions have been exploited, in particular, for fluorescence sensing using surface plasmons. The present work is directed towards the understanding of these effects and the physics behind such plasmons and its application.

In the first chapter (Chapter 1), a succinct introduction to quantum confinement and fluorescence biosensors has been presented, followed by a brief overview of the applications of nanomaterials in biosensing. Chapter 2 focuses on the various analytical and characterization techniques used in this work. Chapter 3 describes the effects of shape on the plasmonic enhancement in silver nanoparticles. In chapter 4, the work on the development of a novel bio-sensing platform (AIDLuQ) has been outlined along with its use in ultra-sensitive detection of biomolecules. Building on chapter 4, the AIDLuQ platform was used for a real-life application in the detection of a cancer biomarker. This was supported with DFT simulations providing an insight into the electronic interactions between graphene and the quantum dots at the nano-scale. This has been described in chapter 5.

These findings lay the groundwork for further in-depth research to study the linear as well as non-linear optical interactions in nanoparticles in the vicinity of other nanoparticles, as elucidated in chapter 6.

DEDICATION

This work is dedicated to my family for their unconditional support in all my endeavors.

ACKNOWLEDGEMENTS

I would like to express my gratitude and appreciation to my advisor Dr. Ramakrishna Podila for his guidance and patience throughout. He helped me understand and appreciate nano-biophysics in a unique light and I will be thankful for his insights and mentorship. I would also like to thank Dr. Apparao Rao and my colleagues at the Clemson Nanomaterials Institute for their support. In particular, I would like to thank my colleagues and friends during my time here in Clemson in Dr. Lakshman Ventrapragada, Dr. Sai Sunil Mallineni, Dr. Yongchang Dong, Dr. Achyut Raghavendra, Dr. Fengjiao Liu, Dr. Anthony Childress, for helping me settle in and continue my work smoothly. I would like to thank Dr. Longyu (Jack) Hu, for his help and hard work in our project together. I would also like to show my appreciation to all my committee members – Dr. Jian He and Dr. Terri Bruce for their expertise, help and suggestions during my research work. Special thanks to Dr. Sriparna Bhattacharya and Herbert Behlow for always being there when I needed any help with my work. I would also like to acknowledge my friends who made my time in Clemson fun and enjoyable in Prakash, Wren, Shailendra, Lea, Komal, Subash, Soham; some of whom I had the pleasure of working with. Special mention to Courtney for being there during the difficult times and celebrating the good times with me. The most important thanks goes to my brother, Binay, for believing in my abilities and supporting me in getting here. And the most important of all, my family for always sticking by my side and believing in me.

TABLE OF CONTENTS

LIST OF TABLES

Table Page

LIST OF FIGURES

List of figures (contd.)

List of figures (contd.)

List of figures (contd.)

List of figures (contd.)

CHAPTER ONE

NANOMATERIALS FOR BIOSENSING

Nanomaterials are materials with at least one of the dimensions of the order of 1-100 nm. When one dimension of a 'bulk' material (say, thickness) is reduced to the nanoscale, the materials are called *quantum wells*. Similarly, if the materials are confined in two dimensions (say height and width), they resemble a wire and are hence named as *quantum wires*. When confined in all three dimensions, the nanomaterials are termed as *quantum dots*. The difference between the materials of different dimensions is depicted in **Fig. 1.1**. Depending on their chemical composition, these materials may or may not exhibit vastly different characteristics compared to their 'bulk' counterparts. For example, crystals in the nanometer regime may exhibit up to a 1000 °C difference in melting point compared to their bulk

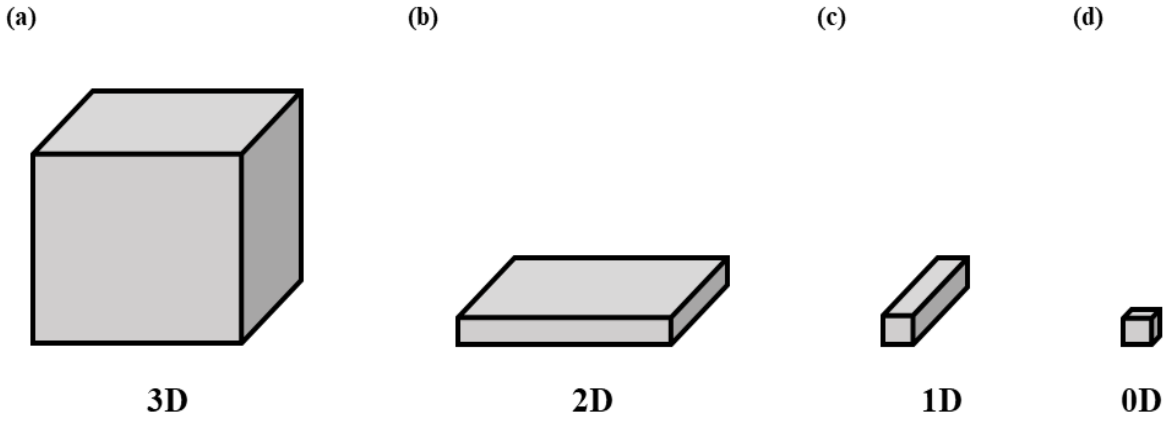

Fig. 1.1. (a) *Bulk* (3D) material. (b) When one dimension of this bulk material is reduced to the nanometer scale, it is called a *Quantum Well* (2D). (c) When two dimensions are reduced to nanometer scale, it is called a *Quantum Wire* (1D). (d) When all the dimensions are reduced to the nanometer regime, the material is now termed as a *Quantum Dot* (0D).

counterparts – a phenomenon directly related to drastic increase in surface area to volume ratio observed when transitioning from micro/macro-scale to nanoscale [1].

The main attraction of this field of nanotechnology is the flexibility and the potential to control the properties of nanomaterials (through the control of the size, shape, and morphology). This allows for a gamut of possibilities of applications in various fields. A more detailed introduction to nanomaterials can be found in Refs. [2], [3]. Some nanomaterials such as carbon nanotubes (CNTs), graphene, nanosized gold and silver have emerged as the panacea for addressing challenges in renewable energy, catalysis, lightweight composites etc.

In this work, as described in the following chapters, I leveraged unique properties of some nanomaterials (specifically, CNTs, graphene, Au and Ag NPs) for developing biosensors that are capable of detecting a wide range of biomarkers relevant for diseases such as cancer.

1.1 Fluorescence-based Biosensors

Biosensors are analytical devices that quantitatively detect the presence of specific analytes/biomolecules. The wide use of biosensors is attributed to the fact that they can convert biochemical processes into a measurable signal, thus enabling the use of such knowledge in clinical diagnostics, agriculture etc.[4]–[6]. The field of biosensor research has been rapidly growing with an approximate annual growth rate of 60% [7]. The major contributing field to biosensor research is the healthcare industry. The classification of biosensors is depicted in **Fig. 1.2** [7]. Biosensors are mainly composed of two components – a biocomponent part and a transducer part.

- The biocomponent part of a biosensor usually consists of a bioreceptor (e.g. an antibody) and a corresponding analyte (antigen that is to be detected) which is specific to the bioreceptor.
- The second and very important part of a biosensor is a transducer. A transducer is a device that converts a physical quality, or a change thereof, to an electrical/optical signal. In the case of a biosensor, the transducer part coverts the biochemical signal arising from the interaction of the analyte with the bioreceptor into an electrical/optical signal. This signal is then received by a detector which gives a readable/quantifiable output.

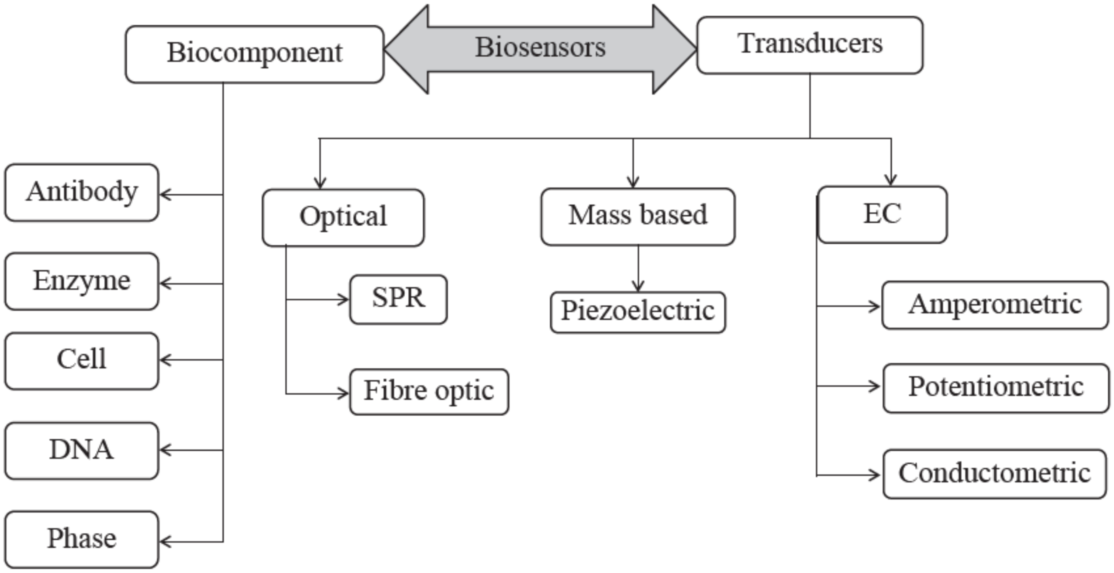

Fig. 1.2. Schematic of the classification of biosensors (DNA: Deoxyribonucleic Acid; SPR: Surface Plasmon Resonance; EC: Electrochemical)

Over the years, optical biosensors have gained immense popularity due to their small size, cost effectiveness and high sensitivity [7]. A large variety of optical biosensors have been used over this period of time including ellipsometry, spectroscopy (fluorescence, photoluminescence, etc.), optical waveguide structures and surface plasmon resonance (SPR) [8]–[10]. Chapter 2 discusses fluorescence, which is a phenomenon where a substance absorbs light of a particular wavelength and emits light of a different wavelength. Fluorescence–based biosensors are probes for the detection (or sensing) of specific bio-analytes where the transducer converts the interaction between analyte and antibody into an optical signal. Most of the work in this field is focused on fluorescent probes that exhibit a change in their fluorescence upon binding with the target molecule.

One field of application which has benefited heavily through the use of nanomaterials is biosensing [11]–[14]. Nano-biosensors use unique properties of nanomaterials to facilitate the detection of target molecules. Nanomaterials have been used to improve optical/electrochemical/mechanical properties of biosensors, thus making them more efficient and sensitive [15], [16].

1.2 Nanomaterials in Biosensors

Nanomaterials exhibit unique physical, chemical and biological properties and have been found to result in the enhancement of mechanical, electrochemical and optical properties of biosensors [15]. Nanomaterials exhibit a discrete electronic band structure due to their quantum size effect, which is similar to that of biomolecules [17], [18]. This similarity facilitates a seamless conjugation of the biomolecular systems with the nanomaterials, which in turn allows for the fabrication of ultrasensitive biosensors. The challenge is thus to develop nano-biosensors that exhibit high selectivity coupled with high sensitivity leading to highly efficient biomolecular sensing [19], [20].

Nanomaterials have been used in biosensors in different capacities over the years. The choice of nanomaterials is generally dependent on the biosensor application. Metal nanoparticles, carbon nanostructures (including graphene, carbon nanotubes (CNTs), etc.), magnetic nanoparticles, as well as other forms of nanomaterials find their use in biosensors [7]. Metal nanoparticles are often used for their plasmonic enhancement properties while oxide and semiconducting nanoparticles are used for immobilization, labeling, and tracing of biomolecules [21]–[23].

1.2.1 Metal Nanoparticle based biosensors:

Metal nanoparticles, mainly noble metal nanoparticles, including gold (Au), silver (Ag), platinum (Pt) and palladium (Pd) have been widely explored for cellular imaging, molecular diagnostics and therapeutics [24]–[26]. One of the main features of noble metallic nanoparticles is *surface plasmon resonance* (SPR). SPR (*or localized SPR*) is the enhancement of the local electric field by the collective oscillations of the conduction band electrons on the surface of metal nanoparticles. SPR enhances the electromagnetic field (light/fluorescence) and thus makes the optical biosensors more sensitive. This phenomenon has been further discussed in section 1.3. Gold nanoparticles (AuNPs) have received much attention among metal nanoparticles mainly because they have high surface energy, which can be used to immobilize biomolecules on their surface [27]. Additionally, silver nanoparticles (AgNPs) have been found to increase electrochemical activity, performance and mass transport and exhibit excellent biocompatibility [28], [29].

1.2.2. Nano metal-oxide based biosensors:

The applications of nanostructured metal oxides for biosensing applications are summarized in **Fig. 1.3**. Different nano-oxides of zinc (Zn), iron (Fe), tin (Sn), magnesium (Mg), zirconium (Zr), titanium (Ti), etc. have been used for their different properties such as biocompatibility, fast electron transfer, morphology, adsorption efficiency and so on [7].

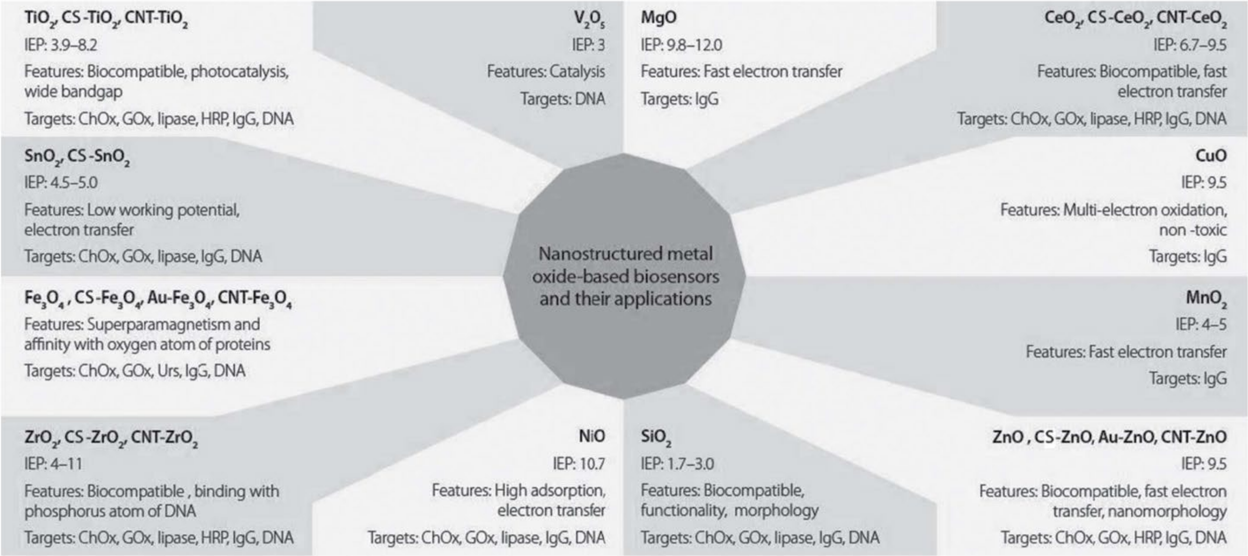

Fig. 1.3. Representation of different types of nanostructured metal oxides and their uses in biosensing applications (ChOx: cholesterol oxidase; CNT: carbon nanotube; CS: chitosan; HRP: horseradish peroxide; IEP: isoelectric point; IgG: Immunoglobulin G; Urs: urease) [7].

For the fabrication of an efficient biosensor, a suitable nanostructured metal oxide must be chosen as the binding of the biomolecule on the surface of the metal oxide nanoparticle has been known to affect the performance of the biosensor [30].

1.2.3. Carbon nanotube (CNT) based biosensors:

Ever since the discovery of carbon nanotubes (CNTs) in 1991 [31], [32], CNTs have been studied extensively for innumerable applications [32]. **Fig. 1.4(a)** shows the different forms of carbon nanostructures. Carbon has many allotropes and exhibits different nanoscale forms such as zero-dimensional (carbon dots, carbon onion, fullerene C_{60}, nanodiamonds), one-dimensional (carbon nanotubes – single-walled nanotube *(SWNT)*, multi-walled nanotubes *(MWNT)*) and two-dimensional (graphene, nanohorns) structures [33]. **Fig. 1.4(b)** shows how CNTs can be visualized as a rolled sheet of graphene, the two-dimensional nanostructure of carbon.

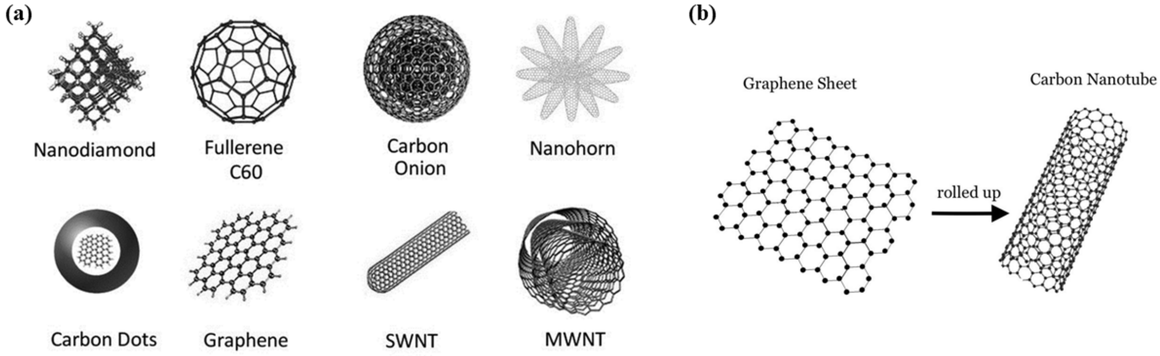

Fig. 1.4. (a) The nanostructures of carbon consisting of the well-known fullerenes (0D), carbon nanotubes (1D) and graphene (2D), among others [33]. **(b)** A simple schematic exhibiting the formation of a CNT from graphene.

In essence, a CNT is a single molecular nanomaterial formed by the seamless rolling of a single layer of carbon atoms into a 'molecular cylinder' [34]. SWNTs exhibit either semi-conducting or metallic nature depending upon their chirality (i.e., the direction in which a graphene sheet is rolled). Metallic SWNTs display extremely high electronic conductivity. Any change in their surface or environment can result in a drastic change in the conductivity – a prerequisite for any highly sensitive biosensor. CNTs are also easily functionalized with (*or immobilization of*) biomolecules, thereby providing a favorable substrate for biosensing. In fact, most of the work in biosensing using CNTs has been done using CNTs conjugated with other functional materials. Electrochemical (EC) CNT based biosensors and field-effect transistor (FET)-CNT biosensors are two of the most popular uses of functionalized CNTs for biosensing applications and have been used for the detection and quantification of cancer biomarkers, DNA, RNA, proteins and enzymes [35]–[41].

1.2.4. Graphene based biosensors:

Graphene, as discussed in the preceding subsection 1.2.3, is a two dimensional, one-atom-thick layer of carbon atoms derived from graphite, the *bulk* (macro) form. It is the thinnest material known to date [42], [43]. Since it is comprised of just the one layer of carbon atoms, the surface area of the material available is much higher because the monolayer can be accessed from both the top and the bottom. This available surface area is much higher in graphene (>2,600 m^2g^{-1}) compared to that of a CNT (~1,315 mg^{-1}) made up from rolling a graphene sheet of similar dimensions, since the inside (hollow part) of the CNT is partially unavailable [7].

Graphene has excellent thermal and electrical conductivity [44], [45], which is also evident in its exceptional promotion of electron transfer. It has been known to enhance direct electron transfer between enzymes and the electrodes/substrates. Graphene has also been previously used as a substrate in fluorescence quenching for ultrasensitive detection of aptamers [46], [47]. In these systems, graphene quenched the fluorescence signal due to the fluorescence resonance energy transfer from the fluorophore (dye) to the graphene substrate and the fluorescence quenching changed according to the change in the system's conformation [48], [49]. A more detailed description of quenching is presented in Ch. 4.

1.2.5 Quantum Dot based biosensors:

A quantum dot (QD) is a quasi-zero-dimensional material with all three dimensions (length, width, and thickness) confined to nanometer size. In a macroscopic or bulk semiconductor, excited with light, an electron-hole pair exists with a characteristic distance of an *exciton*

Bohr radius between them. In the nano-regime, if the size of the crystals of this semiconductor approaches the exciton Bohr radius, then the energy levels of the electrons are considered to be discrete. This phenomenon of size reduction of size is 'quantum confinement' which leads to zero dimensional materials (QDs) [50], [51]. QDs primarily find their use in biosensors as the fluorescing molecules (fluorophores), mainly because the absorption spectrum of a QD is dependent on its size.

QDs have numerous advantages over traditional fluorophores in that they show broad excitation, negligible photobleaching and high photochemical stability. In addition, the excitation spectrum for QDs is very broad while the emission wavelength is tunable via control over the size [50], [52], [53]. QDs also do not hinder Forster Resonance Energy Transfer (FRET). FRET is the radiationless transfer of energy from an excited fluorophore (*donor*) to another molecule (*acceptor*) through dipole-dipole coupling [54]. The most widespread of the biosensors using QDs are bioassays and bioprobes that use QDs as donors in FRET [54], [55]. The biorecognition agents that can be readily coupled to QDs for their use in biosensing are enzymes, antibodies, proteins, DNA, RNA, to name a few [56], [57].

1.3 Surface Plasmon Resonance (SPR) in Fluorescence Biosensors

1.3.1 Fluorescence biosensors:

Fluorescence is the emission of electromagnetic radiation (visible/invisible) of a certain wavelength by a molecule on excitation with a radiation of a shorter wavelength (higher energy). Therefore, fluorescence is quintessentially an optical phenomenon and a fluorescence-based biosensor an optical biosensor. Fluorescence will be discussed in further detail in Chapter 2, section 2.1 of this thesis. Despite being slightly more complex and more expensive, optical biosensors are better suited than EC biosensors for repetitive analysis, real-time monitoring and for continuous measurements of molecular binding events [58]. The two main types of biosensors are depicted in **Fig. 1.5**.

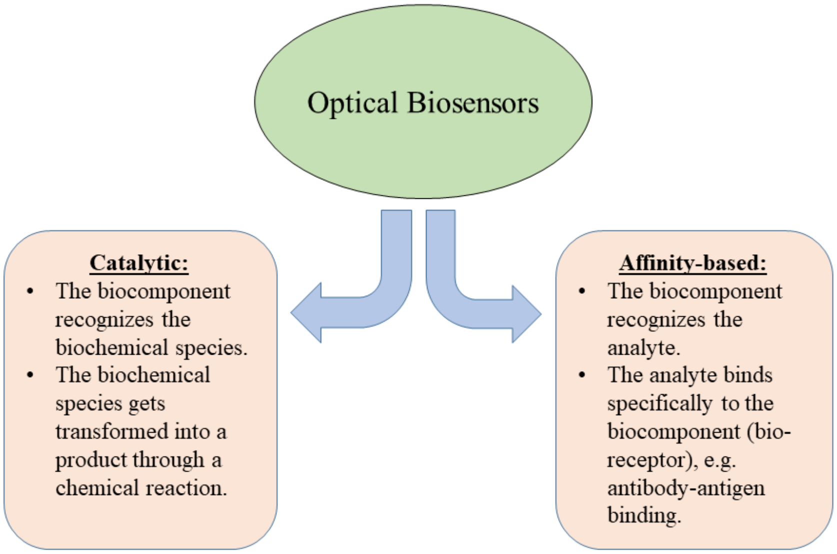

Fig. 1.5. The two main types of optical biosensors and their general mechanisms of operation.

Fluorescence is one of the most popular analytical approaches often applied in medical testing, biotechnology and drug discovery [8], [10], [59]. One of the major reasons for this popularity is the fact that many chemically synthesized fluorescent probes became available as early as the 1980s [10], [59]. These probes are molecules that specifically bind with the ligand while changing their fluorescent property in the process of binding. This provided ease and simplicity in biosensing, which is highly desirable [60].

Fluorescence biosensors can be classified into *label-free* or *label-bound* sensors [61]. **Fig. 1.6** discusses the basic differences between the two types.

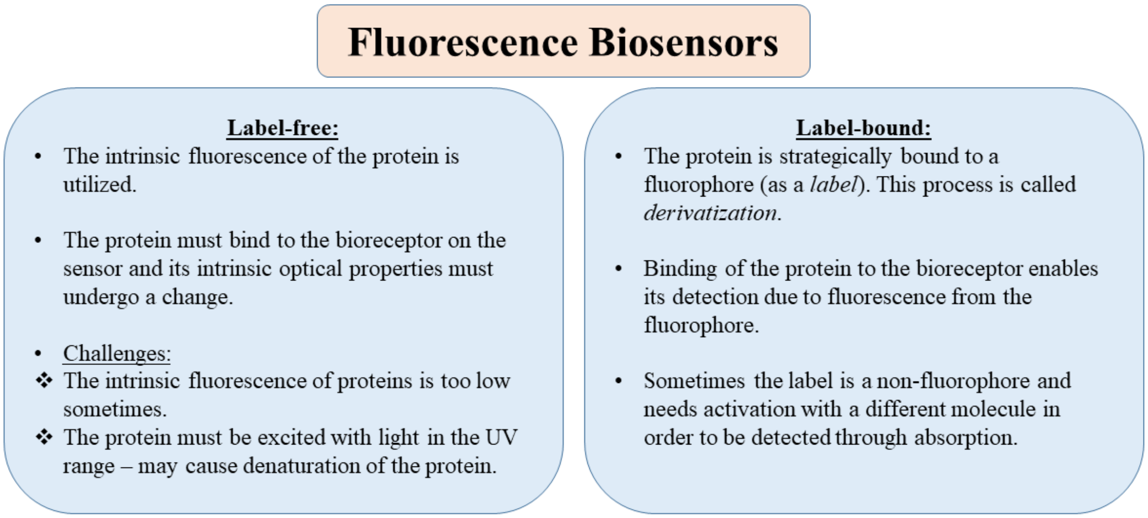

Fluorescence Biosensors

Label-free:

- The intrinsic fluorescence of the protein is utilized.
- The protein must bind to the bioreceptor on the sensor and its intrinsic optical properties must undergo a change.
- Challenges:
  - ❖ The intrinsic fluorescence of proteins is too low sometimes.
  - ❖ The protein must be excited with light in the UV range – may cause denaturation of the protein.

Label-bound:

- The protein is strategically bound to a fluorophore (as a *label*). This process is called *derivatization*.
- Binding of the protein to the bioreceptor enables its detection due to fluorescence from the fluorophore.
- Sometimes the label is a non-fluorophore and needs activation with a different molecule in order to be detected through absorption.

Fig. 1.6. Classification of fluorescence biosensors based on the dependence on a label (fluorescent or otherwise) (UV: ultraviolet).

Label-free fluorescence biosensors are mainly dependent on changes in optical properties of proteins upon binding the bioreceptor. This change is normally observed in absorbance, polarization, emission or luminescence decay time [60]. *Label-bound* fluorescence biosensors utilize *derivatization* of the proteins with a high quantum-yield fluorophore [59]. Quantum Yield (QY) of a fluorophore may be understood as the ratio of number of photons emitted by the fluorophore to the number of photons absorbed.

$$QY = \frac{no. of\ photons\ emitted}{no. of\ photons\ absorbed} \tag{1}$$

A detailed description of QY in terms of decay rates is presented later in this section. Essentially, a 'high quantum-yield' fluorophore will have a high number of photons emitted per absorbed photon. These fluorophores can thus be excited with a lower energy (higher wavelength) light. This, in turn, allows for the control of the analytical wavelength which needs to be monitored for biosensing [8], [61].

1.3.2 Surface Plasmon Resonance:

Surface Plasmon Resonance (SPR) is a phenomenon of the collective oscillations of the valence electrons on the surface of the metal (*plasmon* – a quantum of plasma oscillation) upon excitation by an incident electromagnetic radiation [62]. In thin (~50 nm) metal films, the plasmons are of the propagating kind and are thus termed as *surface plasmon polaritons* [63]–[65]. However, in metallic nanostructures, where the electron clouds are bound to each individual particle, we observe something called *localized surface plasmon resonance* (LSPR) [66]–[68]. A schematic illustration is presented in **Fig. 1.7**.

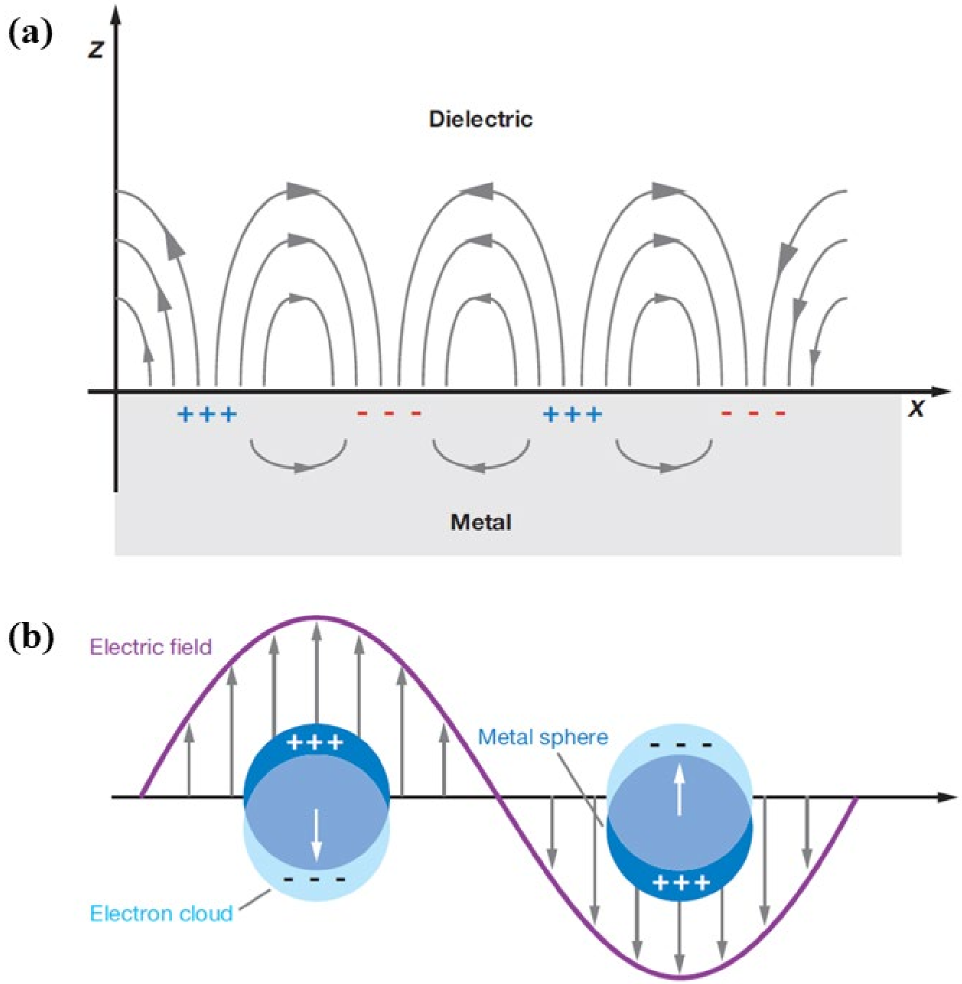

Fig. 1.7. Schematic representations of (a) surface plasmon polaritons (propagating); and (b) a localized surface plasmon (LSPR) showing the oscillation of the electron cloud localized around a spherical nanoparticle [69].

1.3.2.1. A brief overview of SPR:

The details of the derivations of the equations used in this section can be found in the work by Willets *et al.* [69]. Consider a spherical metal nanoparticle of radius 'a' that is exposed to a z-polarized light of wavelength 'λ' where a is significantly smaller than the incident wavelength, i.e., $(a/\lambda) < 0.1$ (**Fig. 1.8**).

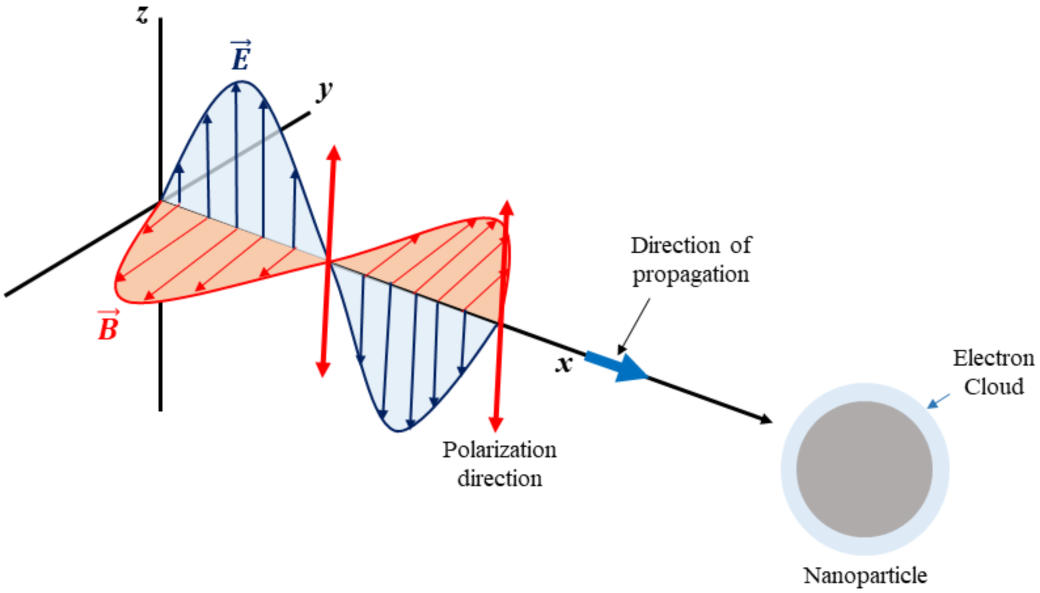

Fig. 1.8. Schematic illustration of the case of a *z*-polarized light wave incident on a metal nanoparticle experiencing a localized surface plasmon resonance ($\vec{E}$: electric field; $\vec{B}$: magnetic field).

In this limit, the electric field around the nanoparticle appears static, thus allowing us to solve for the electric field using Maxell's equations via the application of a quasi-static approximation [70], [71] to be:

$$E_{out}(x,y,z) = E_0\hat{\mathbf{z}} - \left[\frac{\varepsilon_{in} - \varepsilon_{out}}{\varepsilon_{in} + 2\varepsilon_{out}}\right] a^3\, E_0 \left[\frac{\hat{z}}{r^3} - \frac{3z}{r^5}(x\hat{\mathbf{x}} + y\hat{\mathbf{y}} + z\hat{\mathbf{z}})\right] \qquad (2)$$

Here, ε_{in} is the dielectric constant of the metal nanoparticle, ε_{out} is the dielectric constant of the outside (external environment) of the metal nanoparticle, E_{out} is the electric field outside the nanoparticle, r is the magnitude of the vector from the center of the nanoparticle to the point of observation ($r < a$: inside the nanoparticle; $r > a$: outside the nanoparticle).

The term $\left[\frac{\varepsilon_{in}-\varepsilon_{out}}{\varepsilon_{in}+2\varepsilon_{out}}\right]$ determines the plasmon resonance condition for the nanoparticle as ε_{in} is strongly dependent on the excitation wavelength. When $\varepsilon_{in} \approx -2\varepsilon_{out}$, the electric field is enhanced relative to the incident field [69]. Incidentally, for nanoparticles of noble metals such as gold (Au) and silver (Ag), this condition is easily satisfied in the visible spectrum, thus enabling their use in surface-enhanced spectroscopic systems. It must be noted that **Equation (2)** above also highlights the field enhancement by the nanoparticle is inversely related to the distance (*r*) from the nanoparticle. Thus, localized surface plasmon resonance is essentially low-dimensional phenomenon (usually, $r < 20\ nm$). In addition, the second term in **Equation (2)** is strongly dependent on the size of the nanoparticle (*a*) – larger the size, larger is the second term, thus smaller the E_{out}.

Extinction spectrum of an object is defined as the addition of absorption spectrum of the object to its elastic light-scattering spectrum [69]. The extinction spectrum of a metal sphere is calculated using the following relation [72], [73]:

$$E(\lambda) = \frac{24\,\pi^2 N a^3 \varepsilon_{out}^{\frac{3}{2}}}{\lambda \ln(10)} \left[\frac{\varepsilon_i(\lambda)}{(\varepsilon_r(\lambda)\ +\ \chi\varepsilon_{out})^2 +\ \varepsilon_i(\lambda)^2}\right] \tag{3}$$

Here, ε_i and ε_r are the imaginary and the real part of the dielectric constant. Needless to say, both ε_i and ε_r are invariantly part of the term ε_{in} described earlier. Also, quite evidently, both these terms are also strongly dependent on the incident wavelength of light (λ). *N* in the **Equation (3)** is an approximation of the number of finite polarizable elements that the particle in question is made of that are capable of interacting with the applied electric field *E* and χ is the extinction coefficient.

The localized SPR (LSPR) extinction (or scattering) wavelength maximum, λ_{max} is affected by the refractive index of the material (n) and its immediate surroundings. This means that if there is a change in the local environment which leads to a change in the refractive index of the metal nanoparticle, it causes a shift in λ_{max} as well. This change, which can be in the form of adsorption of some species on to the surface of the material, results in a changed λ_{max} expressed using the following relationship [74], [75]:

$$\lambda_{max} = m\Delta n\left[1 - \exp\left(\frac{-2d}{l_d}\right)\right] \tag{4}$$

Here, m is the 'bulk' refractive index of the nanoparticle; Δn is the change in the refractive index induced by the change in the surroundings of the nanoparticles; d is the thickness of the adsorbed layer and l_d is the exponential decay constant of the electromagnetic field [69]. This is the basis of the sensing experiments using LSPR which utilize the shift in the wavelength on the introduction of the target species.

In addition to the above stipulations for the observation of SPR in nanoparticles, there are other conditions that need to be satisfied in order to observe SPR in thin films (or *nano* films) of metals. As discussed earlier, the real and imaginary parts of the refractive index ($\hat{n}$) of the metal plays an important part in the calculation of surface plasmons [76], [77], which are dependent on the extinction coefficient (χ), the dielectric constant (ε), the conductivity (σ), and the permeability (μ). This co-dependence can be seen through the following relations [78]:

$$\hat{n} = n + ik = n(1 + i\kappa) = \sqrt{\mu\hat{\varepsilon}} \tag{5}$$

$$\hat{\varepsilon} = \varepsilon_r + i\varepsilon_i \tag{6}$$

$$\varepsilon_i = \frac{4\pi\sigma}{\omega} \tag{7}$$

$$\chi = \frac{4\pi\kappa}{\lambda} \tag{8}$$

Here, n is the real part of the refractive index, k the imaginary part; and κ is a derivative form of the imaginary part of the refractive index and is called the *attenuation index*. The common configurations for the excitation of surface plasmons are shown in **Fig. 1.9**. In the *Kretschman* configuration [79], the incident p-polarized light passes through a prism (a dense dielectric medium) of refractive index n_1 which is followed by generation of surface plasmon in a thin metal layer of thickness d with a complex refractive index of $(n_2 + ik_2)$. The outer medium is a dielectric with a refractive index n_3.

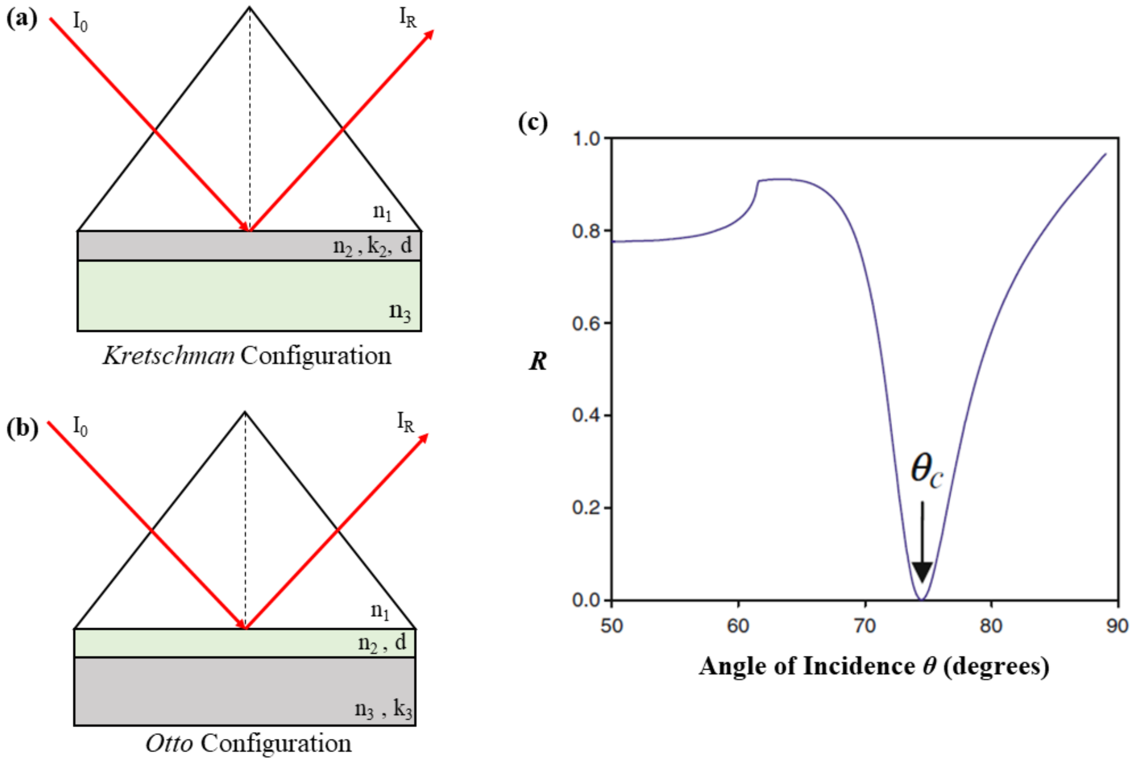

Fig. 1.9. The common surface plasmon excitation configurations: **(a)** Kretschman configuration, in which the metal film lies between two dielectrics of refractive indices n_1 and n_3; **(b)** Otto configuration, in which the metal film is on the 'outside' of two adjacent dielectrics of refractive indices n_1 and n_2; **(c)** a plot of intensity of reflectivity (***R***) with respect to the angle of incidence. A strong decrease in the intensity occurs at an angle called the *critical angle* ($\boldsymbol{\theta_c}$), which is due to SPR [78].

In the *Otto* configuration [80], a metal layer with a complex refractive index $(n_3 + ik_3)$ is present on the 'outside' of two adjacent dielectrics of different refractive indices n_1 and n_2, where $n_2 < n_1$ and the thickness of the dielectric with refractive index of n_2 is d. Since $n_2 < n_1$, total internal reflection (TIR) takes place at a *critical angle* (θ_c) and the evanescent field of the incident light is absorbed by the metal layer on the outside, which excites the surface plasmons [78].

1.3.3 Applications of SPR in fluorescence biosensors:

An ideal fluorophore is a molecule that absorbs a photon of a certain wavelength λ_1 and emits another photon of a higher wavelength λ_2, such that $\lambda_1 < \lambda_2$, exhibiting a high quantum yield (QY) while doing so. The fluorescence emission rate Γ_{em} is dependent on the rate of excitation Γ_{exc}, the radiative decay rate Γ and the intrinsic non-radiative decay rate k_{nr}, and can be expressed as [81]:

$$\Gamma_{em} \propto \Gamma_{exc} \frac{\Gamma}{\Gamma + k_{nr}} \tag{9}$$

It is vital to note that QY can be defined in terms of the radiative and non-radiative decay rates as:

$$QY = \frac{\Gamma}{\Gamma + k_{nr}} \tag{10}$$

QY is usually in the range of 0.5 – 0.9 the lifetime (τ), which is expressed as $\tau = \frac{1}{\Gamma + k_{nr}}$, generally lies in between 1 – 10 ns for the most commonly used organic chromophores [81].

As is evident from **Equation (9)**, the rate of emission of the fluorophore is directly proportional to the excitation rate. This rate of excitation Γ_{exc} is, in turn, proportional to the intensity of the electromagnetic field used for excitation of the fluorophore. By placing the fluorophore within the limits of surface plasmon enhanced field, Γ_{exc} can be increased significantly, which leads to the enhancement of the emission rate Γ_{em}, and thus, the emission intensity of the fluorophore [81].

On placement of a fluorophore in close proximity to a plasmonic thin film, a strong coupling of the emitted light from the fluorophore to the surface plasmons is observed for distances up to a few hundred nanometers from the metal surface [82]. The advantage of such a coupling of fluorescence emission surface plasmon is that it provides a highly directional fluorescence emission [81]. In addition, this coupling allows for orders of magnitude of increase in the fluorescence signal [83]. Thus, SPR has been found to be immensely useful in fluorescence biosensing for ultrasensitive detection of biomolecules and other biological entities.

CHAPTER TWO

CHARACTERIZATION AND ANALYTICAL METHODS

‘Characterization’ is a broad term referred to the analysis and quantification of the physical and chemical properties of materials. Characterization of materials can involve either of the macroscopic or microscopic properties and is a powerful tool in understanding the science behind processes in these domains. Characterization techniques can usually be divided into *three* major categories as highlighted by **Fig. 2.1**: (i) Microscopic techniques, (ii) Spectroscopic techniques, and (iii) Macroscopic analysis techniques.

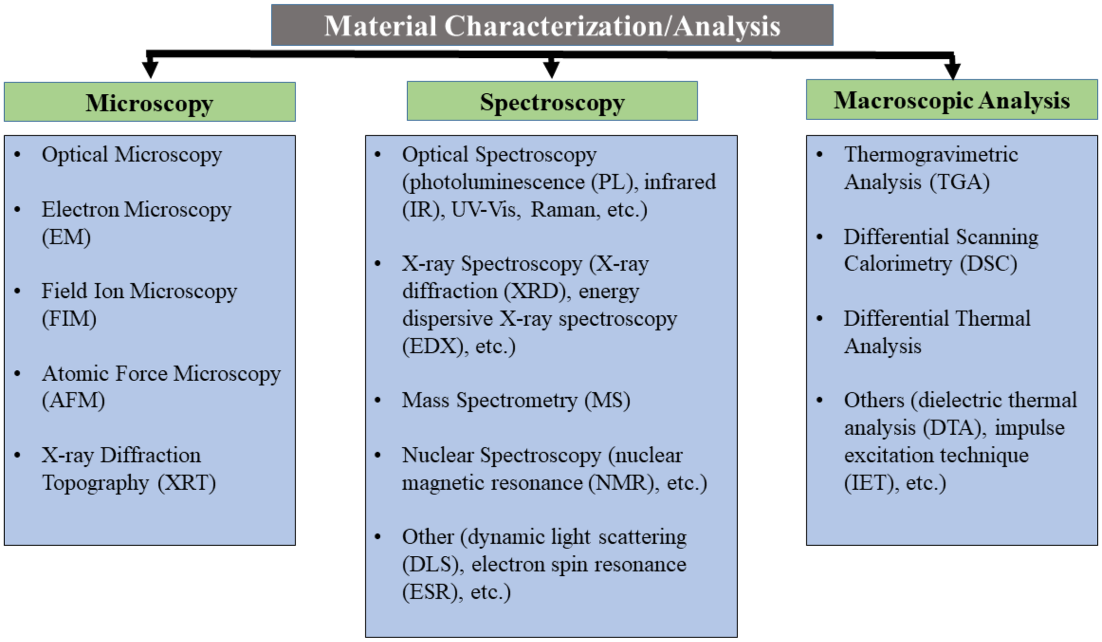

Fig. 2.1. The most popular forms of materials characterization and analysis tools and techniques.

Microscopic techniques are generally centered around the ‘visual’ characterization of materials. Optical microscopy techniques use light-based microscopes to get microscopic images of the size and shape of materials in the microscopic domain. The most common example is the imaging/visualization of stained and unstained cells and cell organelles. Electron microscopy techniques (scanning electron microscopy (SEM), transmission electron microscopy (TEM), scanning tunneling microscopy (STM)) use the diffraction, scattering and tunneling of electrons to provide information about the size, shape and morphology of nanomaterials. Similarly, atomic probe microscopy (APM) and atomic force microscopy (AFM) probe the surface features of materials at the nano scale.

Spectroscopy is associated with light-matter interaction, i.e., absorption, scattering or emission (spontaneous or induced) of electromagnetic radiation by matter (atoms or molecules) [84]. This electromagnetic radiation can be of different wavelengths including infrared (IR), ultraviolet (UV), visible range, X-rays, gamma radiation, etc. The output from the detector after any event of light-matter interaction is known as the spectrum and this spectrum helps in understanding the physical and chemical components (and/or reactions) of a system. A spectrum is generally specific to a certain element/compound and is thus useful for elemental and chemical composition analysis. For example, the Raman spectrum has specific peaks for specific types of phonons – which in turn are specific to an element or a compound. Thus, the peaks of the Raman spectrum of an unknown sample can be analyzed to discover its identity.

In addition to the microscopic and spectroscopic methods of analysis, we also use the *macroscopic* forms of analysis. It must be noted that these macroscopic forms of analysis are not size-dependent – they apply to microscopic and macroscopic (or bulk) materials alike. These techniques have more to deal with the macroscopic properties of substances, for example, differential scanning calorimetry (DSC) is used for the determination of heat capacity of an unknown (or known) sample, regardless of whether the substance is in bulk form of nano.

This chapter will mainly focus on some spectroscopic and microscopic techniques that were used in the chapters to follow. A brief overview is provided of the physical principles of each of the methods/techniques used followed by their instrumentation. In section 2.1, Fluorescence spectroscopy is discussed, followed by Raman spectroscopy in 2.2, Scanning Electron Microscopy (SEM) in 2.3 and Transmission Electron Microscopy (TEM) in 2.4.

2.1 Fluorescence Spectroscopy

The phenomenon of fluorescence is schematically demonstrated using a simple Jablonski diagram in **Fig. 2.2**. A *Jablonski* diagram is a form of representation of electronic transitions, first developed by A. Jablonski [85]. The diagram demonstrates the pathway of a ground-state electron as it absorbs a photon, goes to an excited electronic state and then returns back to the ground state as it releases energy in emissive and/or non-emissive processes.

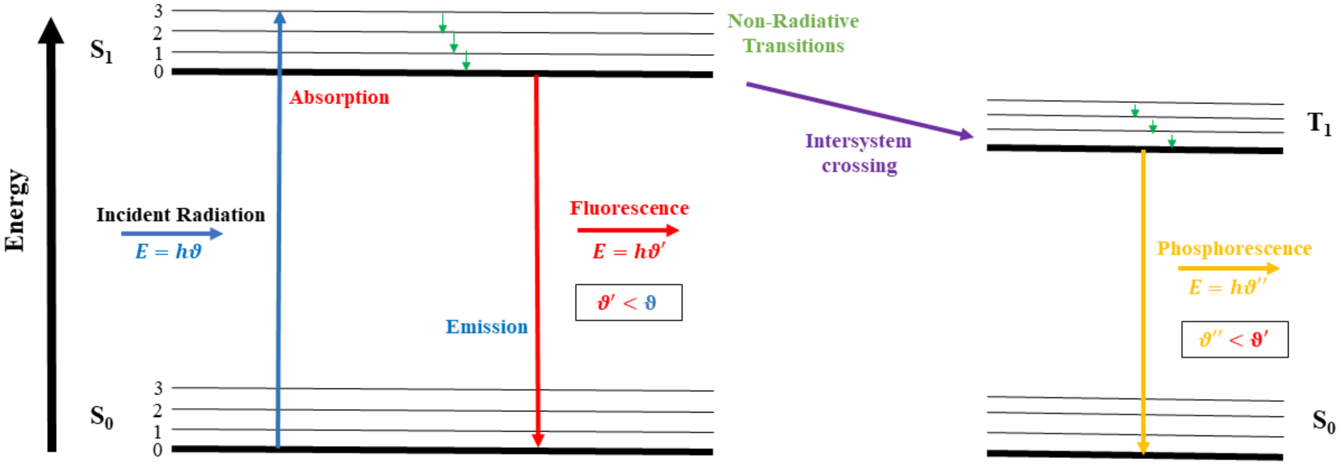

Fig. 2.2. A Jablonski diagram featuring the electronic transitions in fluorescence.

The phenomenon may be described as follows:

- An electron in the S_0 ground singlet electronic level absorbs the energy ($E = h\vartheta$) from a photon of wavelength λ (and frequency ϑ; $\vartheta = c/\lambda$, where c is the speed of light in vacuum). A *singlet* state is the electronic state of a molecule wherein all the electrons are paired, thus leaving the net angular momentum to be zero.

- This absorption of energy takes the electron to a higher (excited) energy state S_1. This excited molecule then dissipates part of its energy to return to the lowest energy state of the excited state S1. This transition happens via the release of energy through *non-radiative* means such as lattice vibrations, heat dissipation, etc.

- The molecule then undergoes *emissive* transition, wherein it emits a photon and ‘relaxes’ back to the ground state S0. Since some of the energy was lost in the non-radiative processes, the energy ($h\vartheta'$) of this emitted photon is lesser than the energy of the excitation (incident) photon ($h\vartheta$). This also means that the wavelength (λ) of the emission is longer than the wavelength (λ') of excitation.

The excited molecule can also transfer some of its energy to the molecules nearby (called collisional quenching) or to molecules at some distance (energy transfer) thereby exhibiting no fluorescence at all. Another common scenario is for molecules to jump from the lowest energy state of the excited state S1 to an excited triplet state T1, with energy lower than S1. This phenomenon is called *inter-system crossing*. A *triplet state* is one in which there are two unpaired electrons – an excited triplet state is extremely unstable energetically. In the case that the molecule goes to this unstable triplet state, it will de-excite through the following mechanisms to get to the ground state:

- Emission of a photon of an even smaller frequency (ϑ''; $\vartheta'' < \vartheta' < \vartheta$) through a process known as *phosphorescence*.

- Non-radiative dissipation of energy in the form of heat, lattice vibrations, etc.

- Transfer of energy through quenching or energy transfer.

In both these processes, the common factor is that both emission wavelengths seem to have 'shifted' to the right, i.e., the emission wavelengths are longer than the excitation wavelength. This shift of emission with respect to the excitation wavelength is called a *red shift* or, more formally, a *Stokes shift*. A typical fluorescence spectrum in comparison to the incident radiation is shown in **Fig. 2.3**.

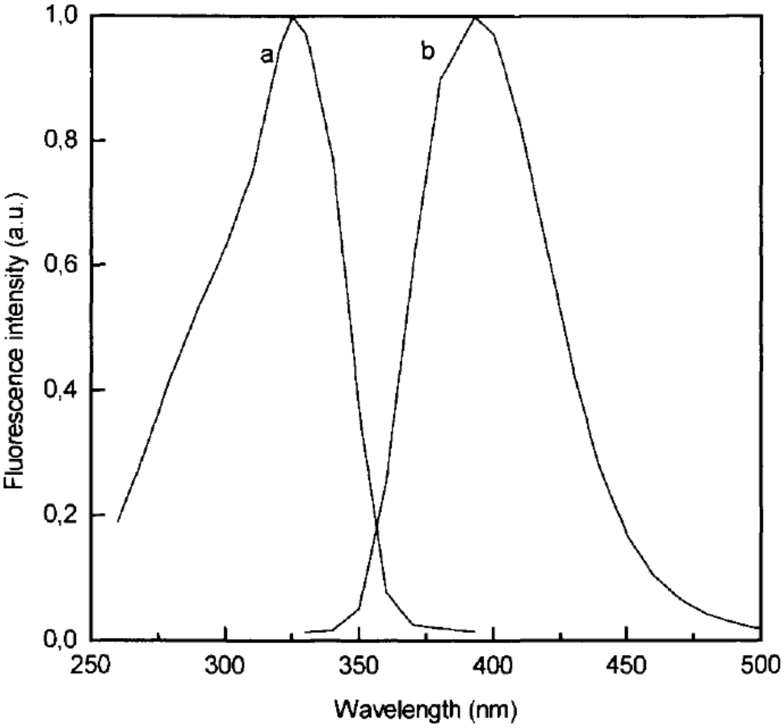

Fig. 2.3. A normalized spectrum of **(a)** excitation and **(b)** emission fluorescence of 7-amino-4-methylcoumarin-DEVD complex (DEVD: Aspartic Acid – Glutamic Acid – Valine – Aspartic Acid) [86].

2.1.1. Instrumentation (Spectrofluorometer):

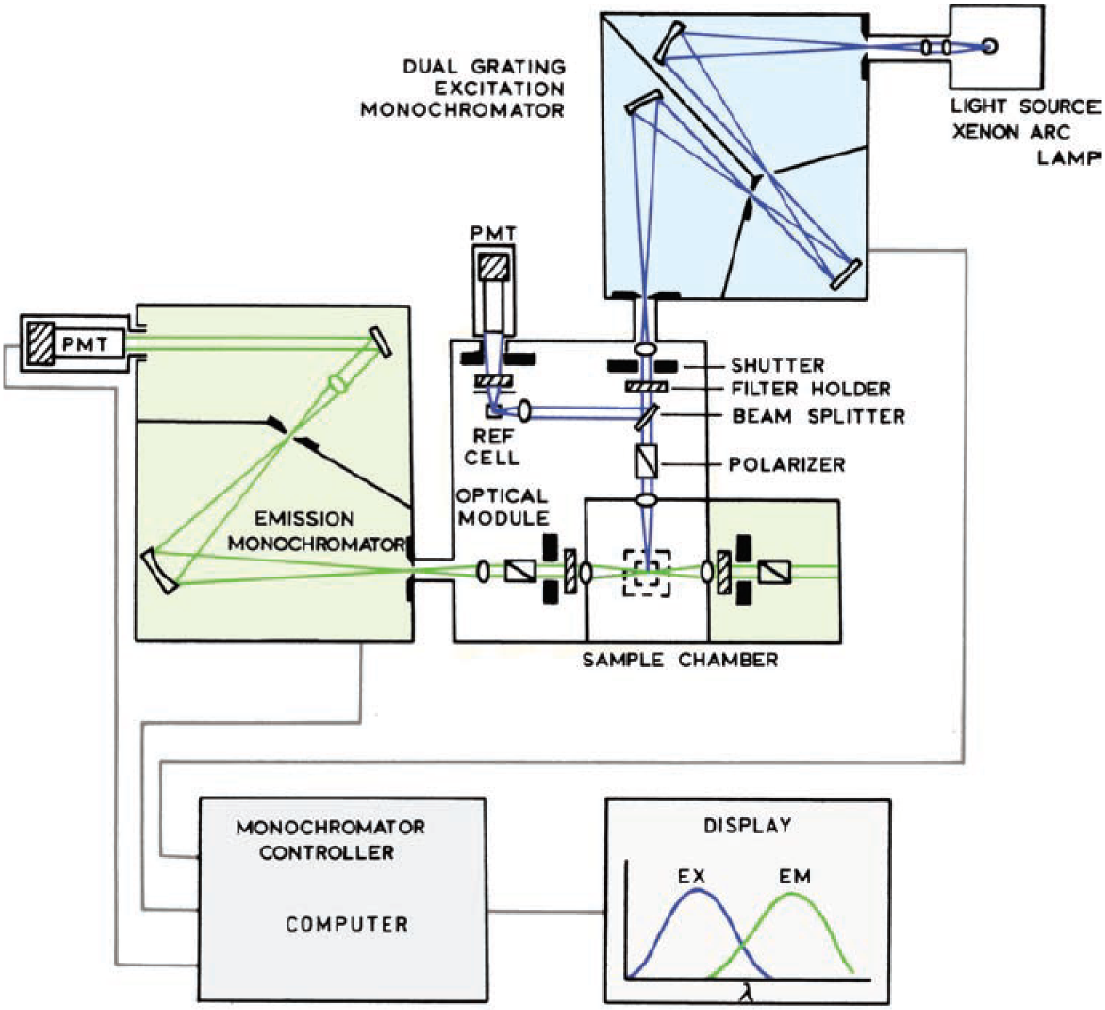

Fig. 2.4. A schematic diagram of the instrumentation of a spectrofluorometer [87]. (EX: excitation spectrum; EM: emission spectrum).

The schematic illustration of a typical spectrofluorometer is shown in **Fig. 2.4**. The light source (a Xenon arc lamp in this example) is used such that it acts as a source with high intensity light over a range of wavelengths. This light then passes through an 'excitation monochromator' which helps in resolution of wavelengths. The light then passes through a shutter, which helps in reduction of stray light entering the chamber with the sample in it. The beam splitter reflects ~ 4% of the incident light on to a reference cell which contains a stable reference fluorophore. The emission from this reference cell is measured using a photomultiplier tube (PMT) detector.

The light that passes through (without reflection) the beam splitter then goes through a polarizer (optional; used in specific cases) before impinging on the sample in the sample chamber. The emitted photons from the sample go through a filter (for removal of the excitation wavelength from the collected light), followed by an 'emission monochromator' and are finally detected by another PMT.

Recent trends are based on movement towards a more compact form of spectrofluorometers. For example, the Xenon arc lamp and the 'excitation monochromator' can both be replaced with a laser which ensures wavelength control and polarized, coherent light with high intensity. The 'emission monochromator' can also be removed from the system and just filters (band pass, high/low pass, etc.) are used to remove the unwanted wavelengths, including the excitation laser wavelength. This allows for a much simpler form of instrumentation, which can be visualized as shown in **Fig. 2.5**.

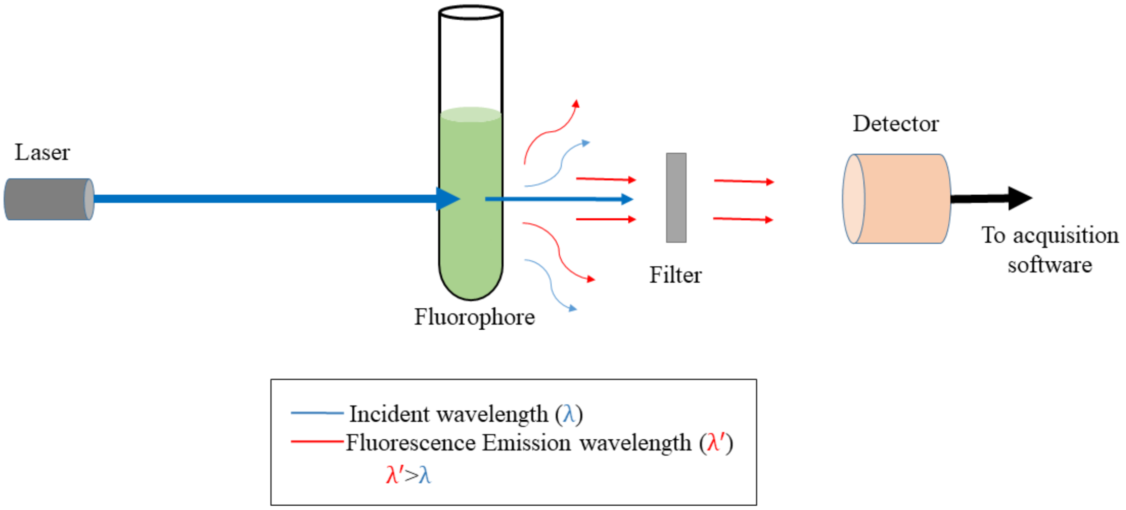

Fig. 2.5. Simplified schematic illustration of the a spectrofluorometer that uses a laser as the light source. The filter weeds out the elastically (Rayleigh) scattered radiation, which is of the same wavelength as the incident radiation (blue color waves in the figure) and allows only higher wavelengths (red) to pass through, which are picked up by the detector.

2.2 Raman Spectroscopy

Raman effect is the phenomenon of inelastic scattering of light by matter. This effect was discovered by Sir C. V. Raman in 1928 [88], [89], at a time when limited instrumentation was available. He used sunlight as the light source, a telescope as the collector and his eyes as the detector [90]. What makes this discovery ever so remarkable is that it is an extremely feeble phenomenon to detect – one in every ~ 10^5 photons undergo Raman scattering [90].

Fig. 2.6 shows the energy levels of the simple example of a diatomic molecule including the transitions it undergoes upon absorption of energy.

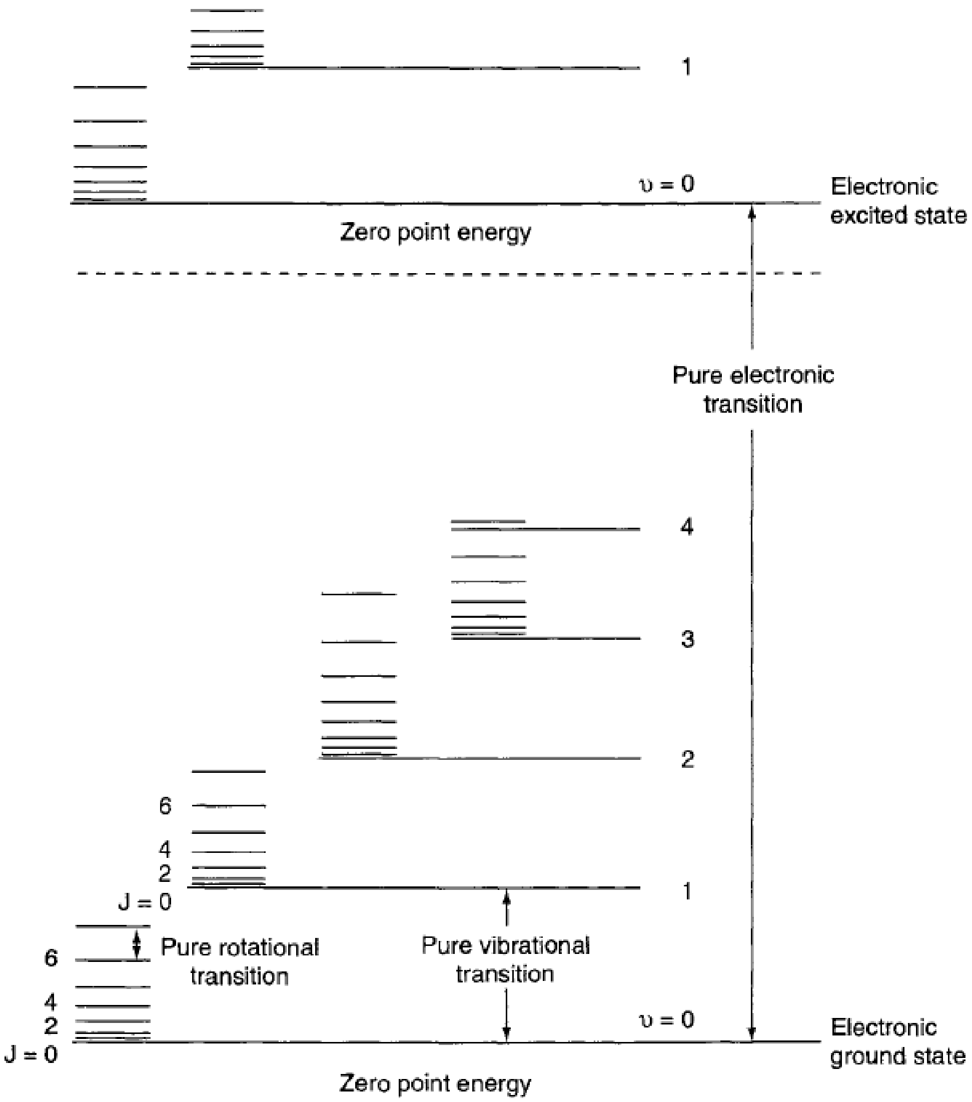

Fig. 2.6. Energy levels and transitions of a diatomic molecule (the spacings between the levels may have been modified for better visualization) [90].

In a molecule with two or more atoms, there is splitting of the energy levels and thus we end up with each electronic state having several vibrational states associated with it and each vibrational state having a few rotational states associated with it. As discussed in section 2.1, a purely electronic transition on the absorption of a photon is responsible for fluorescence and phosphorescence. A molecule may also absorb some energy from a photon and undergo a purely vibrational or a purely rotational transition. The energy (*wavenumber*) range associated with different types of spectroscopies and the types of energy transitions are listed in **Table 2.1**. Wavenumber ($\bar{\vartheta}$) is a quantity associated with electromagnetic radiation and is defined mathematically as

$$\bar{\vartheta} = \frac{1}{\lambda} \tag{11}$$

Here, λ is the wavelength of the electromagnetic radiation in question. But, the quantity λ is related with the frequency (ϑ) of the radiation via the expression $\lambda = c/\vartheta$ (or, $\vartheta = c/\lambda$). Thus, we can relate the frequency to the wavenumber as follows:

$$\vartheta = \frac{c}{\lambda} = c\bar{\vartheta} \tag{12}$$

The quantity $\bar{\vartheta}$ $(= 1/\lambda)$ has the units of cm^{-1}. From the **Equation 12**, it can be seen that a simple constant of proportionality (c) relates the wavenumber and the frequency. Hence, frequency and wavenumber are generally used interchangeably.

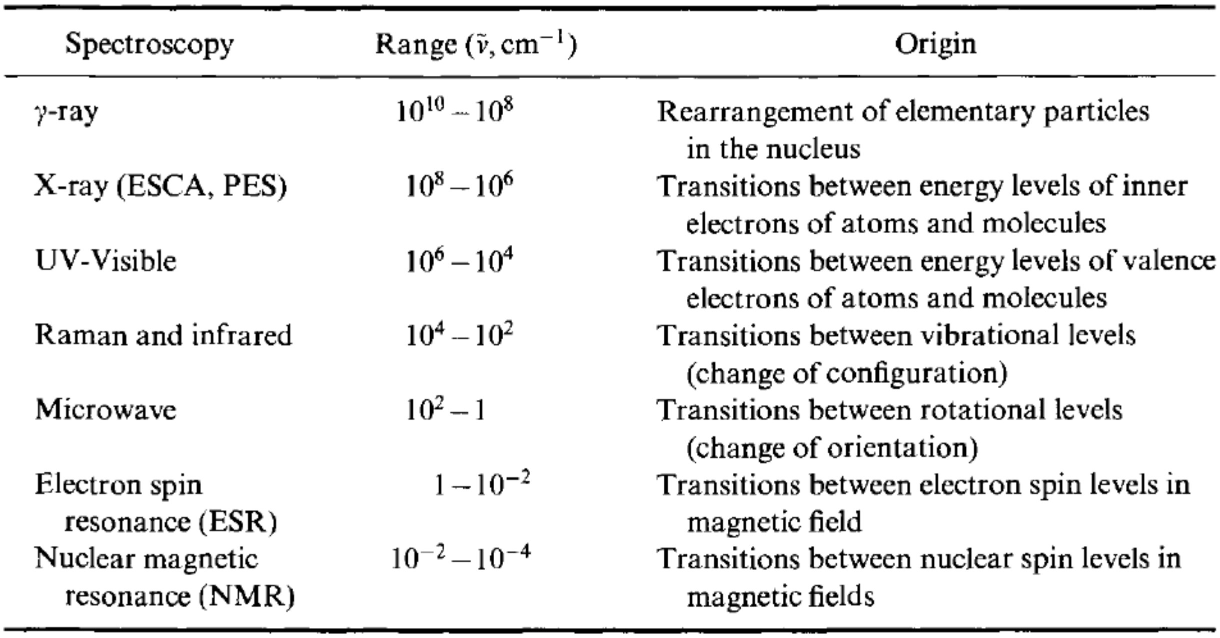

Spectroscopy	Range ($\tilde{\nu}$, cm^{-1})	Origin
γ-ray	$10^{10} - 10^{8}$	Rearrangement of elementary particles in the nucleus
X-ray (ESCA, PES)	$10^{8} - 10^{6}$	Transitions between energy levels of inner electrons of atoms and molecules
UV-Visible	$10^{6} - 10^{4}$	Transitions between energy levels of valence electrons of atoms and molecules
Raman and infrared	$10^{4} - 10^{2}$	Transitions between vibrational levels (change of configuration)
Microwave	$10^{2} - 1$	Transitions between rotational levels (change of orientation)
Electron spin resonance (ESR)	$1 - 10^{-2}$	Transitions between electron spin levels in magnetic field
Nuclear magnetic resonance (NMR)	$10^{-2} - 10^{-4}$	Transitions between nuclear spin levels in magnetic fields

Table 2.1. Spectral techniques, their frequency (wavenumber) ranges and their origins [90].

Both Raman and infrared (IR) spectroscopy are associated with the vibrational level transitions, although IR spectroscopy also allows for the study of rotational transitions. If the frequency of the laser beam incident on the sample is ϑ_0, we observe frequencies $\vartheta_0 \pm \vartheta_m$ as the Raman-scattered radiation, where ϑ_m is the *molecular vibrational frequency*. This vibrational frequency (ϑ_m) is measured in Raman spectroscopy as a shift from the incident laser frequency (ϑ_0). For general applications, this excitation frequency ϑ_0 is chosen such that its energy is significantly lower than the electronic excited state.

It must be noted that not all materials exhibit the Raman effect. Classical theory offers an explanation as to what materials are *Raman active*. Essentially, all materials that are not Raman active are Raman inactive. The electric field (E) of the laser beam as a function of time (t) is expressed as [90]

$$E = E_0 \cos 2\pi\vartheta_0 t \tag{13}$$

Here, E_0 is the amplitude of the electric field and ϑ_0 is the incident laser frequency. For a diatomic molecule, this electric field induces an electric dipole moment (P), which is proportional to the applied electric field such that

$$P = \alpha E = \alpha E_0 \cos 2\pi\vartheta_0 t \tag{14}$$

where α is the constant of proportionality between P and E, and is called the *polarizability* of the molecule. The molecule vibrates on exposure to this time-dependent electric field. Let the frequency of the molecular vibration be ϑ_m. The vibration also causes a small displacement (q) of the nucleus, which is written as

$$q = q_0 \cos 2\pi\vartheta_m t \tag{15}$$

Here, q_0 is the amplitude of vibration of the nucleus. For a relatively small vibrational amplitude, α is a linear function of q and is expressed as

$$\alpha = \alpha_0 + \left(\frac{d\alpha}{dq}\right)_0 + \ldots \tag{16}$$

where α_0 is the polarizability at equilibrium and $\left(\frac{d\alpha}{dq}\right)_0$ is the rate of change of polarizability with respect to the nuclear displacement at equilibrium. Combining **Equations 14, 15** and **16** and solving for P, we get the following expression:

$$P = \alpha_0 E_0 \cos 2\pi\vartheta_0 t + \frac{1}{2}\left(\frac{d\alpha}{dq}\right)_0 q_0 E_0 [\cos\{2\pi(\vartheta_0 + \vartheta_m)t\} + \cos\{2\pi(\vartheta_0 - \vartheta_m)t\}] \tag{17}$$

The first term in the above expression is an oscillating dipole radiating light of frequency ϑ_0 (elastic scattering). The second and third terms are the inelastic (Raman) scattering of light with frequencies $\vartheta_0 + \vartheta_m$ (*anti-Stokes*) and $\vartheta_0 - \vartheta_m$ (*Stokes*), respectively. For a molecule (or material) to be *Raman active*, the term $\left(\frac{d\alpha}{dq}\right)_0$ must be a non-zero number, thus leading to inelastic scattering of light.

2.2.1 Instrumentation (Raman Spectrometer):

In Raman Spectroscopy, a sample is usually exposed to a laser beam and the Raman spectrum is either obtained at a 90° angle or a 180° angle. A schematic representation of a typical 180° collection angle Raman spectrometer is shown in **Fig. 2.7**.

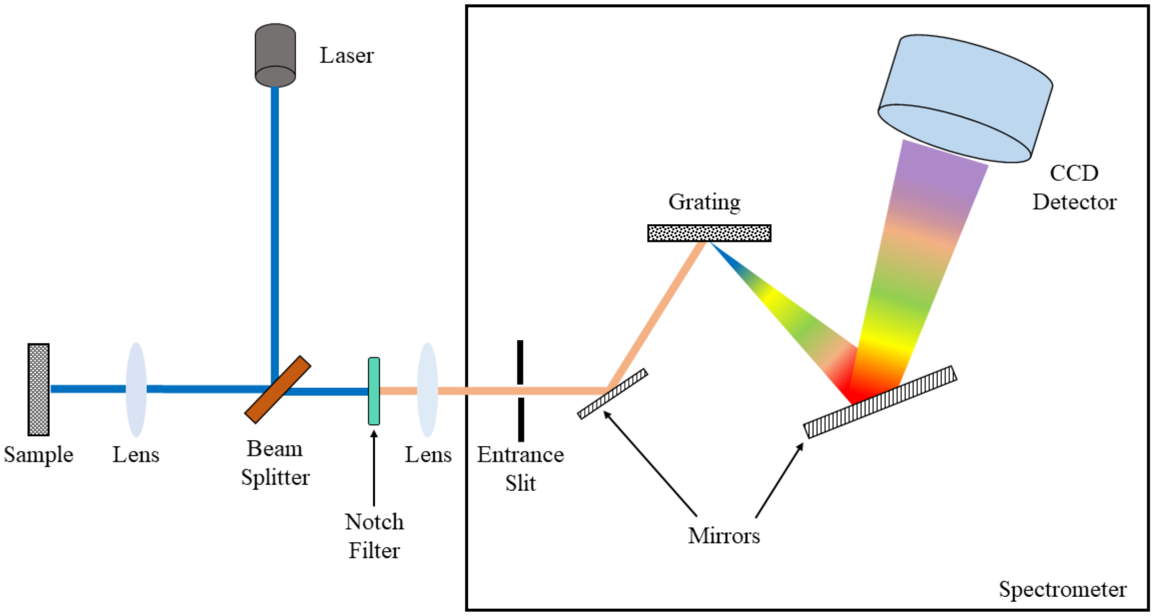

Fig. 2.7. A schematic representation of a Raman spectrometer.

The sample is irradiated with a laser beam usually in the UV/Vis (ultraviolet/visible) wavelength region after the beam is reflected by the beam splitter on to a lens which focuses it on the sample. The configuration depicted in **Fig. 2.7** involves collection of the scattered radiation at an angle of 180° with respect to the incident radiation – this is equivalent to collection of photons reflected from the sample. This reflected beam, which mainly consists of Rayleigh scattered radiation, then passes through the beam splitter and then a *notch filter*. A notch filter blocks a narrow range of frequencies while allowing all others to pass through. For application in a Raman spectrometer, the notch filter is normally chosen so as to block the wavelength of the laser beam used. The filtered radiation containing only the Stokes and anti-Stokes wavelengths is wavelength resolved using a grating and collected by a CCD detector.

A typical Raman spectrum of carbon tetrachloride (CCl_4) is shown below in **Fig. 2.8**. There are some general rules that apply to relative Raman band intensities [91]:

- The intensity of a Raman band is more for a stretching mode as compared to one which is mainly an angular deformation mode.

- In a stretching mode, higher the bond order, higher the intensity. For example, a double bond stretching yields higher intensity than a single bond involving the same constituent atoms (e.g., $C = C$ vs. $C – C$).

- For bond-localized modes, the intensity is directly proportional to the atomic numbers of the atoms involved in the bond.

- If two stretching modes are present, the mode in which the bonds stretch in phase produces a higher Raman intensity as compared to the one in which the bonds stretch out of phase with one another.

- In cyclic molecules (for example, benzene), the 'breathing' modes yield the highest intensities.

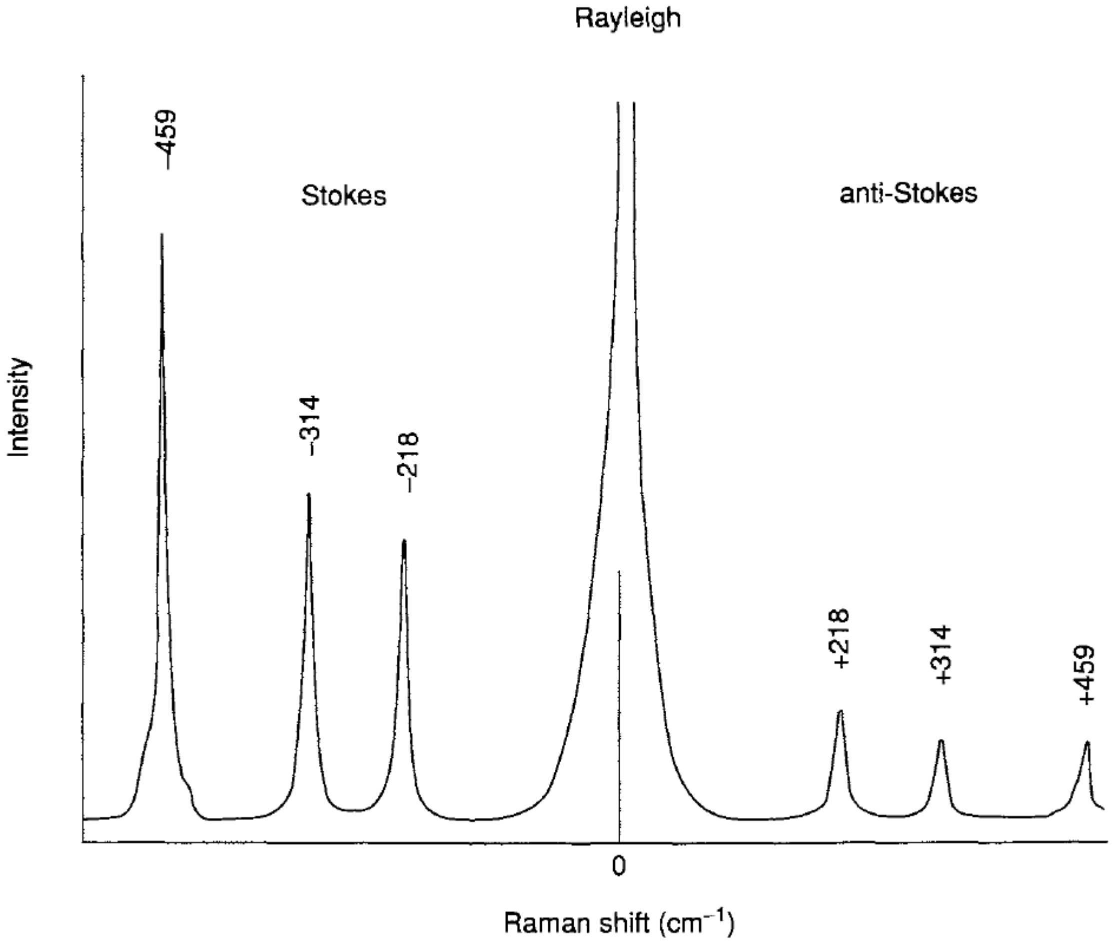

Fig. 2.8. Raman Spectrum of carbon tetrachloride (CCl_4) showing the Stokes and anti-Stokes scattering bands along with the Rayleigh band. As expected, the Stokes (lower energy) bands have higher intensities (energetically more favorable).

Needless to say, the Raman spectrum of a particular molecule is its signature spectrum, meaning that the peak positions in the Raman spectrum of a molecule are specific to that molecule. Therefore, Raman spectroscopy is an excellent analytical tool – if we were given an unknown Raman active substance, a simple Raman spectrum obtained for the material would reveal its identity.

CHAPTER THREE

SHAPE DEPENDENT FLUORESCENCE ENHANCEMENT IN SILVER NANOPARTICLES

Bipin Sharma *et al.*, "Silver Nanodiscs for Enhanced Fluorescence Emission", *Journal of Physical Chemistry C*, 123, 49 (2019): 29811-29817. Reproduced in part with permission from ACS Publications.

3.1 Introduction

Fluorescence is widely used in many biosensing applications such as the quantification of disease markers, protein activity, cytokine and small molecule signals [92]–[101]. Accordingly, concerted efforts have been devoted towards achieving strong enhancements in fluorescence to improve the detection sensitivity of biomarkers [93], [96], [102]. The strong interactions between light and metallic nanostructures have been used to enhance fluorescence emission intensities by, increasing fluorescence absorption, raising quantum yield (QY), increasing the radiative decay rate to allow faster cycling, tuning the far field fluorescence angular distribution, and increasing the number of photons emitted before photobleaching. For instance, silver and gold nanoparticles (Ag and Au NPs) have been widely used for improving the limits of detection through surface plasmon resonance (SPR) and surface plasmon coupled emission (SPCE) [103]–[105]. Metallic NPs alter fluorescence emission by influencing: A) the incident excitation field and B) the radiative and non-radiative decay rates of dye molecules [106]. In the case of single-molecule fluorescence [106], these competing effects (A and B) have been experimentally shown to result in either fluorescence enhancement or quenching depending on the separation distance between dye molecules and NPs. Here, we posit that the NP shape can be tuned to synergistically combine effects A and B to achieve high fluorescence enhancements in an ensemble of dye molecules. Specifically, we show that the fluorescence emission from Rhodamine B (RhB) is enhanced by >30 fold (with respect to RhB on bare glass) in the presence of Ag nanodiscs due to a simultaneous increase in the excitation intensity and photonic mode density. On the other hand, the fluorescence emission from RhB on polyhedral Ag NPs was at least ~2 times weaker compared to RhB on Ag nanodiscs.

As mentioned earlier, plasmonic nanostructure assemblies enable modified light-matter interactions for a macroscopic ensemble of emitters by altering their emission rates or quantum yields. Although free space electromagnetic vacuum fluctuations are only dependent on fundamental physical constants, their photonic mode density or the local density of states is influenced by the surrounding material environment [107]. The total Hamiltonian of a dye under an excitation may be expressed as $H_0 + H_{Exc}$, where H_0 is the unperturbed Hamiltonian of the dye and H_{Exc} is a time-dependent perturbation from the excitation. From here, one can obtain the radiative decay rate (γ) through the Fermi golden rule. However, in the presence of NPs, the photonic mode density is altered and thus an extra term H_{Sec} is necessary in the Hamiltonian. Thus, the total Hamiltonian in the presence of the nanoparticle becomes $H_0 + H_{Exc} + H_{Sec}$. While it is difficult to use a complete quantum electrodynamic treatment to address complex geometries of nanoparticles, other techniques such as local Langevin quantization [107] are often used to describe the effects of H_{Sec}. In this approach, photonic mode density is directly proportional to the imaginary part of the corresponding classical electromagnetic Green's function. Often, the observation of fluorescence enhancement or increased quantum yield is attributed to changes in lifetime or radiative decay rate. However, it should be noted that QY and radiative decay rate are not a cause and effect pair, but both are effects caused by H_{Sec}. Here, by combining the Langevin quantization approach with detailed finite-element simulations, which account for incident, scattered, and dipole radiated electric fields, we show that the enhancement is strongly dependent on the orientation of RhB dipole relative to Ag NPs and nanodiscs. The observed increase in RhB emission on Ag nanodiscs is explained in terms of the nanodisc's scattering spectrum red-shifting towards the RhB emission wavelength, which results in an increased local electric field and higher photonic mode density for Ag nanodiscs. Using atomic force microscopy, hyperspectral imaging, fluorescence spectroscopy, and finite-element simulations, we show that the photonic mode density is dependent on the NP shape.

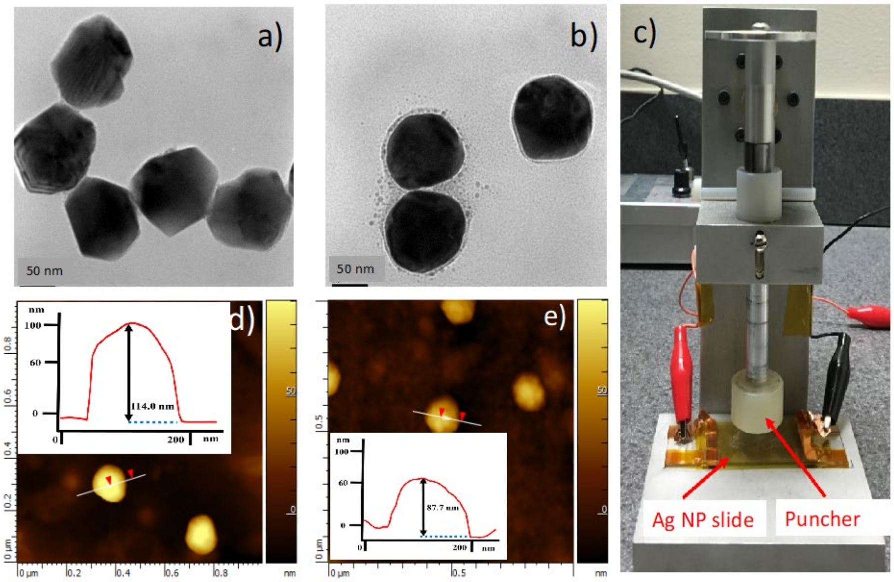

Fig 3.1. (a) and **(b)** show transmission electron microscopy images of (a) *unpunched* and (b) *punched* Ag NPs subjected to 50 N force (scale bar: 50 nm). A home-built puncher with a Teflon mandrel was used for mechanically deforming Ag NPs **(c)**. Zoomed-in AFM images

of **(d)** *unpunched* Ag NPs and **(e)** *punched* Ag NPs (@50N) exhibiting a circular shape with a reduced height for the latter. The insets in panels (d) and (e) show the height profiles, which correspond to 114.0 and 87.7 nm.

3.2 Materials and Methods

3.2.1 Synthesis and characterization of Ag NPs:

To evaluate the effects of nanostructure morphology on RhB emission, polyhedral Ag NPs were first prepared via a previously established method by Chumanov *et al*. [108] Briefly, a saturated aqueous Ag_2O suspension (99.99%, Alfa-Aesar) was reduced by infusing hydrogen (ultrahigh purity) at ~73°C until a faint yellow color was observed indicating the formation of colloidal Ag NPs. The as-prepared Ag NPs were characterized using transmission electron microscopy (TEM, Hitachi 9500) and were found to exhibit a polyhedral single crystal morphology having corners, as shown in **Fig. 3.1 (a)**. Atomic force microscope (AFM) imaging was performed using AIST-NT SPM Smart system. The AFM probes (HQ:NSC14/Al BS-50) were purchased from Micromasch, and AIST-NT image analysis and processing (Version 3.3.105ex1) software was used for AFM topographic image analysis. The Ag NPs were then coated onto microscope slides.

3.2.2 Preparation of PVP- and Ag NP- coated glass slides:

Bare glass-microscope-slides (*25 mm × 15 mm × 1 mm*) were functionalized with a polyvinyl pyrrolidone (PVP) layer (~10 nm) by submerging them in a 0.01 wt. % PVPethanol solution for 4 hours. Following rinsing and drying, PVP functionalized slides were immersed into the synthesized Ag NP suspension under constant agitation for ~10 hours. This step facilitated the chemisorption of Ag NPs that form bonds with the lone-pair electrons on the pyridyl ring of PVP coated on the slides.

3.2.3 Preparation and characterization of Ag nanodiscs:

Ag nanodiscs were prepared using a home-built puncher (discussed in **Fig. 3.1 (c)**). For the puncher, a 12 V DC stepper motor (Zheng motors, ZYTD520 3500 r/min) was used to deliver mechanical force through the puncher (**Fig 3.2**). The as-prepared Ag NPs were subjected to different punching forces (16, 33, and 50 N) using the Teflon puncher to obtain Ag nanodiscs. The effect of nanoparticle morphology on fluorescence emission was studied by uniformly spin coating (3000 rpm for 60 s to form a ~30 nm overcoat) RhB fluorophore (1 µM- 1 mM) on glass slides containing both punched and unpunched Ag NPs. The fluorescence spectra of RhB molecules were collected using a Renishaw inVia micro-Raman spectrometer with a 532 nm laser excitation from multiple spots (n > 5) and averaged to account for possible heterogeneity in coating. A dark-field transmission optical microscope equipped with the CytoViva hyperspectral imaging system (Cytoviva HSI, Auburn, AL) was employed to obtain high-resolution scattering spectra from Ag NPs and 50 N punched Ag nanodiscs.

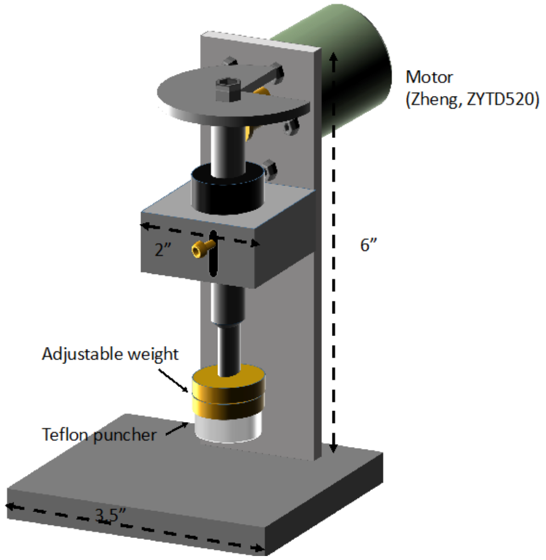

Fig 3.2. A schematic of the home-built Teflon puncher used in this study.

3.3 Results and Discussion

3.3.1 Experimental observations:

Previously, Qian *et al.* [109] used classical Mie theory with size and strain-corrected dielectric functions to show that mechanical strain leads to substantial enhancements in the absorption and scattering maxima of Au NPs in addition to a significant shift in their plasmon resonance wavelength. Similarly, Ameer *et al*. [110] showed that surface plasmon resonance can be red-shifted by mechanical deformation. Building on these works, we used a new scalable method to create arrays of Ag nanodiscs by applying transverse force on polyhedral Ag NPs using a home-built Teflon puncher (see **Fig. 3.1 (c)**). To alter the NP shape, the glass-slides coated with Ag NPs were deformed through the application of a transverse mechanical force using a motorized Teflon coated circular puncher (automated to deliver force at 2 Hz) with a radius of ~1 cm. As the force was applied only over a part of the slide (corresponding to the puncher area ~3.14 cm^2), we were able to prepare both as-prepared Ag NPs (in the *unpunched* regions) and Ag nanodiscs (*punched* regions) on the same glass slide. The as-prepared Ag NPs were found to be mechanically deformed to nanodiscs upon subjecting them to a force of 50 N (**Fig. 3.1 (b)**). While *unpunched* Ag NPs displayed sharp edges (**Fig. 3.1 (a)**), *punched* Ag NPs subjected to 50 N force exhibited a smooth circular boundary (**Fig. 3.1 (b)**) in TEM studies. The lateral size of *unpunched* (105±10 nm) and 50 N *punched* NPs (113±10 nm) gleaned from TEM images was consistent with the deformed particles exhibiting slightly larger diameters. Considering that TEM is more reliable for measuring the lateral size, we conducted AFM to understand the effects of applied force on the NP height. The *unpunched* Ag NPs showed an average height of ~114 nm (**Fig. 3.1 (d)**) that is very similar to their lateral size (~105 nm) suggesting that they are nearly spherical with an aspect ratio (diameter/height) of ~0.95. On the other hand, the 50 N punched Ag NPs exhibited a smooth circular boundary with a height ~88 nm (**Fig. 3.1 (e)**) that is significantly lower than their lateral size (113±9 nm). This is indicative of a flattened sphere or 'disc' shaped morphology with an increased aspect ratio of ~1.34. A schematic of the home-built Teflon puncher used in this study is shown in **Fig. 3.2**. We studied the influence of applied force on particle morphology, as shown in **Fig. 3.3**. We prepared punched Ag NPs of different heights (106±10, 99±12, and 88±10 nm) and different lateral sizes (106±10, 108±10, and 113±10 nm) by subjecting as-prepared Ag NPs to different forces (16, 33, and 50 N). The heights and lateral sizes for all punched Ag NPs are listed in **Table 3.1**. It should also be noted that we did not observe any significant changes in the interplanar spacing of crystal planes in unpunched and punched Ag NPs even at 50N, as shown in **Fig. 3.4**.

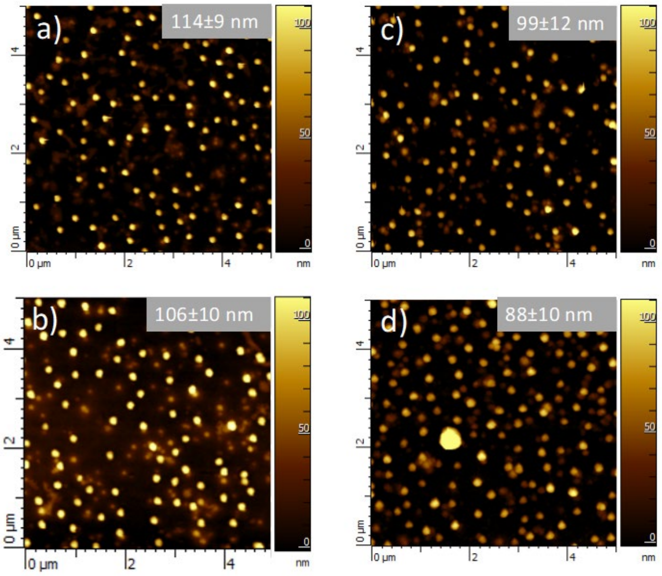

Fig. 3.3. AFM topographic images for **(a)** as-prepared Ag NPs and **(b-d)** Ag NPs subjected to a 16, 33, and 50 N force, respectively. The numbers in the inset indicate the average height. While Ag NPs subjected to 16 N force (106±10 nm) did not exhibit a significant change in their height compared to as-prepared Ag NPs (114±9 nm), Ag NPs subjected to 33 and 50 N displayed a height (99±12 nm and 88±10 nm) that is significantly lower than their lateral size (113±10 nm). The heights and lateral sizes for all punched Ag NPs are listed in **Table 3.1**.

Sample	Height	Lateral size
Unpunched Ag NPs	114±9 nm	105±10 nm
16 N punched Ag NPs	106±10 nm	106±10 nm
33 N punched Ag NPs	99±12 nm	108±10 nm
50 N punched Ag NPs	88±10 nm	113±10 nm

Table 3.1. Heights and lateral sizes for Ag NPs subjected to different forces

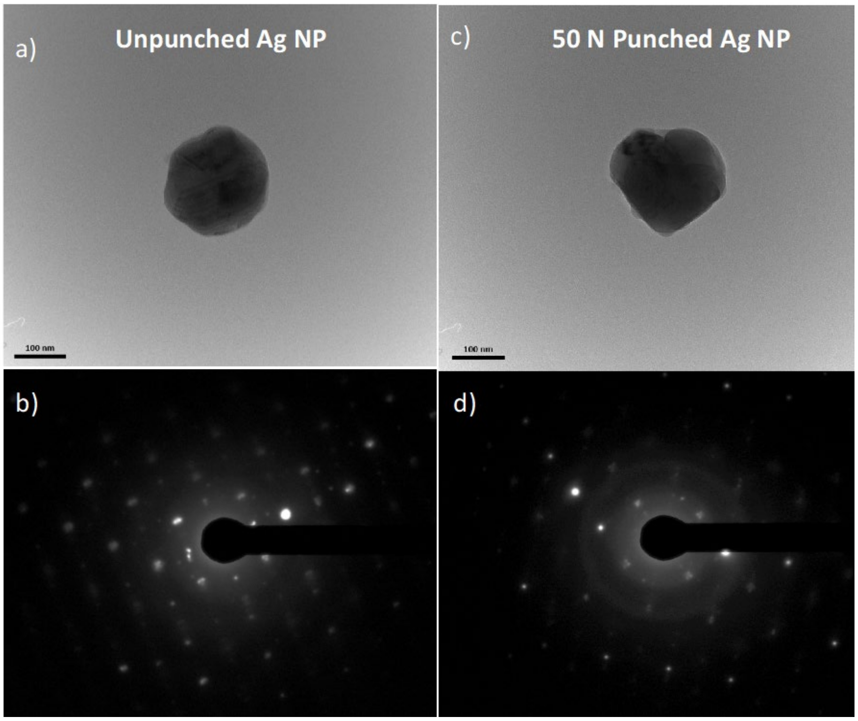

Fig. 3.4. (a, c) High-resolution TEM images of unpunched and 50 N punched Ag NPs and **(b, d)** their corresponding selected area electron diffraction pattern obtained at 300 kV with a camera length of 0.25 m. No significant difference was observed in the interplanar spacing (0.14 nm for unpunched vs. 0.15 nm for punched, which is within error limits).

3.3.2 Theoretical explanation of experimental results:

It is well known that any change in the size or shape of metallic NPs drastically alters their optical and plasmonic properties [108]. **Fig 3.5 (a)** shows a dark-field image of the substrate containing both *unpunched* (i.e., as-prepared) and 50 N *punched* Ag NPs. While the blue-region represents the *unpunched* portion of Ag NPs, the reddish tinge arises due to the presence of *punched* Ag nanodiscs. The scattering spectrum (**Fig. 3.5 (b)**) of deformed Ag nanodiscs (peak at ~600 nm with a width ~180 nm) red-shifted with respect to that of as-synthesized polyhedral Ag NPs (peak at ~530 nm with a width ~150 nm), which is attributed to the increased aspect ratio from 0.95 (*unpunched*) to 1.34 (50 N *punched* Ag nanodiscs).

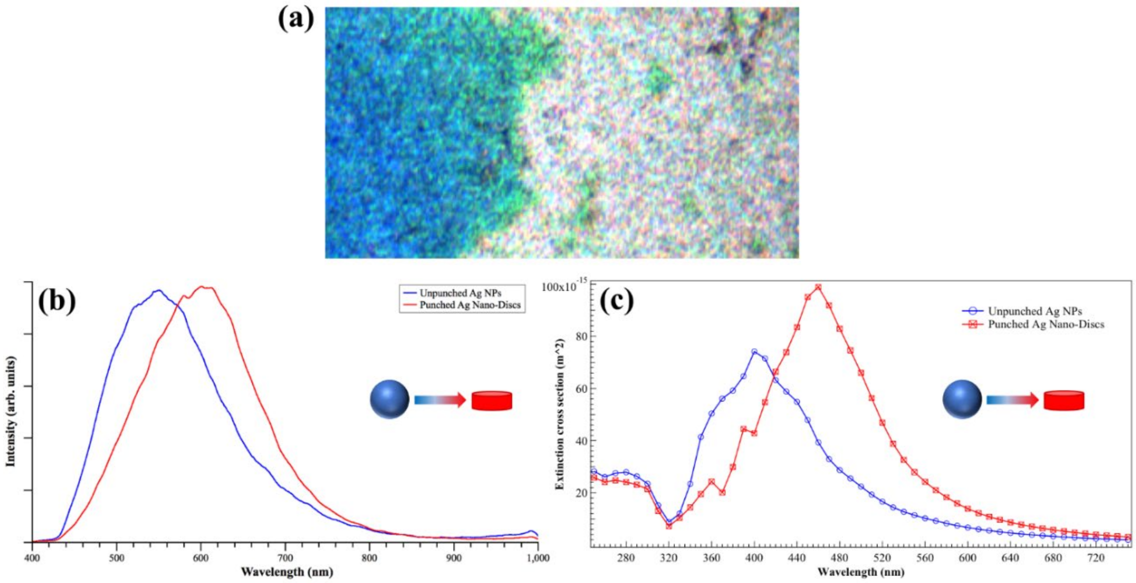

Fig. 3.5. (a) A dark field image showing *unpunched* (blue) and *punched* (red) regions of the glass substrate; **(b)** corresponding red-shifted scattering spectra acquired from Cytoviva optical microscope; and **(c)** COMSOL simulations showing a red-shift in the extinction spectra from *unpunched* Ag NPs to *punched* Ag nanodiscs.

To better understand the effects of mechanical deformation, we simulated the extinction spectrum of Ag NPs and nanodiscs (with the observed experimental sizes) by numerically solving the Helmholtz wave equation for the total electric field in the full field formulation with a plane wave incidence using COMSOL Multiphysics finite element method (**Fig. 3.5 (c)**). Permittivity values for silver were adopted from Johnson and Christy's work [111]. The simulations confirmed that the higher aspect ratio of Ag nanodiscs changes the frequency dependence of the scattered E-field leading to an upshifted peak in their extinction spectrum.

The effect of nanoparticle morphology on fluorescence emission was studied by uniformly spin coating (3000 rpm for 60 s to form a ~30 nm overcoat) RhB fluorophore (1 µM- 1 mM) on glass slides containing both *unpunched* and *punched* Ag NPs (obtained using 16, 33, and 50 N punching force). **Fig. 3.6** shows the fluorescence intensity of RhB (1 mM) on *unpunched* Ag NPs, 50 N *punched* Ag nanodiscs, and a plain glass-slide. The emission from RhB coated on a plain glass-slide served as the control. Clearly, RhB emission on both 50 N *punched* Ag nanodiscs and *unpunched* Ag NPs produced high signal enhancements over the control. While *unpunched* Ag NPs exhibited ~15-fold enhancement, 50 N *punched* Ag nanodiscs showed even higher enhancements ~33-fold with respect to the control and ~2.2-fold with respect to *unpunched* Ag NPs.

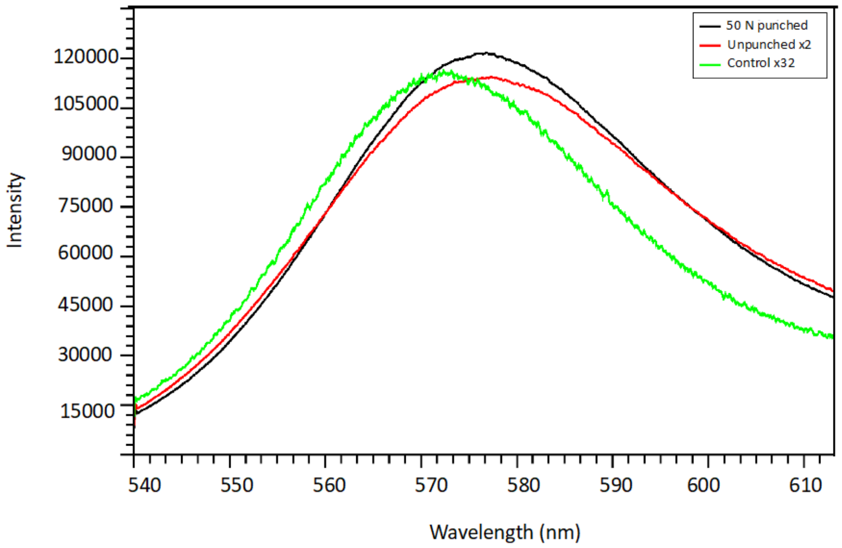

Fig. 3.6. Fluorescence spectrum of Rhodamine B (1 mM) on a plain glass slide, *unpunched* Ag NPs, and 50 N *punched* Ag nanodiscs. The RhB fluorescence spectrum on *unpunched* Ag NPs and *punched* Ag nanodiscs was found to exhibit 15-fold and 33-fold enhancement relative to the control spectrum on a plain glass slide.

Similar enhancements were observed at different RhB concentrations ranging from 1 µM-1 mM for 50 N *punched* Ag nanodiscs (**Fig. 3.7 (a)**). We performed similar studies on 16 and 33 N *punched* Ag nanodiscs. Not surprisingly, as shown in **Fig. 3.7 (b)**, the enhancement for 16 and 33 N *punched* Ag nanodiscs with respect to *unpunched* Ag NPs was lower compared to 50 N *punched* Ag nanodiscs because they were not completely deformed. Indeed, there was no discernible difference between RhB intensity on *unpunched* Ag NPs and 16 N *punched* Ag NPs (**Fig. 3.7(b)**; enhancement factor for 16 N force is 1.0). Such a result is attributed to the lack of any significant change in the aspect ratio of Ag NPs upon punching at 16 N (*cf*. **Fig. 3.3** and **Table 3.1**). On the other hand, the higher enhancements observed for 33 and 50 N Ag nanodiscs may be rationalized through the following analysis.

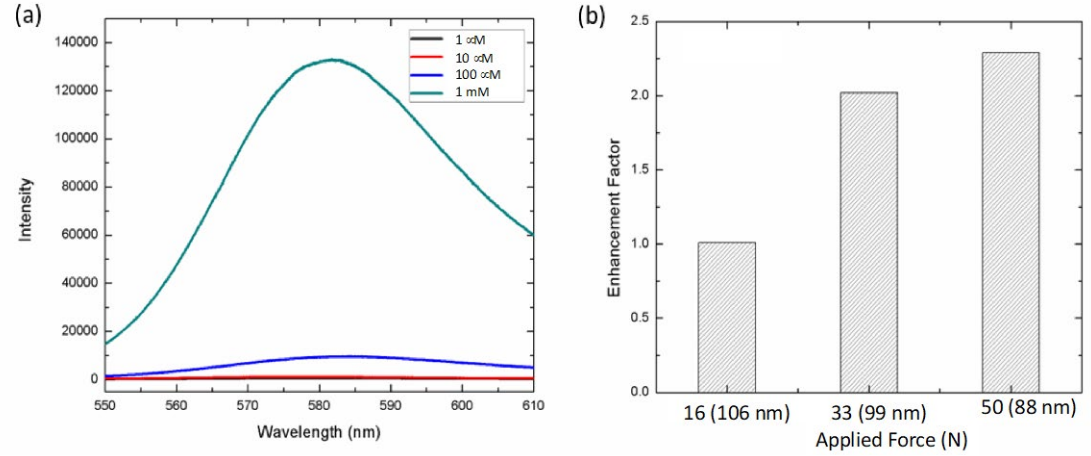

Fig. 3.7. (a) Fluorescence spectrum of RhB on 50 N punched Ag nanodiscs at different concentrations; **(b)** Enhancement factor (defined as the enhancement in the intensity of RhB fluorescence with respect to *unpunched* Ag NP at 1 mM) for different *punched* Ag nanodiscs. While Ag NPs subjected to 16 N force did not show any change compared to unpunched Ag NPs, 33 and 50 N *punched* Ag NPs showed ~2.0 and 2.2-fold enhancement relative to *unpunched* Ag NPs. The x-axis label shows the heights in parentheses for each force.

In a simplified NP-dye model, the presence of NPs in the vicinity of dyes is known to change the frequency (ω) dependent radiation field $\vec{E}_{inc}(\omega)$ due to the addition of scattered field ($\vec{E}_{sca}(\omega)$) leading to a new excitation field given by $\vec{E}_{exc}(\omega) = \vec{E}_{inc}(\omega) + \vec{E}_{sca}(\omega)$. While this simplification is apt for some cases such as the single-molecule case, the true excitation field must include an additional secondary field ($\vec{E}_{sec}(\omega)$) arising from the spontaneous emission of the dye. Each dye molecule acts as an emitting dipole whose field interacts with the NP to in turn backscatter $\vec{E}_{sec}(\omega)$ as a part of the excitation field. Beyond the single-molecule fluorescence case [106], the backscattered $\vec{E}_{sec}(\omega)$ may play more significant role in an ensemble of dyes due to a higher number of dye molecules associated with each NP. Thus, the true total excitation field ($\vec{E}_{total}$) for dye ensemble is given by $\vec{E}_{total}(\omega) = \vec{E}_{exc}(\omega) + \vec{E}_{sec}(\omega)$. Based on Maxwell's equations, the secondary field may be expressed as $\vec{E}_{sec}(\omega) = \overleftrightarrow{G}(r, r', \omega).\vec{p}(\omega)$, where $\overleftrightarrow{G}(r, r', \omega)$ is the dyadic Green's function connecting the *E*-field at a position *r* due to a dipole at *r*' while $\vec{p}(\omega)$ is the dipole moment of RhB [102], [106], [112], [113]. Thus, a self-consistent expression for the frequency-dependent dipole moment may be obtained from

$$\vec{p}(\omega) = \alpha(\omega)\vec{E}_{total}(\omega) = \alpha(\omega)\left(\vec{E}_{exc} + \vec{E}_{sec}\right) = \alpha(\omega)\vec{E}_{exc} + \alpha(\omega)\overleftrightarrow{G}(r, r', \omega).\vec{p}(\omega) \quad (12)$$

where $\alpha(\omega)$ is the polarizability of the dye. Considering the dipole moment to be aligned along a direction $\hat{e}_d$ yields the magnitude of $\vec{p}(\omega)$ given by $\vec{p}(\omega) = \frac{\alpha(\omega)(\hat{e}_d \bullet \vec{E}_{exc})}{1-\alpha(\omega)(\hat{e}_d \bullet \overleftrightarrow{G}(r,r',\omega) \bullet \hat{e}_d)}$.

If the backscattered field from the radiating dipoles is ignored, then the second term in the denominator becomes zero resulting in the standard form of the dipole moment. As mentioned earlier, the presence of NPs influences the excitation (effect A) due to changes in the local field. The NP-induced excitation enhancement is proportional to the ratio of square of the local electric field with and without NPs. Given that $\vec{p}(\omega) = \alpha(\omega)\vec{E}_{total}(\omega)$, the excitation enhancement factor (*EEF*) is equivalent to the ratio of square of the dipole moment strengths in the presence/absence of the NP.

$$EEF = \left(\frac{\hat{e}_d \bullet \vec{E}_{exc}}{\hat{e}_d \bullet \vec{E}_{inc}}\right)^2 \frac{1}{\left(1 - \alpha(\omega)\left(\hat{e}_d \bullet \overleftrightarrow{G}(r, r', \omega) \bullet \hat{e}_d\right)\right)^2} \tag{13}$$

While the traditional excitation enhancement occurs solely due to the scattered field, the above expression for *EEF* combines the effects of secondary field dependent on an extra "field term" $\left(\hat{e}_d \bullet \overleftrightarrow{G}(r, r', \omega) \bullet \hat{e}_d\right)$ related to the dipole field. Similar to the enhancement of excitement intensity, the presence of NPs also alters the radiative decay rate (effect B). The radiative decay rate (γ) of a dye molecule, from an excited state $|k\rangle$ of energy E_k to a lower state $|n\rangle$ of energy E_n, through the emission of a photon of energy $\hbar\omega$ may be understood in terms of the Fermi golden rule given by

$$\gamma = \frac{2\pi}{\hbar} \sum_{n \neq k} \left|\langle n|\vec{p} \bullet \vec{E}_{tot}|k\rangle\right|^2 \delta(E_k - E_n - \hbar\omega) \tag{14}$$

The Fermi golden rule can also be expressed in terms of photonic mode density or $\rho(r, \omega)$ within the vicinity of the dye, which is defined by the ratio of photon flow per unit area per second (i.e., power flow per photon) to the velocity of photons

$$\gamma = \frac{2\omega}{3\hbar\varepsilon_0}\langle p\rangle^2 \rho(r,\omega) \tag{15}$$

where $\rho(r,\omega) = \frac{6\omega}{\pi c^2}\left(\hat{e}_d \bullet \overleftrightarrow{G}(r,r',\omega) \bullet \hat{e}_d\right)$. The photonic mode density, and thus the decay rate of a dye, is determined by the field term $\left(\hat{e}_d \bullet \overleftrightarrow{G}(r,r',\omega) \bullet \hat{e}_d\right)$ containing the dyadic Green's function of the system in which the dye is embedded. The field term $\left(\hat{e}_d \bullet \overleftrightarrow{G}(r,r',\omega) \bullet \hat{e}_d\right)$ is frequency dependent and is sensitive to the changes in the scattering spectrum of the surrounding NPs.

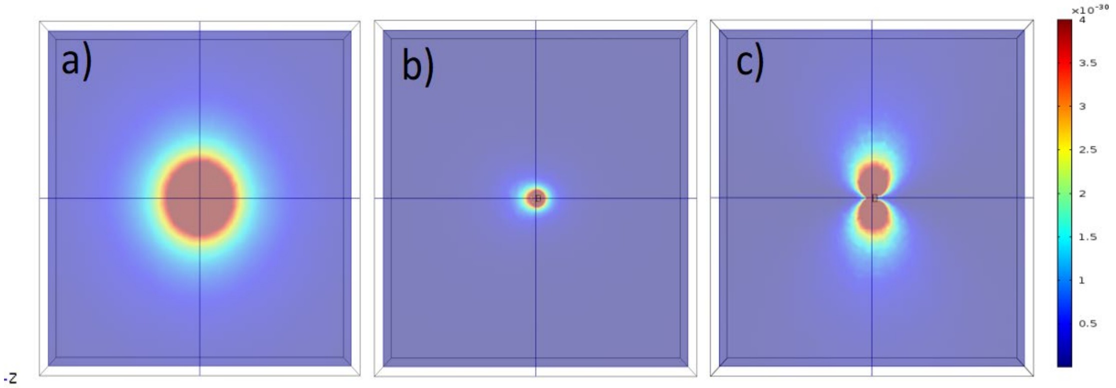

Fig. 3.8. COMSOL simulation showing time-averaged Poynting vector for a point dipole located at the center of a disc in the *y-z* plane **(a)**; a dipole positioned at a distance of 10 nm perpendicular **(b)** or parallel **(c)** to the nanodisc. Each of these configurations influenced the symmetry of the radiated field.

Given that the punched Ag NPs or nanodiscs show a red-shift in their scattering, which is closer to the emission wavelength of RhB, it may be rationalized that the field term at the emission frequency of RhB is higher for Ag nanodiscs compared to polyhedral Ag NPs due to increased local field from scattering. This increase in the field term is expected to simultaneously enhance both the excitation intensity (**Equation 13**) and the decay rate (**Equation 15**) leading to a higher enhancement.

We validated the observed enhancements by simulating the emission of an electric dipole (mimicking RhB molecule with dipole moment 9.78 D) 10 nm above spherical and punched Ag NP surface using the RF module in COMSOL Multiphysics v5.1. This full field model, which includes the effects of scattered and secondary fields, was used to compute both normalized electric field (*normE*) and time-average Poynting vector (P_{av}) (see **Fig. 3.8 (a-c)**). Our simulations evidenced that the electric field of the radiating dipole changed from a spherically symmetric shape to a dumbbell shape in the presence of both Ag NPs and nanodiscs. Furthermore, the simulations showed that the total enhancement factor is dependent on the orientation of the dipole. The dipole showed a higher enhancement when it is oriented parallel to the NPs. In our experiments, the orientation of RhB in the dye ensemble relative to Ag NPs or nanodiscs is random. Thus, we obtained the overall enhancement factor from simulations by weighing 2/3 parallel versus 1/3 perpendicular direction. The P_{av} for Ag nanodiscs showed a higher enhancement factor ~10 times over free space and ~4 times relative to Ag NPs concurring with our experimental results.

3.4 Conclusions

In summary, we experimentally showed that the RhB emission can be increased up to ~33 folds by flattening AgNPs. We produced Ag nanodiscs through mechanical deformation of polyhedral Ag NPs coated on a glass slide. The higher enhancement factors in the presence of Ag nanodiscs (~33 fold) compared to Ag NPs (~15 folds) are rationalized in terms of the higher contribution from secondary *E*-field comprised of dipole radiation of RhB. Ag nanodiscs exhibited a red-shift in their scattering spectrum due to a higher aspect ratio with a peak (~600 nm) closer to the RhB emission peak (~580 nm). Such a red-shift resulted in a better enhancement of both the excitation intensity and the radiative decay rate of RhB in the presence of Ag nanodiscs relative to Ag NPs. The experimentally observed upshift in scattering and the higher enhancement factors for Ag nanodiscs were validated by a COMSOL finite element model, which considered the effects of both incident and scattered electric fields.

CHAPTER FOUR

ULTRASENSITIVE PLATFORM FOR FEMTOMOLAR DETECTION OF BIOMARKERS

Bipin Sharma *et al.*, “Analyte-induced disruption of luminescence quenching (AIDLuQ) for femtomolar detection of biomarkers”, *Nanoscale*, 11 (2019): 14010-14015. Reproduced with permission from RSC.

4.1 Introduction

Graphene, a sheet of sp^2 hybridized carbon atoms, has received much attention due to its unique physicochemical properties. It is ideally suited for the realization of biosensors in various transduction modes ranging from electrical/electrochemical transduction to optical detection [114]–[117]. Specifically, graphene presents an excellent platform for fluorescence energy transfer or quenching [118], [119] due to its linear electronic energy bands with high optical absorption (~2.3% per layer [120]–[124]). Others and we have previously shown that emission from traditional dyes and quantum dots [118] can be quenched by resonant energy transfer via the excitation of electron-hole pairs in graphene. This ability of graphene has also been utilized in suppressing background fluorescence and enhancing Raman signals in graphene-enhanced Raman spectroscopy or GERS [125]. Building on fluorescence quenching properties of graphene, this article presents a novel flexible immunosensor for highly sensitive and rapid detection of proteins and biomarkers.

Traditionally, antibody-based immunoassays have been extensively used for the detection of proteins due to their high sensitivity and specificity. Despite these advantages, conventional immunoassays (e.g., lateral flow, microarray, enzyme-linked immunosorbent assay) [126] require long incubation times, multiple washing steps, and are unsuitable for point-of-care (POC) testing [127]. Over the past two decades, there has been a steady increase in the availability and use of flexible and inexpensive POC sensors for disease diagnosis and monitoring [128]–[130]. Previously, we used surface plasmon (SP) coupled emission [131] to develop highly sensitive fluorescent POC platforms for pathogen detection. Although such SP platforms improve the sensitivity and flexibility needed for POC testing, they do not alleviate long incubation and multiple washing steps. In this regard, there is a great need for rapid, highly sensitive (up to femto-molar concentrations), flexible, and inexpensive optical POC sensors for detection of specific biomarkers. Here, we used the fluorescence quenching properties of graphene to build a rapid, flexible, cost-effective, extremely sensitive and highly efficient immunosensing platform.

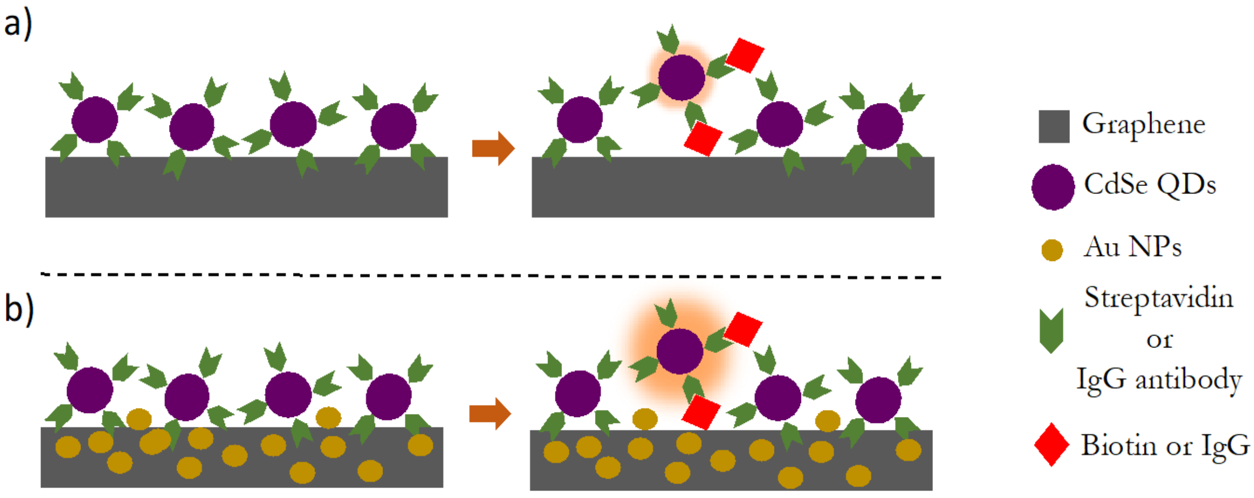

Fig. 4.1. (a) The sensing platform consists of receptor (e.g. streptavidin or IgG antibody) functionalized CdSe quantum dots (QDs) deposited on a flexible graphene paper. The fluorescence emission from CdSe QDs is quenched when they are spatially close to graphene.

Upon the addition of analyte (e.g. biotin or IgG), some CdSe QDs are lifted off from the graphene surface due to binding with receptors on the surface of CdSe QDs. The binding increases the spatial gap between CdSe QDs and graphene, which disrupts quenching and results in an increased emission from QDs. The number of CdSe QDs lifted off from graphene surface is proportional to the analyte concentration. Thus, the increase in the emission of CdSe QDs could be used as a tool to detect different analytes; **(b)** A platform similar to the one presented in (a) with the extra addition of gold nanoparticle (Au NPs) is shown. In this case, the binding of analyte disrupts quenching caused by graphene while plasmonic Au NPs enhance the emission of CdSe QDs to enable highly sensitive detection of low analyte concentrations.

In many conventional immunoassays, at least two antibodies are necessary for detecting an analyte. While the primary antibody captures the analyte, a labelled secondary antibody (often labelled with a dye or an optically active molecule) is used to obtain a measurable optical signal to quantify the analyte [132]. Some immunoassays (such as the capture sandwich assay) necessitate the use of three antibodies. Unlike these methods where the detection antibody is added at the end, our graphene sensing platform is pre-coated with detection antibodies (see **Fig. 4.1**) labelled highly luminescent quantum dots (QDs). However, the luminescence of QDs on the platform is almost completely quenched due to the presence of graphene. Upon the addition of analyte, the analyte binds with the detection antibody and raises QDs away from graphene leading to reappearance of QD emission (**Fig. 4.1 (a)**). Thus, in a single step, the analyte can be detected. While this simple platform allows for rapid detection of analytes, its sensitivity is limited by the emission intensity and quantum yield of QDs. To improve the sensitivity, we incorporated gold nanoparticles (Au NPs) into graphene platform (**Fig. 4.1 (b)**). In the graphene-Au platform, the analyte raises QDs away from the surface similar to graphene platform leading to recovery in QD emission. The analyte-antibody pair acts as a spacer between Au NPs embedded in graphene and QDs, which leads to surface plasmon-induced increase in emission and consequently higher sensitivity.

In other words, as described in **Fig. 4.1**, this process relies on analyte induced disruption of luminesce quenching (AIDLuQ). The AIDLuQ platform has multiple advantages such as: i) easy scalability in manufacturing, ii) flexibility, iii) inexpensive, iv) alleviation of the use of a second antibody as is the case in most of traditional antigen-antibody immunosensing techniques, and v) shorter incubation time (15-30 min). We demonstrated two model assays using biotin-streptavidin and human immunoglobulin assay to illustrate the practical applications of AIDLuQ sensors. Our results show clear evidence that AIDLuQ sensors are successfully able to achieve selective and specific detection up to 10 fM on graphene-Au platform. The limit of detection observed in our graphene-Au platform is at superior to other similar IgG sensing platforms (**Table 4.1**).

Reference	**Sensitivity (fM)**
This work	10
Human IgG ELISA Kit (Abcam)	1500
NPG Asia Materials vol. 6, 112 (2014)	20
Biosensors and Bioelectronics, 31(1), 233-239	1100
Nano Research 4, no. 10 (2011)	1000 - 10000

Biosensors and Bioelectronics, 26(7), 3297-3302.	20000
Talanta, 83(1), 42-47.	20000
International Journal of Biological Macromolecules, 43(2), 165-169.	10^5 - 10^7
Sensors and Actuators B: Chemical, 74(1-3), 106-111.	$2x10^5$ - $2.7x10^6$
Journal of Biophotonics, 9(3), 218-223.	$5x10^6$ – $2x10^8$
Microchimica Acta 183, no. 7 (2016): 2177-2184.	$5x10^5$
Sensors, 17(4), 898.	10^5 - 10^6

Table 4.1. A comparison of the reported sensitivities of platforms/kits for the detection of Immunoglobulin G (IgG).

4.2 Materials and Methods

4.2.1 Synthesis of graphene/graphene-AuNP paper:

Exfoliated graphene nanoplatelets (Grade M) were obtained from XG Science (Mason, MI). Detailed atomic force microscopy images of graphene platelets are provided in **Fig. 4.2**. A 5 mg/ml suspension of exfoliated graphene nanoplatelets was prepared in 75 ml acetone via tip sonication for 30 minutes (Branson 250W, 1/8” tip sonicator). This solution was then spray-coated thrice using an industrial spray gun (Iwata 5095 WS400; 1.3 mm nozzle, 29 psi ambient air pressure) to coat a layer of graphene on a standard copier paper (21 x 29.7 cm). A representative scanning electron micrograph (obtained using Hitachi S-4800) of graphene coated paper is shown in **Fig. 4.3 (a)**. For preparing graphene-Au NP platform, 7.5 ml of 1.5 mg/ml ~10 nm Au NPs (Vive Nano, Inc.) was added to the 5 mg/ml graphene suspension before the third coat. This corresponds to a net areal Au NP density of ~18 μg/cm^2, which was found to be optimal for sensing. The paper was dried for 15 min in air after each coating. The dried graphene/graphene-Au NP papers were stored in dark and dry conditions.

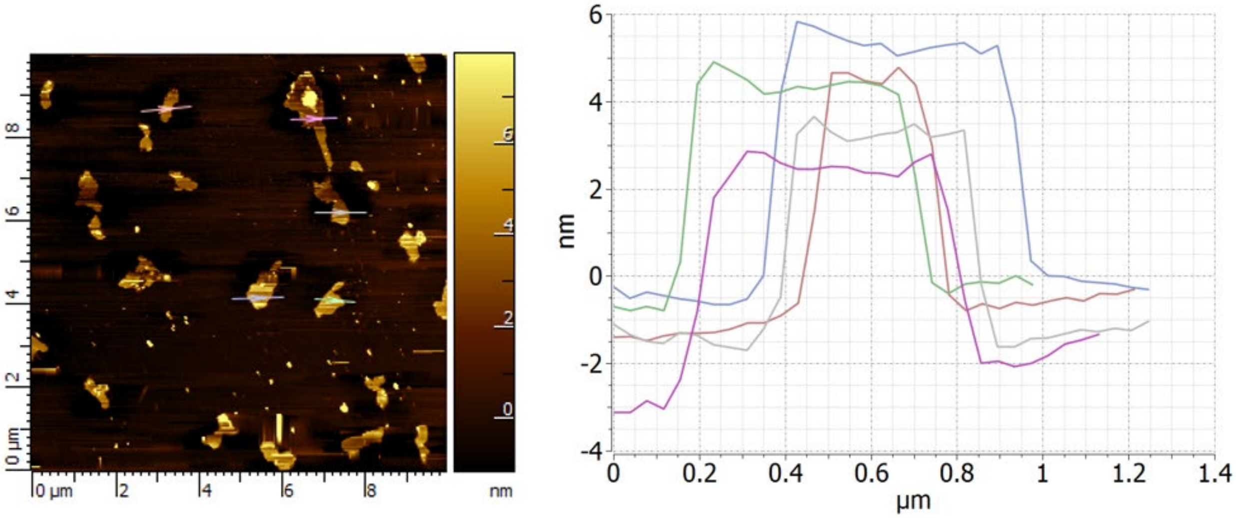

Fig. 4.2. Atomic Force Microscopy (AFM) images (left panel) and corresponding line scans (right panel) of graphene show that the flakes have an average thickness of ~ 5±1.5 nm.

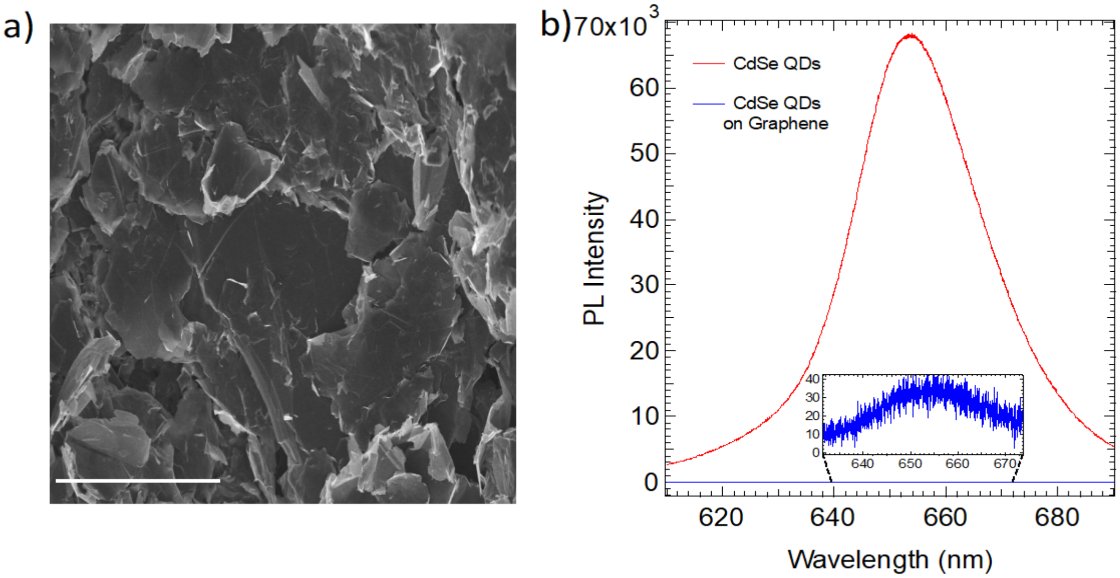

Fig. 4.3. (a) A representative scanning electron micrograph of graphene coated paper. The graphene flakes are ~ 5 nm thick with lateral dimensions in the range of a few microns (the scale bar is 20 µm). **(b)** The emission of CdSe QDs on graphene is strongly quenched due to the interactions between the pi-electron clouds of graphene and d-orbitals of CdSe QDs. The inset shows a very weak quenched emission peak for the CdSe QDs on graphene.

4.2.2 Preparation of standard buffer:

A standard buffer was prepared by mixing 0.5% (v/v) Tween-20 and 1% (w/v) of BSA in 0.01 M phosphate buffer saline (PBS). This standard buffer was used as a solvent for all the further studies.

4.2.3 Conjugation of CdSe QDs with antibodies:

CdSe QDs were purchased from Thermo Fisher Scientific (Invitrogen, *Cat. # Q10123MP*). QDs were mixed with anti-human IgG antibody (Ab) (Abcam, *Cat. # ab109489*) in the standard buffer to attain a final concentration of 100 nM for QDs and 200 μg ml^{-1} for Ab. These optimal concentrations for QDs and Ab was chosen based on previous studies [133]. The conjugation was carried out by continuous shaking at 650 rpm and 4°C for 30 min.

4.2.4 Preparation of graphene/graphene-AuNP sensing platforms:

For sensing experiments, graphene or graphene-Au NP coated paper was cut ~1 x 1cm pieces. 2 μl of the QD-Ab conjugate was drop cast on to each piece and left to dry at room temperature for 1 hour. Detailed electron microscopy images of graphene/graphene-Au NP sensing platform and the nanoparticles are provided below in **Fig. 4.4** and **Fig. 4.5**. Upon drying, the fluorescence intensity of QDs was measured for at least three spots on each piece with the excitation of 532 nm using Renishaw InVia micro-spectrometer. The average (n=3) spectrum was considered as the background fluorescence.

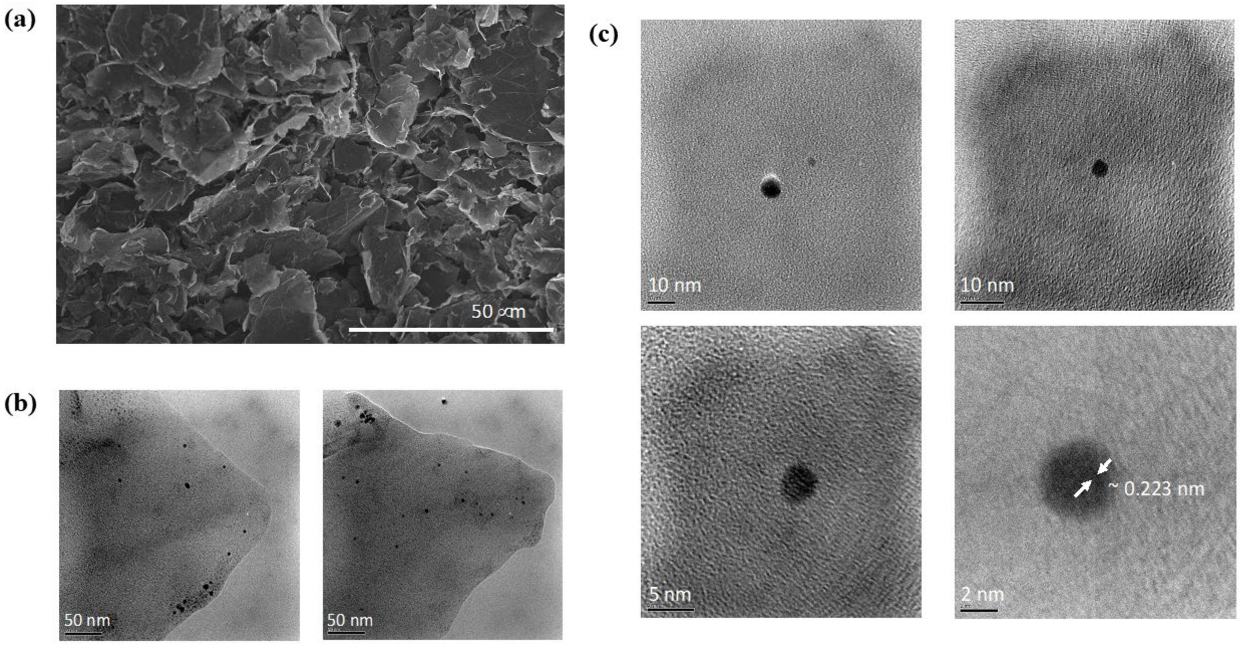

Fig. 4.4. (a) A representative of the scanning electron micrograph of graphene-AuNP paper; **(b)** Transmission electron microscopy (TEM) images of the graphene-AuNP flakes; **(c)** High-resolution images of the AuNPs.

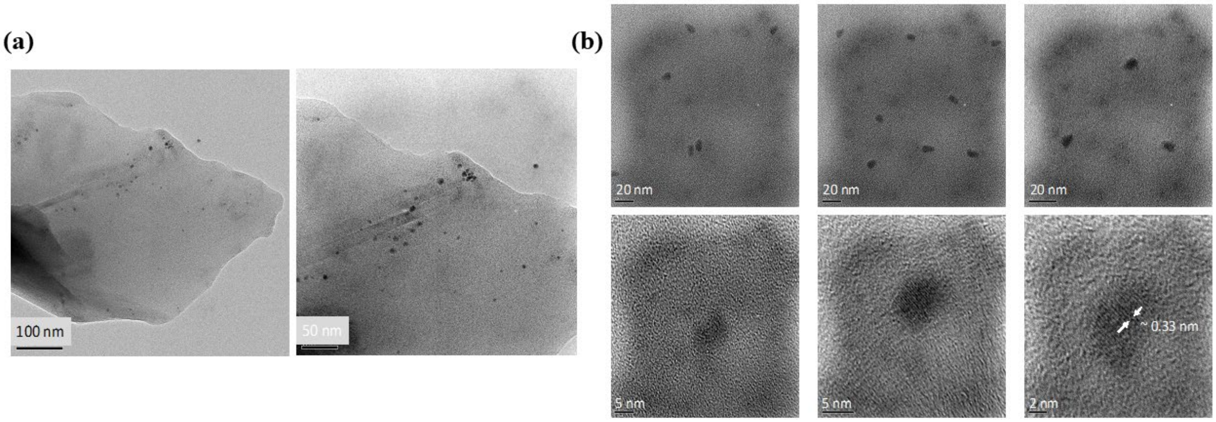

Fig. 4.5. (a) Transmission electron microscopy (TEM) images of graphene-AuNP-CdSe-Ab; **(b)** High-resolution transmission electron microscopy (TEM) images of CdSe quantum dots.

4.2.5 Using the sensing platform for IgG detection:

Human IgG (Abcam, *Cat. # ab91102*) solutions were prepared in different concentrations (10 fM – 1 nM) in the standard buffer and stored at 4°C. 20 µl of the analyte solutions were then added to the spots where the QD-Ab was drop cast. The solution was immediately absorbed by the paper and took around 15 min of incubation at room temperature for drying. Once dried, the fluorescence was recorded from at least three spots for each concentration with a 532 nm excitation using Renishaw InVia micro-spectrometer. For evaluating the specificity of our sensors (discussed later in **Fig. 5**), human IgG solution was prepared in 10% fetal bovine serum (FBS). The data shown is the average fluorescence collected from multiple spots to avoid artefacts arising from inhomogeneous spatial distribution of the antibody/antigen.

4.3 Results and Discussion

As shown in **Fig. 4.1 (a)**, AIDLuQ works in the following manner on graphene paper. Initially, antibody-coated CdSe QDs (QD-Ab) are adsorbed on the surface of graphene paper. The interaction between CdSe QDs and graphene results in the quenching of the emission from the CdSe QDs (see **Fig. 4.3 (b)**). Upon the addition of antigen, some CdSe QDs are raised from the surface, which disrupts quenching from graphene and leads to increased emission of CdSe QDs. In the case of graphene-Au paper (**Fig. 4.1 (b)**), the emission from CdSe QDs is further enhanced due to the presence of surface plasmons of Au NPs.

To test the quenching efficiency of graphene, we dropcasted ~2 μl of 100 nM QD-Abs on both a plain paper and a graphene-coated paper. As seen in **Fig. 4.3 (b)**, there is a significant decrease in the fluorescence intensity in the case of the graphene-coated paper due to fluorescence quenching. This observation concurs with previous studies on highly efficient fluorescence quenching of CdSe/ZnS QDs on few-layer graphene [118]. To validate our hypothesis of AIDLuQ, we recorded emission from streptavidin-coated CdSe QDs on graphene paper in the presence of different biotin concentrations. The complex of biotin and streptavidin is the strongest known non-covalent interaction with an extremely low dissociation constant of 10^{-15} M [134]. We performed a concentration study for the increasing concentrations of biotin and recorded the corresponding fluorescence intensities. As evident from **Fig. 4.6 (a)** below, there is a steady increase in the recorded fluorescence intensity with the increase in the concentration of biotin added to the graphene paper. While we were able to observe significant recovery in emission of CdSe QDs at >1 nM biotin, no discernible changes in the emission of CdSe QDs were observable at lower concentrations.

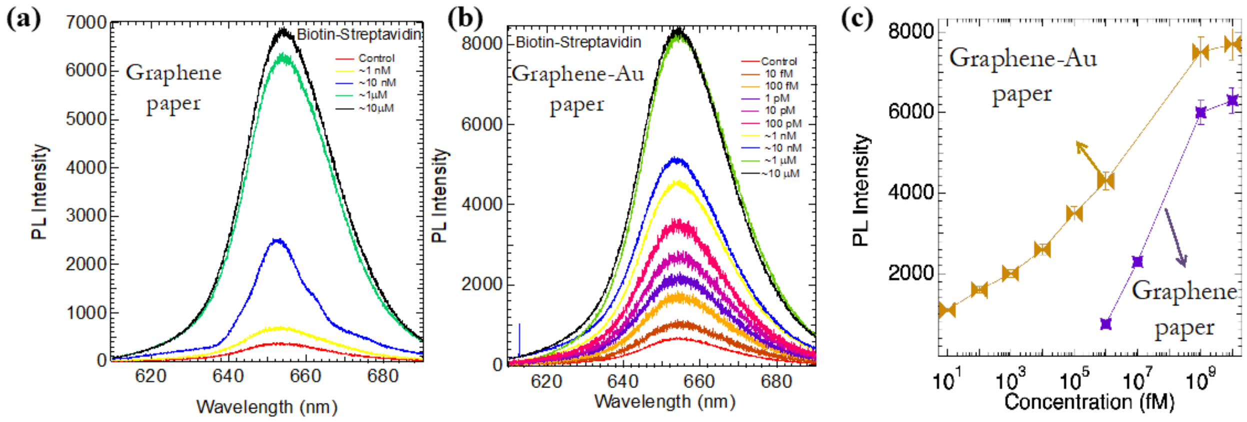

Fig. 4.6. (a) Graphene paper with streptavidin coated CdSe QDs is used for detecting biotin. Upon the addition of biotin, CdSe QDs are lifted off from the surface leading to increase in emission. In this case, a concentration as low as ~1 nM was able to disrupt the quenching. No discernable changes were observed for biotin concentrations below 1 nM; **(b)** A similar experiment of graphene-Au paper with streptavidin-coated QDs demonstrated increased sensitivity due to the presence of Au NPs, which enhance emission by increasing the local electric field; **(c)** A plot showing the background corrected intensity of CdSe QDs emission as a function of biotin concentration. Clearly, graphene-Au provides better sensitivity compared to graphene paper alone.

As mentioned earlier, the graphene paper provides a rapid sensing platform but lacks sensitivity to detect lower concentrations. To achieve better sensitivity, we embedded Au NPs into the graphene platform in order to increase local electric field around CdSe QDs through surface plasmons. The graphene-Au paper exhibited much higher sensitivity even at lower concentrations (~10 fM) of biotin (see **Fig. 4.6 (b)**). As shown in **Fig. 4.6 (c)**, the graphene-Au paper is effective in sensing a wider concentration range from 10 fM-1μM due to the increase in the emission intensity of CdSe QDs. This increase in sensitivity can be rationalized as follows. The quantum yield (QY) of CdSe QDs in the presence of graphene can be expressed as [134]

$$QY = \frac{\Gamma}{\Gamma + \Gamma_{Qu} + k_{nr}} \tag{16}$$

where, Γ is the radiative decay rate, Γ_{Qu} is the non-radiative decay rate arising from the quencher or graphene, k_{nr} is the inherent non-radiative decay rate of CdSe QDs. In the case of graphene paper, the analyte binds the detection antibody and raises CdSe QDs from the surface resulting in a situation where the effects of Γ_{Qu} can be ignored. It is worth noting that the quenching in graphene occurs through resonant energy transfer, which decreases very rapidly with distance d as d^{-6} [118]. Thus, the original QY and the emission of CdSe QDs is recovered. In the presence of Au NPs, the QY of CdSe QDs is altered and may be expressed as

$$QY = \frac{\Gamma + \Gamma_m}{\Gamma + \Gamma_m + \Gamma_{Qu} + k_{nr}} \tag{17}$$

where, Γ_m is the change in the radiative decay rate due to the presence of metallic NPs. When the analyte binds the detection antibody on graphene-Au paper, the quenching effects are removed and the radiative decay rate is increased leading to an increase in QY. While the presence of metallic Au NPs has an oscillatory effect on radiative decay rates, it results in a positive Γ_m when the fluorophore is 5-20 nm away from it [135]–[138]. Given that ~20 nm is the typical dimensions for antigen-antibody pairs that are sensed, the presence of Au NP increases the emission of CdSe QDs even at low concentrations of biotin (**Fig. 4.6 (b)**).

To validate the sensitivity of AIDLuQ platform for specific biomarkers, we evaluated the performance of graphene and graphene-Au papers for detecting human IgG. IgG is an important antibody, which is found in all body fluids and protects against bacterial and viral infections. IgG levels are often measured to diagnose immunodeficiencies, infections, and detect auto-immune diseases.

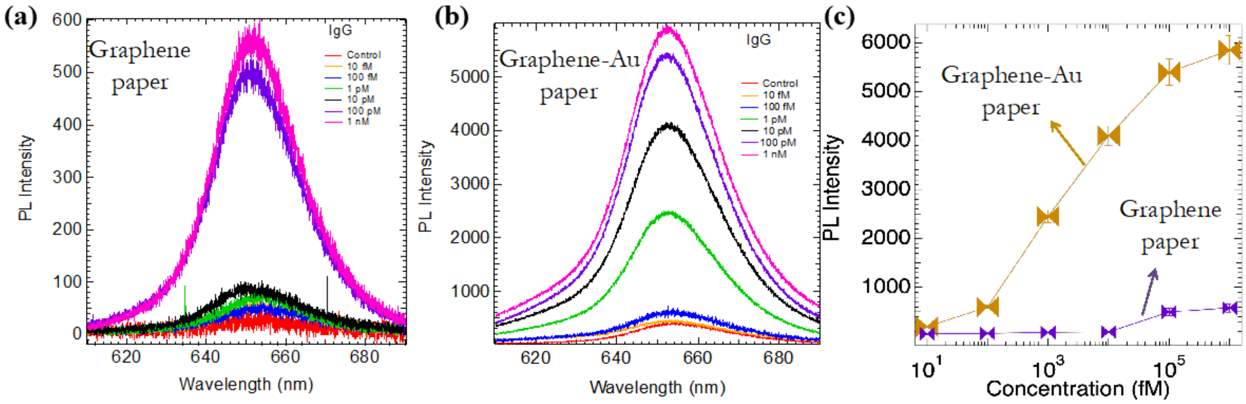

Fig. 4.7. (a) Graphene and **(b)** graphene-AuNP papers with IgG antibody-coated CdSe QDs are used for detecting IgG. Similar to the case of biotin, an increase in the emission of CdSe QDs was observed for both graphene and graphene-Au papers; **(c)** A plot showing the

background corrected intensity of CdSe QDs emission as a function of IgG concentration reveals that it is possible to sense up to ~10 fM of IgG using the graphene-Au platform.

As shown in **Fig. 4.7**, the graphene/graphene-Au platforms performed similar to the case of biotin. While graphene platform was able to sense up to ~10 pM, graphene-Au platform could distinguish up to ~10 fM of IgG (see **Fig. 4.7 (c)** and **Fig. 4.8**). To further test the specificity of our assay, we evaluated the performance of graphene-Au NP platform for sensing IgG in the presence of fetal bovine serum (FBS), which is a complex mixture of several gamma globulins (i.e., antibodies similar to IgG), proteins, amino acids, sugars, lipids, and hormones. Despite the presence of several interfering molecules, we observed that the PL intensity increased with increasing IgG concentration similar to **Fig. 4.7 (c)** (see **Fig. 4.8**). A clear difference could be observed even at IgG concentrations as low as 10 fM.

4.4 Conclusions

In this study, we fabricated a facile single-step immunoassay sensing platform based on graphene's fluorescence quenching ability. Antibody-conjugated CdSe QDs deposited on graphene paper showed low emission due to resonance energy transfer. We hypothesized that the addition of appropriate analyte will bind antibody, raise CdSe QDs from the surface, and consequently help recover its emission. We validated this "analyte-induced disruption in luminescence quenching or AIDLuQ" scheme using two model assays: biotin and IgG. On graphene coated with CdSe-Streptavidin, we were able to discernibly sense up to 1 nM biotin. Similarly, using graphene coated with CdSe-anti-IgG antibodies, we were able to detect up to ~10 pM IgG. To increase the sensitivity of this platform, we embedded Au NPs (~10 nm) into the graphene paper. The graphene-Au paper outperformed the graphene paper and showed ~10 fM sensitivity for biotin and IgG. In summary, spray coated graphene/graphene-Au provides a rapid, specific, and highly sensitive platform for biosensing.

CHAPTER FIVE

A FLEXIBLE PLATFORM FOR RAPID DETECTION OF UROKINASE PLASMINOGEN ACTIVATOR (uPA)

Bipin Sharma *et al.*, "Rapid Detection of Urokinase Plasminogen Activator using Flexible Paper-based Graphene-gold Platform", *Biointerphases*, 15 (2020): 011004. Reproduced with permission from AVS.

5.1 Introduction

The majority of the cancer-related (> 90%) deaths are usually caused due to the metastatic spread of tumor cells [139]–[141]. Despite the emergence of efficient therapeutic strategies to treat primary tumors in recent years, targeting tumor metastasis has not been very successful. A major event in metastasis is the proteolytic degradation of the extracellular matrix that leads to tumor cell invasion, migration, and homing to other organs. Although many protease systems are suspected to be involved in metastasis, several studies have shown that urokinase plasminogen activator (uPA) is causally involved in promoting cancer invasion and metastasis. Particularly, elevated expression of the components of the uPA system has been correlated with adverse patient outcomes in multiple types of cancer (e.g., breast, prostate, colorectal etc.) [141]–[146]. In case of prostate cancer cells, Bekes *et al.* [147] found that uPA participates at an early phase in the initial escape of tumor cells from the primary site. Duffy *et al.* [142] suggested that monitoring uPA levels could very helpful in determining the course of treatment in breast cancer patients. Similarly, uPA also been proposed for monitoring multiple cancer types including prostate cancer [139]–[147].

According to the World Health Organization (WHO), cancer is the second leading cause of death globally, and is responsible for an estimated 9.6 million deaths in 2018 alone [148]. Among 9.6 million deaths, ~70% occurred in low- and middle-income countries due to the lack of access to rapid, inexpensive, and point-of-care diagnostic sensors that could be used in a resource limited setting. According to WHO, in 2017, only 26% of low-income countries reported having pathology services generally available in the public sector. In this regard, there is a great need to develop novel inexpensive sensors that could rapidly diagnose biomarkers such as uPA to improve cancer treatment globally.

Graphene is an ideal platform for biosensing due to its high surface area and unique physicochemical properties. Indeed, graphene biosensors have been used in various modes ranging from electrical/electrochemical to optical detection for sensing a variety of analytes [36], [114]–[117], [149]–[152]. Graphene-based materials (e.g., graphene, graphene oxide, carbon nanotubes etc.) exhibit excellent fluorescence quenching [118], [119] due to non-radiative resonant energy transfer associated with the π-electron cloud. Similarly, noble metal nanoparticles exhibit surface plasmon resonance (SPR) in the visible spectrum [153], [154]. SPR enhances the local electric field, which can induce an increase in quantum yield of fluorescent dyes and quantum dots within its vicinity. Building on SPR and fluorescence quenching of graphene, we fabricated a novel graphene-Au nanoparticle (NP) sensing platform on cellulose-based paper for highly selective sensing of uPA. Using this platform, we achieved a sensitivity as low as 100 pM for uPA even in the presence of complex fluids such as fetal bovine serum. Unlike many existing carbon nanomaterial assays with low sensitivity (~50 nM [155]) or long incubation times, uPA sensing using graphene-Au NP platform is very rapid (<1 hr), highly reliable, inexpensive, and easily scalable.

5.2 Materials and Methods

5.2.1 Fabrication of graphene-Au NP paper:

Exfoliated graphene nanoplatelets (Grade M) were obtained from XG Science (Mason, MI). Detailed atomic force and scanning electron microscopy images of graphene platelets can be referred to in *Chapter 4*, **Fig. 4.2**. A 5 mg/ml suspension of exfoliated graphene nanoplatelets was prepared in 75 ml acetone via tip sonication for 30 minutes (Branson 250W, 1/8" tip sonicator). This solution was then spray-coated onto a A4 printer paper thrice using an industrial spray gun (Iwata 5095 WS400; 1.3 mm nozzle, 29 psi ambient air pressure). During the last coat, 7.5 ml of 1.5 mg/ml ~10 nm Au NPs (Vive Nano, Inc.) was added to obtain a uniform layer of graphene-Au NPs on a standard copier paper. This corresponds to a net areal Au NP density of ~18 μg/cm^2, which was found to be optimal for sensing based on our previous studies [156]. The paper was dried for 15 min in air after each coating. The dried graphene-Au NP papers were stored in dark and dry conditions.

5.2.2 Preparation of standard buffer:

The standard buffer to be used as the solvent for all the experimental studies was prepared by mixing 0.5% (v/v) Tween-20 and 1% (w/v) of BSA in 0.01 M phosphate buffer saline (PBS).

5.2.3 Conjugation of CdSe quantum dots (QDs) with uPA antibodies (Ab):

A mixture was prepared with a final concentration of 100 nM for CdSe QDs (Thermo Fisher Scientific – Invitrogen, Cat #Q10123MP) and 200 µg/ml for uPA Ab (Abcam, Lot # GR131433) in the standard buffer. This mixture was then placed on a shaker at 650 rpm at 4°C for 60 min to ensure the conjugation of antibodies to QDs. These optimal concentrations for QDs and Ab were chosen based on previous studies with other analytes similar to uPA [133], [156]. In this case, the binding of Ab on CdSe QDs is non-specific and is primarily governed by ionic, van der Waals, and hydrophobic forces [133], [157], [158].

5.2.4 Preparation of graphene-Au NP sensing platform:

The graphene-Au NP paper was cut into ~1 cm^2 pieces for sensing experiments and 2 µl of the uPA Ab-conjugated QDs was drop casted on to 1 cm^2 graphene-Au NP paper and left for drying under ambient conditions for around 1 hr. Upon drying, the fluorescence intensity of QDs was measured using a Renishaw InVia micro-spectrometer equipped with a 532 nm laser. The fluorescence intensity was collected from multiple spots per sample (at least 3 different spots) with at least three different replicates (n = 3). A comparison of QD fluorescence on papers with and without graphene is shown in *Chapter 4*, **Fig. 4.3 (b)**.

5.2.5 Using the sensing platform for uPA antigen detection:

Recombinant human uPA protein (Abcam, Lot # GR314499) solution in different concentrations (100 pM – 1 μM) was prepared by dissolving the uPA protein in the standard buffer. Another set of concentrations (100 pM – 100 nM) was prepared in fetal bovine serum (FBS) for the interference study to investigate the selectivity of our assay. All the solutions were stored at 4°C. For sensing experiments, 20 μl of uPA solution of different concentrations (in either standard buffer or FBS) was added to the QD-Ab coated on graphene-Au NP paper. The solutions made in the standard buffer took around 20 min to dry while those made in FBS took around 60 min. Once dry, the fluorescence emission was measured for at least three separate spots using a Renishaw InVia micro-spectrometer at 532 nm. All the data shown hereafter in this chapter are the average fluorescence collected from multiple spots (at least three) to avoid artefacts arising from inhomogeneous distribution of the antibody/antigen.

5.3 Computational Modeling:

5.3.1 Density Functional Theory (DFT):

A DFT calculation with DFT- D2 approach was used to calculate charge transfer between graphene and CdSe QDs. DFT-D2 is a first-principles calculation based on DFT with van der Waals corrections, which is explained in detail in Refs. [159]–[161]. The calculations were performed using the Quantum ESPRESSO code with ultrasoft pseudopotentials for plane wave basis set within generalized gradient approximation (GGA) with the Perdew Burke-Ernzerhof (PBE) exchange correlation functional including London dispersion.

Before stacking up two systems to calculate the charge transfer, each system (viz., graphene and CdSe) was individually optimized to obtain correct parameters such as cell dimensions, k-mesh, and energy cut-off for the plane wave basis. After obtaining the right parameters, the two systems were stacked over one another with a 7 x 7 supercell size (98 Carbon atoms) for graphene matching 4 x 4 supercell size (16 Cd atoms and 16 Se atoms) for the CdSe system. The energy expense of matching two supercells together was within the optimization threshold for energy of 10^{-4} Rydberg. Due to high computational cost, the CdSe bulk structure was approximated to a single layer to be stacked over the graphene layer and relaxed for optimization.

5.4 Results and Discussion

The operation mechanism of our graphene-Au NP platform is described in **Fig. 5.1**. The original fluorescence of CdSe QDs in the QD-antibody (QD-Ab) complex is quenched by graphene due to the interaction between the π-electron cloud of graphene and CdSe QDs. Upon the addition of an analyte (i.e., uPA in this case), the analyte binds with an antibody (Ab) on QDs raising QDs above graphene paper. In other words, as shown in **Fig. 5.1 (d)**, antigen-Ab acts as a spacer between graphene and the QD-Abs ensuing in the reappearance of the fluorescence of QDs. The fluorescence of QDs lifted off the surface by the analyte is further enhanced by the presence of the Au NPs leading to high sensitivity.

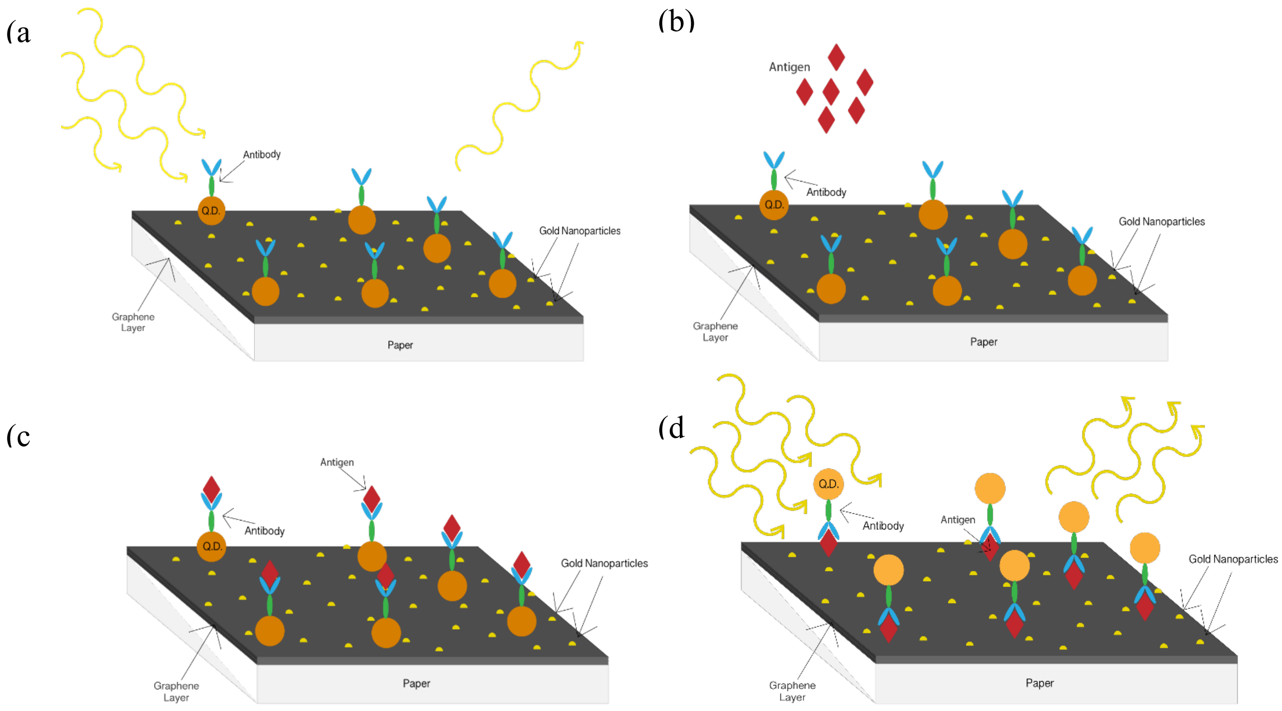

Fig. 5.1. (a) The sensing platform consists of a receptor (uPA antibody) functionalized CdSe quantum dots (QDs) deposited on a cellulose paper coated with graphene. The fluorescence emission from CdSe QDs is quenched when QDs are spatially close to graphene, **(b)** Upon the addition of an analyte (e.g., uPA protein), some CdSe QDs are lifted off from the graphene surface due to binding with the antibodies on the surface of CdSe QDs. The binding increases the spatial gap between CdSe QDs and graphene, which disrupts the quenching and thereby results in an increased emission from QDs, **(c, d)** The number of CdSe QDs lifted off from graphene surface is proportional to the analyte concentration. The plasmonic Au NPs enhance the emission of CdSe QDs. Thus, the increase in the emission of CdSe QDs could be used as a tool to enable highly sensitive detection of low analyte concentrations.

Our DFT calculations showed that graphene-CdSe form a charge transfer complex when they are in close vicinity, which leads to non-radiative fluorescence quenching. The charge transfer profile is shown in **Fig. 5.2 (a) – Fig. 5.2 (c)**. While blue regions show the area from where charge is removed, red color represents regions of charge accumulation. The charge transfer profile along the *z*-axis (perpendicular to graphene and CdSe system plane) is shown in Fig. 2d with graphene at $z = 0$ plane. The shaded area was integrated to obtain the total amount of charge transfer from graphene to CdSe layer, which was about $0.18e$. This charge transfer complex between graphene-CdSe plausibly results in the quenching of CdSe fluorescence.

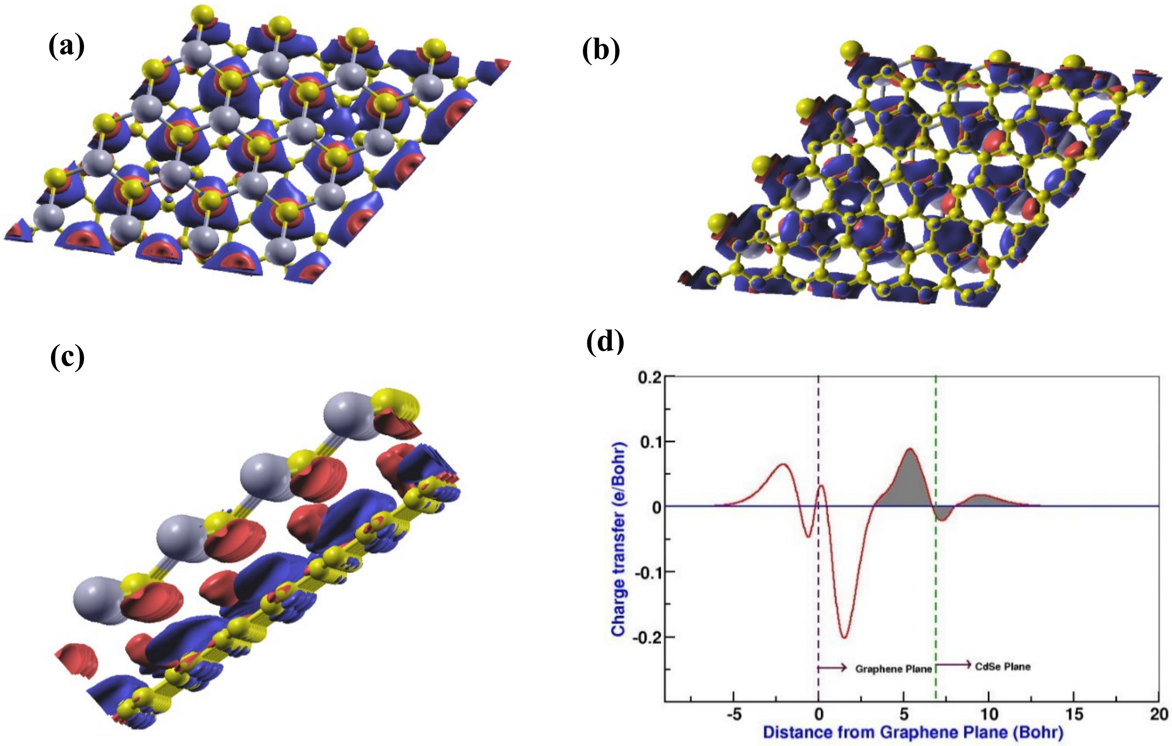

Fig. 5.2. A DFT calculation to evaluate the charge transfer between graphene and CdSe **(a)** Top view with CdSe on top; **(b)** Top view with graphene on top; **(c)** side view for 3D charge transfer pattern. Blue (/red) regions represent areas with charge depletion (/accumulation); **(d)** The charge transfer profile along the z-axis. The area under the shade was integrated to get the total amount of charge transfer from graphene to CdSe layer and was around 0.18e.

The quantum yield (Q) of a fluorophore (CdSe in this case) in the presence of a quencher (graphene in this case) can be expressed as [136]

$$Q = \frac{\Gamma}{\Gamma + \Gamma_{Qu} + k_{nr}} \tag{16}$$

where, Γ is the radiative decay rate, Γ_{Qu} is the non-radiative decay rate arising due to the charge transfer complex between graphene and QDs, and k_{nr} is the inherent non-radiative decay rate of CdSe QDs. Upon raising QDs from the surface of graphene, the effects of Γ_{Qu} become weaker. This leads to an overall increase in the quantum yield. Furthermore, in the presence of Au NPs, the quantum yield of the QDs can be expressed as

$$QY = \frac{\Gamma + \Gamma_m}{\Gamma + \Gamma_m + \Gamma_{Qu} + k_{nr}} \tag{17}$$

where Γ_m is the change in the radiative decay rate due to the presence of Au NPs. When the QDs are raised from the graphene surface in the presence of Au NPs, a positive Γ_m further increases fluorescence when the fluorophore in 5-20 nm away from the Au NPs [135]–[138]. When uPA is added to QD-Ab complex on graphene-Au NP paper, it binds with the uPA antibody on QDs to form a graphene-QD-Ab-uPA complex, which raises QDs above the graphene surface. To test the quenching efficiency of graphene, we drop casted 2 μl of the QD-Ab simultaneously on a normal paper and on the graphene-Au NP paper. As expected, a significant decrease was observed in the emission intensity of QDs on graphene-Au NP paper (see *Chapter 4,* **Fig. 4.3 (b)**). This fluorescence intensity of the graphene-QD-Ab was used as the control intensity.

A concentration study was performed with different concentrations of uPA protein ranging from 100 pM to 1 μM in the standard buffer solution. As shown in **Fig. 5.3 (a)**, a gradual increase is evident in the fluorescence intensity with the increasing concentration of the uPA protein. These intensities are plotted in **Fig. 5.3 (b)**, which displays experimentally recorded average fluorescence intensities (recorded from at least three sampling spots) for different concentrations of uPA. As it can be deduced from **Fig. 5.3 (b)**, concentrations as low as 100 pM of uPA can be detected using this method. The selectivity of our assay was evaluated using proteins other than uPA such as apolipoprotein A-1 (Apo A-1) and immunoglobulin G (IgG) (**Fig. 5.3 (c)** and **Fig. 5.3(d)**). For the selectivity study, 1 nM (which is an order of magnitude above our detection limit of 100 pM for uPA) solutions of IgG and Apo A-1 proteins were prepared in the standard buffer. **Fig. 5.3 (c)** shows the average fluorescence intensities recorded after the addition of the IgG and Apo A-1 solutions respectively. As evident from these results, there was no increase in the emission upon the addition of the IgG or Apo A-1 proteins even at a concentration as high as 1 nM. The uPA antibody is highly selective and thus it does not bind with these proteins (IgG and Apo A-1) and thus eliminates the possibility of formation of a spacer between the QDs and graphene.

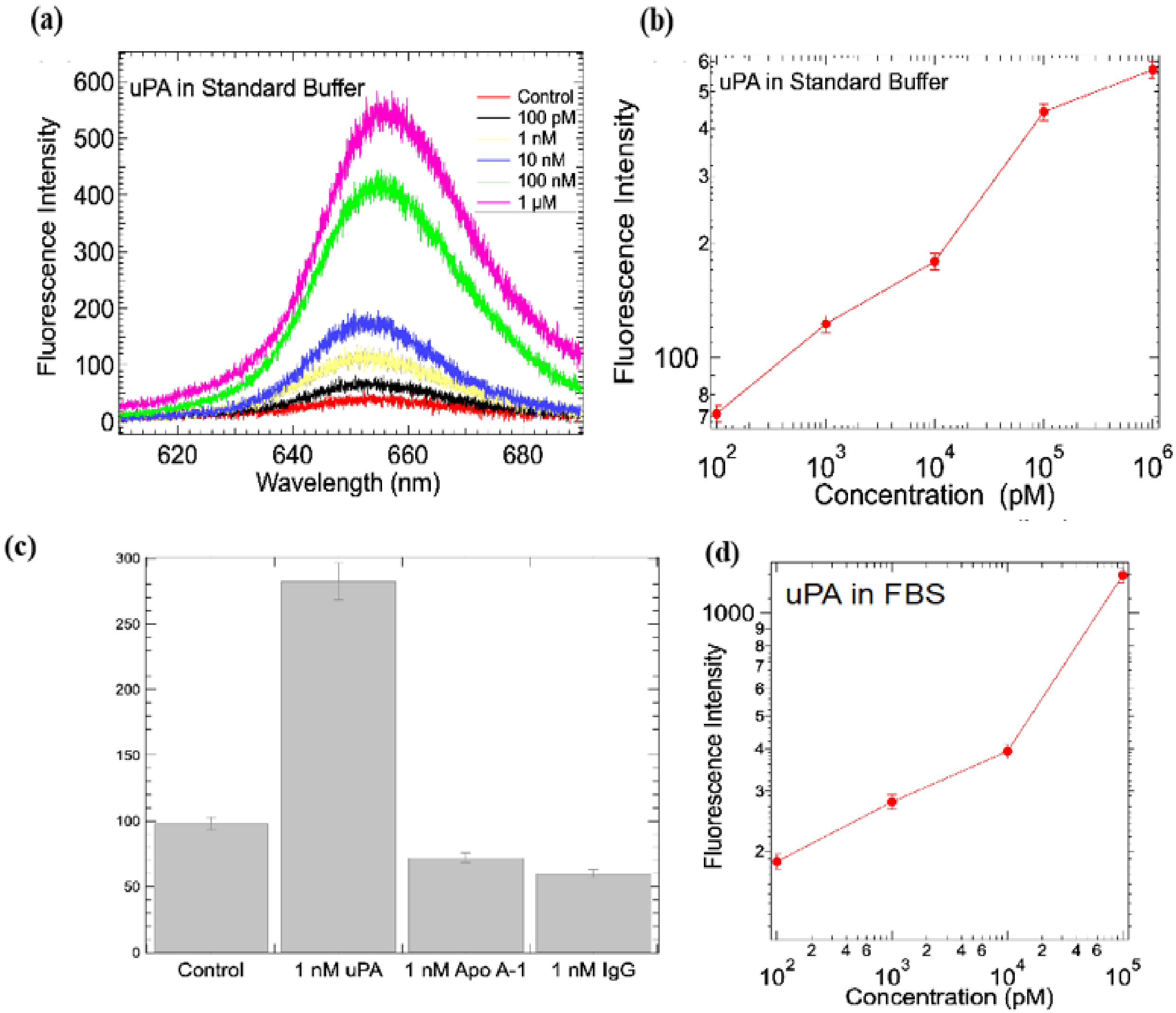

Fig. 5.3. (a) Emission intensities of uPA antibody coated CdSe QDs on graphene-Au NP paper. The emission intensity before the addition of uPA protein is labeled as the control. The addition of uPA protein leads to the raising of the QDs from the surface of graphene, leading

to an increase in the fluorescence intensity; **(b)** A plot showing the dependence of fluorescence intensity on the concentration of uPA. Both these measurements were performed with the standard buffer as the solvent for the uPA antigen. **(c)** Fluorescence intensities obtained by addition of 1 nM of different biomolecules in standard buffer to CdSe QDs coated with uPA antibody. The emission intensity before the addition of any biomolecule is labeled as the control. The addition of uPA protein causes increase in fluorescence intensity while there is almost no significant change in the fluorescence intensity upon addition of non-specific proteins; **(d)** Fluorescence intensities of different concentrations of uPA in FBS. There is a clear trend of increasing fluorescence with increasing uPA concentrations suggesting that our platform can sense uPA even in the presence of a complex milieu containing a wide variety of proteins and lipids.

In order to further evaluate the selectivity of our sensing platforms, solutions of different concentrations of uPA protein were prepared in FBS instead of the standard buffer. FBS is a complex mixture of many proteins, lipids, and is often used as a serum supplement for *in vitro* culturing of eukaryotic cells. Accordingly, detection in FBS is more complex due to the presence of a variety of other proteins and molecules that are similar to uPA in size and structure. Given that our sensing platform is based on the binding of the analyte with the uPA antibodies, we expected that the sensitivity of our platform to not change significantly even in the presence of any interfering molecules. Indeed, as shown in **Fig. 5.3 (d)**, a steady increase in the fluorescence intensity was observed with increasing concentration of uPA in FBS similar to the case of standard buffer confirming the selectivity of our platform.

Lastly, it should be mentioned that our platforms are at least an order of magnitude cheaper than existing ELISA platforms for uPA. Considering that we use ~1.25 mg/cm^2 of Au NPs and ~1-5 mg/cm^2 of graphene (~$450/kg for graphene and $384,000/kg for Au), the price of a 1 cm^2 sensing platform coupon is ~$0.5. Thus, one can fabricate 100 such platforms for $50, which is significantly inexpensive (by an order of magnitude) compared to a standard uncoated 96-well plate uPA ELISA kit (~$539).

5.5 Conclusions

Graphene-Au NP paper was used as a sensing platform for the detection of uPA protein. CdSe QDs coated with uPA antibody showed extremely low fluorescence emission when deposited on the graphene-Au NP paper due to fluorescence quenching. Our DFT calculations suggested that such quenching plausibly arises from charge transfer between graphene and CdSe QDs. The graphene-Au NP platform was able to achieve up to 100 pM uPA sensitivity in the standard buffer. The selectivity of the sensing platform was also evaluated using Apo A-I, IgG, and FBS. No discernible effects of the interfering proteins were observed on the detection of uPA. Although other platforms such as ELISA may provide similar sensitivities, graphene-Au NP platform is inexpensive, flexible, and rapid (~ 1 hr). A main advantage of a flexible sensor is that it can be wrapped or pressed more easily against the patients' fingers to absorb the blood from a simple needle prick similar to existing glucose sensors available in the market. This opens up the possibility of creation of hand-held and point-of-care sensors for low- and middle-income countries.

CHAPTER SIX

SUMMARY AND FUTURE WORK

Most health conditions in humans are accompanied by corresponding biomarkers. The detection of these biomarkers facilitates an early diagnosis and thus have the potential to drastically boost the healthcare industry and the public health in general. Early diagnosis of diseases are known to significantly boost the patient survival rate in life – threatening diseases [162]. Over the years, nanoparticles of various morphologies have been used to improve the performance of biosensors. One of the widely used physical phenomenon in fluorescence-based biosensors is surface plasmon resonance (SPR). Even though SPR has shaped the field of research in ultrasensitive bioassays, the fundamental physical processes behind the effects of size and shape of the nanoparticles on SPR have been largely overlooked.

In our work, we first studied the effects of the shape of Ag nanoparticles in plasmon resonance. Here, we delved into the fundamental physics behind the enhancement (and shift) in emission wavelength corresponding to the shape of the Ag nanoparticles. We then moved on to develop an inexpensive, ultrasensitive biosensing platform that employs nanomaterials to achieve femtomolar detection of biomarkers. These results provide encouragement for future point-of-care devices utilizing the economical nature of our platform for fast and sensitive diagnosis of diseases.

6.1 Point-of-care biomarker detection using AIDLuQ platform

The importance of point-of-care diagnostics is highlighted by the fact that there are many countries with regions completely inaccessible to medical care. In addition, the people in these regions do not have the facilities to get an early diagnosis and might have to wait for a few days to a week and travel afar to get their results. These inconveniences are overcome by the use of mobile health clinics. If these mobile clinics could be equipped with an ultrasensitive diagnosis platform like AIDLuQ, the patients could be tested and the results obtained within the space of an hour or so. This would drastically improve the efficacy of the mobile clinics along with adding to their value and making them more multifunctional. In this setup (**Fig. 6.1**), a simple green pointer laser could be used as the incident light source. We have developed a grating which can be used with a cell phone and the captured light is recorded in the form of a spectrum using an application readily available.

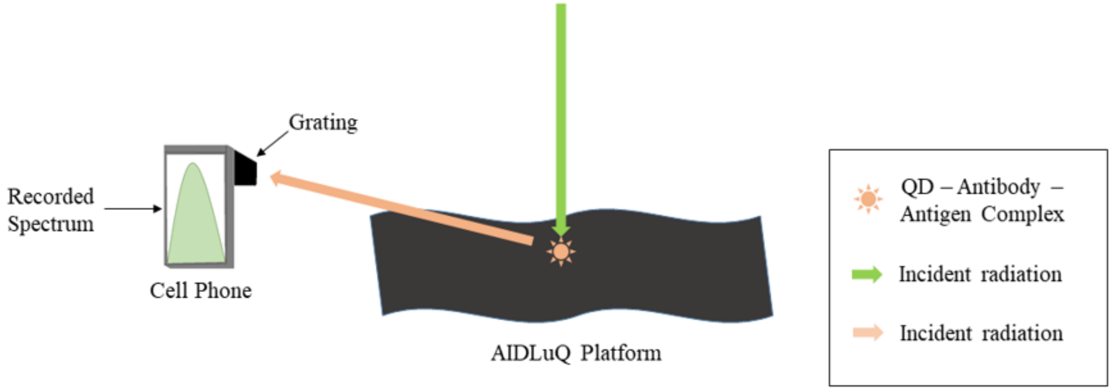

Fig. 6.1 A schematic illustration of the setup for point-of-care diagnostics using AIDLuQ.

6.2 Non – Linear Optics (NLO) in graphene

Optical properties of graphene at the quantum level haven't been fully explored. The next part of future work is aimed at furthering our understanding of the non – linear optical properties of 3-5 layers of graphene. This work will shed light on the type of interactions of graphene with light at the quantum scale. The information obtained can be used to improve the performance or tune the optical side of graphene-light interaction to suit our needs. The NLO in graphene can be studied using a Z-scan setup as shown in **Fig. 6.2**.

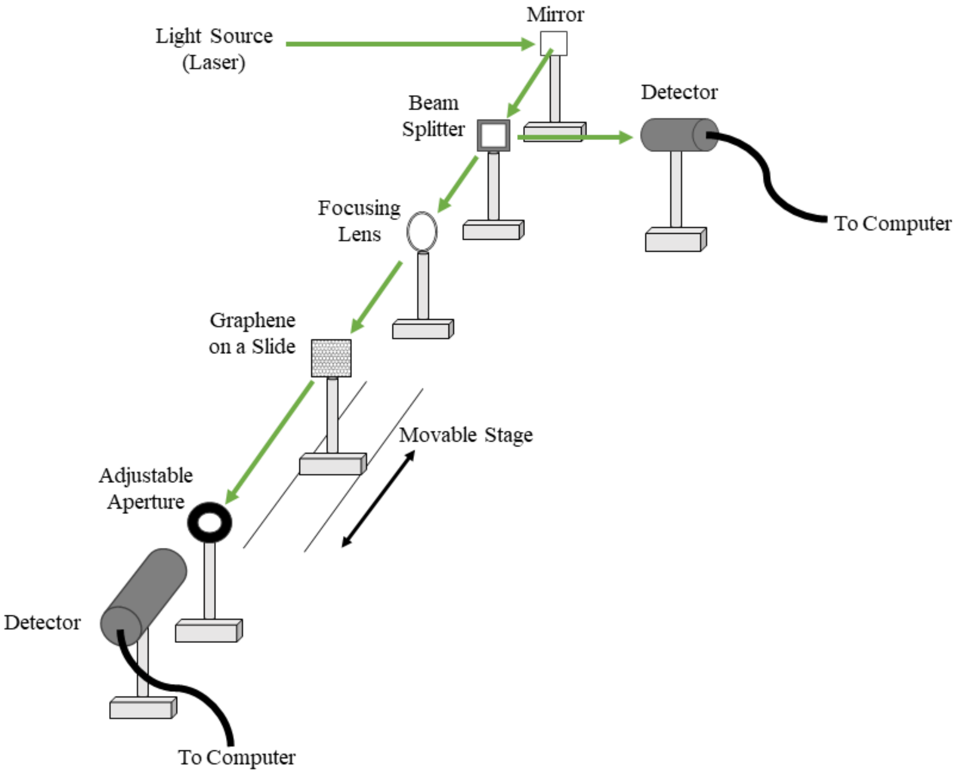

Fig. 6.2. The setup for Z-scan. Z-scan can be used to study the non – linear optical properties of transparent or semi-transparent solids and liquids.

Our previous work has utilized the quenching effects of graphene when a fluorophore is near it. We propose to study the non-linear interactions of graphene with light in the presence of metal nanoparticles in its vicinity. To this end, we have started off with some preliminary experiments in studying the non-linear optical effects in graphene as well as graphene – gold and graphene – silver systems with one coat of gold/silver on graphene. This was followed by a second coating. The results are shown in **Fig. 6.3**.

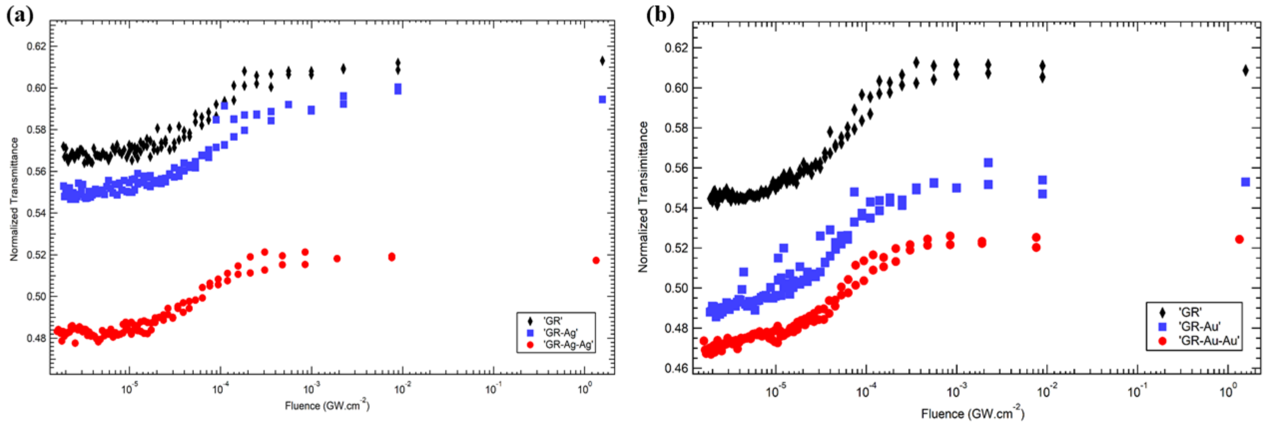

Fig. 6.3. (a) The NLO effects observed in a few-layered graphene (GR), graphene-silver (1 coating) (GR-Ag) and graphene-silver (2 coatings) (GR-Ag-Ag); **(b)** The NLO effects in GR, GR-Au and GR-Au-Au.

A clear trend is observed in the reduction of the normalized transmittance with addition of more layers of gold/graphene. This is due to the simple fact that the light has to now pass through more layers of material and therefore the decrease in transmittance. However, more study into the details of interactions is needed and more data needs to be obtained to study the effect of the size of the coated nanoparticles.

APPENDIX

Glossary of acronyms used in the dissertation

1. CNTs: Carbon Nanotubes
2. SWNTs: Single Walled Nanotubes
3. MWNTs: Multi Walled Nanotubes
4. NPs: Nanoparticles
5. DNA: Deoxyribonucleic Acid
6. RNA: Ribonucleic Acid
7. SPR: Surface Plasmon Resonance
8. LSPR: Localized Surface Plasmon Resonance
9. SPCE: Surface Plasmon Coupled Emission
10. QDs: Quantum Dots
11. EC: Electrochemical
12. UV: Ultraviolet
13. QY: Quantum Yield
14. IR: Infrared
15. SPM: Scanning Probe Microscopy
16. STM: Scanning Tunneling Microscopy
17. SEM: Scanning Electron Microscopy
18. TEM: Transmission Electron Microscopy
19. AFM: Atomic Force Microscopy
20. DSC: Differential Scanning Calorimetry
21. PMT: Photomultiplier Tube
22. RhB: Rhodamine B
23. EEF: Excitation Enhancement Factor
24. AIDLuQ: Analyte Induced Disruption of Luminescence Quenching
25. GERS: Graphene Enhanced Raman Spectroscopy
26. POC: Point-of-care

27. BSA: Bovine Serum Albumin
28. PBS: Phosphate Buffer Saline
29. Ab: Antibody
30. IgG: Immunoglobulin G
31. FBS: Fetal Bovine Serum
32. WHO: World Health Organization
33. DFT: Density Functional Theory
34. uPA: Urokinase Plasminogen Activator
35. ELISA: Enzyme-Linked Immunosorbent Assay

REFERENCES

[1] G. Cao, *Nanostructures and Nanomaterials*. London: Imperial College Press, 2004.

[2] C. N. R. Rao, A. Müller, A. K. Cheetham, and J. Butler, *The Chemistry of Nanomaterials*. Germany: Wiley-VCH, 2004.

[3] M. F. Ashby, P. J. Ferreira, and D. L. Schodek, *Nanomaterials, Nanotechnologies and Design: an Introduction for Engineers and Architects*. China, 2009.

[4] D. R. Thevenot, K. Toth, R. A. Durst, and G. S. Wilson, "Electrochemical biosensors : recommended definitions and classification," *Biosens. Bioelectron.*, vol. 16, pp. 121–131, 2001.

[5] E. Mohanty, S. P.; Kougianos, "Biosensors : A tutorial review," *IEEE Potentials*, vol. 25, pp. 35–40, 2006.

[6] A. P. F. Turner, "Biosensors: sense and sensibility," *Chem. Soc. Rev.*, vol. 42, pp. 3184–3196, 2013.

[7] B. D. Malhotra and C. M. Pandey, *Biosensors : Fundamentals and Applications*. Shrewsbury, UK: Smithers Rapra Technology Ltd., 2017.

[8] S. M. Borisov and O. S. Wolfbeis, "Optical Biosensors," *Chem. Rev.*, vol. 108, pp. 423–461, 2008.

[9] C. Mcdonagh, C. S. Burke, and B. D. MacCraith, "Optical Chemical Sensors," *Chem. Rev.*, vol. 108, pp. 400–422, 2008.

[10] O. S. Wolfbeis, "Fiber-Optic Chemical Sensors and Biosensors," *Anal. Chem.*, vol. 80, pp.

4269–4283, 2008.

[11] A. P. Graham *et al.*, “Carbon Nanotubes for Microelectronics?,” *small*, vol. 1, no. 4, pp. 382–390, 2005.

[12] A. D. Mcfarland and R. P. Van Duyne, “Single Silver Nanoparticles as Real-Time Optical Sensors with Zeptomole Sensitivity,” *Nano Lett.*, vol. 3, no. 8, pp. 1057–1062, 2003.

[13] L. He *et al.*, “Colloidal Au-Enhanced Surface Plasmon Resonance for Ultrasensitive Detection of DNA Hybridization,” *J. Am. Chem. Soc.*, vol. 122, pp. 9071–9077, 2000.

[14] S.-J. Park, T. A. Taton, and C. A. Mirkin, “Array-Based Electrical Detection of DNA with Nanoparticle Probes,” *Science (80-.).*, vol. 295, pp. 1503–1507, 2002.

[15] C. Jianrong, M. Yuqing, H. Nongyue, and W. Xiaohua, “Nanotechnology and biosensors,” *Biotechnol. Adv.*, vol. 22, pp. 505–518, 2004.

[16] J. Wang, “Nanomaterial-based electrochemical biosensors,” *Analyst*, vol. 130, pp. 421–426, 2005.

[17] C. de M. Donega, *Nanoparticles - Workhorses of Nanoscience*. Springer, 2014.

[18] P. C. Ray, “Size and Shape Dependent Second Order Nonlinear Optical Properties of Nanomaterials and Their Application in Biological and Chemical Sensing,” *Chem. Rev.*, vol. 110, pp. 5332–5365, 2010.

[19] M. Holzinger, A. Le Goff, and S. Cosnier, “Nanomaterials for biosensing applications : a review,” *Front. Chem.*, vol. 2, pp. 1–10, 2014.

[20] L. Teixeira and D. Agnol, “Recent Advances in Biosensor Technology for Potential

Applications – An Overview," *Front. Bioeng. Biotechnol.*, vol. 4, pp. 1–9, 2016.

[21] B. Veigas *et al.*, "Noble Metal Nanoparticles for Biosensing Applications," *Sensors*, vol. 12, pp. 1657–1687, 2012.

[22] J. Cabaj and J. Sołoducho, "Nano-Sized Elements in Electrochemical Biosensors," *Mater. Sci. Appl.*, vol. 5, pp. 752–766, 2014.

[23] P. R. Solanki, A. Kaushik, V. V Agrawal, and B. D. Malhotra, "Nanostructured metal oxide-based biosensors," *NPG Asia Mater.*, vol. 3, no. 1, pp. 17–24, 2011.

[24] V. V Mody, R. Siwale, A. Singh, and H. R. Mody, "Introduction to metallic nanoparticles," *J. Pharm. Bioall. Sci.*, vol. 4, pp. 282–289, 2010.

[25] C. J. Murphy *et al.*, "Anisotropic Metal Nanoparticles : Synthesis, Assembly, and Optical Applications," *J. Phys. Chem. B*, vol. 109, pp. 13857–13870, 2005.

[26] T. A. Klar, B. T. K. Sau, A. L. Rogach, and F. Ja, "Properties and Applications of Colloidal Nonspherical Noble Metal Nanoparticles," *Adv. Mater.*, vol. 22, pp. 1805–1825, 2010.

[27] M. Shah, V. D. Badwaik, C. Agrisciences, Y. Kherde, and H. Waghwani, "Gold nanoparticles : various methods of synthesis and antibacterial applications," *Front. Biosci.*, vol. 19, pp. 1320–1344, 2014.

[28] X. Ren, X. Meng, D. Chen, F. Tang, and J. Jiao, "Using silver nanoparticle to enhance current response of biosensor," *Biosens. Bioelectron.*, vol. 21, pp. 433–437, 2005.

[29] J. Lin, C. He, Y. Zhao, and S. Zhang, "One-step synthesis of silver nanoparticles / carbon nanotubes / chitosan film and its application in glucose biosensor," *Sensors Actuators B*

Chem., vol. 137, pp. 768–773, 2009.

[30] A. E. Nel *et al.*, “Understanding biophysicochemical interactions at the nano-bio interface,” *Nat. Mater.*, vol. 8, no. 7, pp. 543–557, 2009.

[31] S. Iijima and T. Ichihashi, “Single-shell carbon nanotubes of 1-nm diameter,” *Nature*, no. 3, pp. 603–605, 1993.

[32] O. A. Shenderova, V. V. Zhirnov, and D. W. Brenner, “Carbon nanostructures,” *Crit. Rev. Solid State Mater. Sci.*, vol. 27, no. 3–4, pp. 227–356, 2002.

[33] F. R. Baptista, S. A. Belhout, S. Giordani, and S. J. Quinn, “Recent developments in carbon nanomaterial sensors,” *Chem. Soc. Rev.*, vol. 44, no. 13, pp. 4433–4453, 2015.

[34] A. Aqel, K. M. M. A. El-Nour, R. A. A. Ammar, and A. Al-Warthan, “Carbon nanotubes, science and technology part (I) structure, synthesis and characterisation,” *Arab. J. Chem.*, vol. 5, no. 1, pp. 1–23, 2012.

[35] X. Yu *et al.*, “Carbon Nanotube Amplification Strategies for Highly Sensitive Immunodetection of Cancer Biomarkers,” *J. Am. Chem. Soc.*, vol. 128, pp. 494–500, 2006.

[36] S. Ji *et al.*, “Carbon nanotubes in cancer diagnosis and therapy,” *Biochim. Biophys. Acta*, vol. 1806, pp. 29–35, 2010.

[37] M. B. Lerner *et al.*, “Hybrids of a Genetically Engineered Antibody and a Carbon Nanotube Transistor for Detection of Prostate Cancer Biomarkers,” *ACS Nano*, vol. 6, no. 6, pp. 5143–5149, 2012.

[38] M. Das, C. Dhand, G. Sumana, A. K. Srivastava, R. Nagarajan, and B. D. Malhotra,

"Electrophoretically fabricated core-shell CNT-DNA biowires for biosensing," *J. Mater. Chem.*, vol. 22, pp. 2727–2732, 2012.

[39] C. Singh *et al.*, "Sensors and Actuators B : Chemical Carboxylated multiwalled carbon nanotubes based biosensor for aflatoxin detection," *Sensors Actuators B. Chem.*, vol. 185, pp. 258–264, 2013.

[40] K. K. Reza, S. Srivastava, S. K. Yadav, and A. M. Biradar, "Biofunctionalized carbon nanotubes platform for biomedical applications," *Mater. Lett.*, vol. 126, pp. 126–130, 2014.

[41] G. A. Zelada-Guillén, A. Tweed-Kent, M. Niemann, H. U. Göringer, J. Riu, and F. X. Rius, "Ultrasensitive and real-time detection of proteins in blood using a potentiometric carbon-nanotube aptasensor," *Biosens. Bioelectron.*, vol. 41, no. 1, pp. 366–371, 2013.

[42] L. Tang, Y. Wang, Y. Li, H. Feng, J. Lu, and J. Li, "Preparation, Structure, and Electrochemical Properties of Reduced Graphene Sheet Films," *Adv. Funct. Mater.*, vol. 19, pp. 2782–2789, 2009.

[43] Y. Zhu *et al.*, "Graphene and Graphene Oxide: Synthesis, Properties, and Applications," *Adv. Mater.*, vol. 22, pp. 3906–3924, 2010.

[44] A. A. Balandin, "Thermal properties of graphene and nanostructured carbon materials," *Nat. Mater.*, vol. 10, pp. 569–581, 2011.

[45] A. H. C. Neto, F. Guinea, N. M. R. Peres, K. S. Novoselov, and A. K. Geim, "The electronic properties of graphene," *Rev. Mod. Phys.*, vol. 81, pp. 109–162, 2009.

[46] H. Pei *et al.*, "A Graphene-Based Sensor Array for High-Precision and Adaptive Target Identification with Ensemble Aptamers," *J. Am. Chem. Soc.*, vol. 134, pp. 13843–13849,

2012.

[47] L. Gao *et al.*, “Highly sensitive detection for proteins using graphene oxide-aptamer based sensors,” *Nanoscale*, vol. 7, pp. 10903–10907, 2015.

[48] Y. Su and Y. Lv, “Graphene and graphene oxides: recent advances in chemiluminescence and electrochemiluminescence,” *RSC Adv.*, vol. 4, pp. 29324–29339, 2014.

[49] Y. Bai, F. Feng, L. Zhao, Z. Chen, H. Wang, and Y. Duan, “A turn-on fluorescent aptasensor for adenosine detection based on split aptamers and graphene oxide,” *Analyst*, vol. 139, pp. 1843–1846, 2014.

[50] A. P. Alivisatos, “Semiconductor Clusters, Nanocrystals, and Quantum Dots,” *Science (80-.).*, vol. 271, no. 5251, pp. 933–937, 1996.

[51] T. Takagahara and K. Takeda, “Theory of the quantum confinement effect on excitons in quantum dots of indirect-gap materials,” *Phys. Rev. B*, vol. 46, no. 23, pp. 578–581, 1992.

[52] O. Stier, M. Grundmann, and D. Bimberg, “Electronic and optical properties of strained quantum dots modeled by 8-band $k \cdot p$ theory,” *Phys. Rev. B*, vol. 59, no. 8, pp. 5688–5701, 1999.

[53] H. Haug and S. W. Koch, *Quantum Theory of the Optical and Electronic Properties of Semiconductors*. Singapore: World Scientific Publishing, 2004.

[54] H. Sahoo, “Förster resonance energy transfer – A spectroscopic nanoruler: Principle and applications,” *J. Photochem. Photobiol. C Photochem. Rev.*, vol. 12, pp. 20–30, 2011.

[55] J. Zhang and M. D. Allen, “FRET-based biosensors for protein kinases: illuminating the

kinome," *Mol. Biosyst.*, vol. 3, pp. 759–765, 2007.

[56] M. F. Frasco and N. Chaniotakis, "Semiconductor Quantum Dots in Chemical Sensors and Biosensors," *Sensors*, vol. 9, pp. 7266–7286, 2009.

[57] X. Michalet *et al.*, "Quantum Dots for Live Cells, in Vivo Imaging, and Diagnostics," *Science (80-.).*, vol. 307, pp. 538–545, 2005.

[58] F. S. Ligler, *Fluorescence-Based Optical Biosensors*. Springer, 2008.

[59] M. Staiano, P. Bazzicalupo, S. D. Auria, and M. Rossi, "Glucose biosensors as models for the development of advanced protein-based biosensors," pp. 354–362, 2005.

[60] M. Strianese, M. Staiano, G. Ruggiero, T. Labella, C. Pellecchia, and S. D'Auria, "Fluorescence-Based Biosensors," in *Spectroscopic Methods of Analysis*, 1st ed., W. M. Bujalowski, Ed. Springer, 2012, pp. 193–216.

[61] X. Fan, I. M. White, S. I. Shopova, H. Zhu, J. D. Suter, and Y. Sun, "Sensitive optical biosensors for unlabeled targets: A review," *Anal. Chim. Acta*, vol. 620, pp. 8–26, 2008.

[62] P. Singh, *Surface Plasmon Resonance*. Nova Science Publishers, 2014.

[63] J. M. Brockman, B. P. Nelson, and R. M. Corn, "Surface Plasmon Resonance Imaging Measurements of Ultrathin Organic Films," *Annu. Rev. Phys. Chem.*, vol. 51, pp. 41–63, 2000.

[64] R. P. Van Duyne, "Molecular Plasmonics," *Science (80-.).*, vol. 306, pp. 985–986, 2004.

[65] W. Knoll, "Interfaces and Thin Films As Seen By Bound Electromagnetic Waves," *Annu. Rev. Phys. Chem.*, vol. 49, pp. 569–638, 1998.

[66] C. R. Yonzon, E. Jeoung, S. Zou, G. C. Schatz, M. Mrksich, and R. P. Van Duyne, “A comparative analysis of localized and propagating surface plasmon resonance sensors: The binding of Concanavalin A to a monosaccharide functionalized self-assembled monolayer,” *Journal of the American Chemical Society*, vol. 126. pp. 12669–12676, 2004.

[67] A. J. Haes and R. P. Van Duyne, “A unified view of propagating and localized surface plasmon resonance biosensors,” *Anal. Bioanal. Chem.*, vol. 379, pp. 920–930, 2004.

[68] A. J. Haes, C. L. Haynes, A. D. Mcfarland, and G. C. Schatz, “Plasmonic Materials for Surface-Enhanced Sensing and,” *Mater. Res. Bull.*, vol. 30, pp. 368–375, 2005.

[69] K. A. Willets and R. P. Van Duyne, “Localized Surface Plasmon Resonance Spectroscopy and Sensing,” *Annu. Rev. Phys. Chem.*, vol. 58, pp. 267–297, 2007.

[70] K. Kneipp, M. Moskovits, and H. Kneipp, Eds., *Surface-Enhanced Raman Scattering*. Springer, 2006.

[71] K. L. Kelly, E. Coronado, L. L. Zhao, and G. C. Schatz, “The optical properties of metal nanoparticles: The influence of size, shape, and dielectric environment,” *J. Phys. Chem. B*, vol. 107, pp. 668–677, 2003.

[72] C. F. Bohren and D. R. Huffman, *Absorption and scattering of light by small particles*. Wiley-VCH, 1998.

[73] G. Mie, “Contributions to the optics of turbid media, particularly of colloidal metal solutions,” *Ann. Phys.*, vol. 25, no. 3, pp. 377–445, 1908.

[74] L. S. Jung, C. T. Campbell, T. M. Chinowsky, M. N. Mar, and S. S. Yee, “Quantitative Interpretation of the Response of Surface Plasmon Resonance Sensors to Adsorbed Films,”

Langmuir, vol. 14, pp. 5636–5648, 1998.

[75] A. J. Haes and R. P. Van Duyne, "A Nanoscale Optical Biosensor: Sensitivity and Selectivity of an Approach Based on the Localized Surface Plasmon Resonance Spectroscopy of Triangular Silver Nanoparticles," *Journal of the American Chemical Society*, vol. 124. pp. 10596–10604, 2002.

[76] R. M. A. Azzam and N. M. Bashara, *Ellipsometry and polarised light*. Amsterdam: Elsevier, 1987.

[77] M. Born and E. Wolf, *Principles Of Optics*, 6th ed. Oxford: Pergamon Press Ltd., 1980.

[78] W. M. Albers and I. Vikholm-Lundin, "Surface Plasmon Resonance on Nanoscale Organic Films," in *Nano-Bio-Sensing*, S. Carrara, Ed. Springer, 2011, pp. 83–126.

[79] E. Kretschmann and H. Raether, "Radiative Decay of Non Radiative Surface Plasmons Excited by Light," *Zeitschrift fur Naturforsch. - Sect. A J. Phys. Sci.*, vol. 23, pp. 2135–2136, 1968.

[80] A. Otto, "Excitation of Nonradiative Surface Plasma Waves in Silver by the Method of Frustrated Total Reflection," *Zeitschrift für Phys.*, vol. 216, pp. 398–410, 1968.

[81] J. Dostálek and W. Knoll, "Biosensors based on surface plasmon-enhanced fluorescence spectroscopy (Review)," *Biointerphases*, vol. 3, pp. FD12–FD22, 2008.

[82] W. H. Weber and C. F. Eagen, "Energy transfer from an excited dye molecule to the surface plasmons of an adjacent metal," *Opt. Lett.*, vol. 4, no. 8, pp. 236–238, 1979.

[83] S. C. Kitson, W. L. Barnes, J. R. Sambles, and N. P. K. Cotter, "Excitation of molecular

fluorescence via surface plasmon polaritons," *J. Mod. Opt.*, vol. 43, no. 3, pp. 573–582, 1996.

[84] J. M. Hollas, *Modern Spectroscopy*, 4th ed. John Wiley & Sons, Inc., 2004.

[85] A. Jabłoński, "Über den Mechanismus der Photolumineszenz von Farbstoffphosphoren (On the mechanism of photoluminescence from dye phosphors)," *Zeitschrift für Phys.*, vol. 94, pp. 38–46, 1935.

[86] J. R. Albani, "Fluorescence: Principles and Observables," in *Structure and Dynamics of Macromolecules: Absorption and Fluorescence Studies*, Elsevier B.V., 2004, pp. 55–98.

[87] J. R. Lakowicz, "Instrumentation for Fluorescence Spectroscopy," in *Principles of Fluorescence Spectroscopy*, 3rd ed., Boston: Springer, 2006, pp. 27–61.

[88] R. Singh, "C. V. Raman and the Discovery of the Raman Effect," *Phys. Perspect.*, vol. 4, pp. 399–420, 2002.

[89] C. V. Raman, "A new radiation," *Indian J. Phys.*, vol. 2, pp. 387–398, 1928.

[90] J. R. Ferraro, K. Nakamoto, and C. W. Brown, *Introductory Raman Spectroscopy*, vol. 4, no. 3. Elsevier, 2003.

[91] G. Turrell and J. Corset, Eds., *Raman Microscopy: Developments and Applications*, vol. 1. San Diego: Elsevier, 1996.

[92] R. B. Thompson, *Fluorescence Sensors and Biosensors*. CRC Press (Taylor and Francis Group), 2006.

[93] Y. Fu, J. Zhang, and J. R. Lakowicz, "Plasmonic Enhancement of Single-Molecule

Fluorescence Near a Silver Nanoparticle," *J. Fluoresc.*, vol. 17, pp. 811–816, 2007.

[94] O. S. Wolfbeis, "Materials for fluorescence-based optical chemical sensors," *J. Mater. Chem.*, vol. 15, pp. 2657–2669, 2005.

[95] B. Valeur and M. N. Berberan-Santos, "Chemical Sensing via Fluorescence," *Mol. Fluoresc.*, pp. 409–478, 2012.

[96] M. E. Stewart *et al.*, "Nanostructured Plasmonic Sensors," *Chem. Rev.*, vol. 108, pp. 494–521, 2008.

[97] J. C. Pickup, F. Hussain, N. D. Evans, O. J. Rolinski, and D. J. S. Birch, "Fluorescence-based glucose sensors," *Biosens. Bioelectron.*, vol. 20, pp. 2555–2565, 2005.

[98] G. Orellana, "Fluorescence - Based Sensors," in *Optical Chemical Sensors*, F. Baldini, A. N. Chester, J. Homola, and S. Martellucci, Eds. Dordrecht, The Netherlands: Springer, 2004, pp. 99–116.

[99] E. Zamir, P. H. M. Lommerse, A. Kinkhabwala, H. E. Grecco, and P. I. H. Bastiaens, "Fluorescence fluctuations of quantum-dot sensors capture intracellular protein interaction dynamics," *Nat. Methods*, vol. 7, pp. 295–298, 2010.

[100] M. Sauer, "Single-molecule-sensitive fluorescent sensors based on photoinduced intramolecular charge transfer," *Angew. Chemie - Int. Ed.*, vol. 42, pp. 1790–1793, 2003.

[101] S. Kruss, A. J. Hilmer, J. Zhang, N. F. Reuel, B. Mu, and M. S. Strano, "Carbon nanotubes as optical biomedical sensors," *Adv. Drug Deliv. Rev.*, vol. 65, pp. 1933–1950, 2013.

[102] H. Mertens, A. F. Koenderink, and A. Polman, "Plasmon-enhanced luminescence near

noble-metal nanospheres: Comparison of exact theory and an improved Gersten and Nitzan model," *Phys. Rev. B - Condens. Matter Mater. Phys.*, vol. 76, p. 115123, 2007.

[103] I. Gryczynski, J. Malicka, Z. Gryczynski, and J. R. Lakowicz, "Surface Plasmon-Coupled Emission with Gold Films," *J. Phys. Chem. B*, vol. 108, pp. 12568–12574, 2004.

[104] S.-H. Cao, W.-P. Cai, Q. Liu, and Y.-Q. Li, "Surface Plasmon–Coupled Emission: What Can Directional Fluorescence Bring to the Analytical Sciences?," *Annu. Rev. Anal. Chem.*, vol. 5, pp. 317–336, 2012.

[105] P. Mulpur, S. Yadavilli, A. M. Rao, V. Kamisetti, and R. Podila, "MoS2/WS2/BN-Silver Thin-Film Hybrid Architectures Displaying Enhanced Fluorescence via Surface Plasmon Coupled Emission for Sensing Applications," *ACS Sensors*, vol. 1, pp. 826–833, 2016.

[106] P. Anger, P. Bharadwaj, and L. Novotny, "Enhancement and Quenching of Single-Molecule Fluorescence," *Phys. Rev. Lett.*, vol. 96, p. 113002, 2006.

[107] P. Ginzburg, "Cavity quantum electrodynamics in application to plasmonics and metamaterials," *Rev. Phys.*, vol. 1, pp. 120–139, 2016.

[108] D. D. Evanoff and G. Chumanov, "Size-Controlled Synthesis of Nanoparticles. 2. Measurement of Extinction, Scattering, and Absorption Cross Sections," *J. Phys. Chem. B*, vol. 108, pp. 13957–13962, 2004.

[109] X. Qian and H. S. Park, "The influence of mechanical strain on the optical properties of spherical gold nanoparticles," *J. Mech. Phys. Solids*, vol. 58, pp. 330–345, 2010.

[110] F. S. Ameer *et al.*, "Tuning Localized Surface Plasmon Resonance Wavelengths of Silver Nanoparticles by Mechanical Deformation," *J. Phys. Chem. C*, vol. 120, pp. 20886–20895,

2016.

[111] P. B. Johnson and R. W. Christy, “Optical Constants of the Nobel Metals,” *Phys. Rev. B*, vol. 6, pp. 4370–4379, 1972.

[112] Y. S. Kim, P. T. Leung, and T. F. George, “Classical Decay Rates for Molecules in the Presence of a Spherical Surface: A Complete Treatment,” *Surf. Sci.*, vol. 195, pp. 1–14, 1988.

[113] H. Chew, “Transition rates of atoms near spherical surfaces,” *J. Chem. Phys.*, vol. 87, pp. 1355–1360, 1987.

[114] C. I. L. Justino, A. R. Gomes, A. C. Freitas, A. C. Duarte, and T. A. P. Rocha-Santos, “Graphene based sensors and biosensors,” *TrAC - Trends Anal. Chem.*, vol. 91, pp. 53–66, 2017.

[115] M. Pumera, “Graphene in biosensing,” *Mater. Today*, vol. 14, pp. 308–315, 2011.

[116] S. Pandit, “Graphene and Graphene Oxide Based Biosensors,” *Res. Gate*, pp. 1–6, 2015.

[117] Y. Shao, J. Wang, H. Wu, J. Liu, I. A. Aksay, and Y. Lin, “Graphene Based Electrochemical Sensors and Biosensors: A Review,” *Electroanalysis*, vol. 22, pp. 1027–1036, 2010.

[118] Z. Chen, S. Berciaud, C. Nuckolls, T. F. Heinz, and L. E. Brus, “Energy Transfer from Individual Semiconductor Nanocrystals to Graphene,” *ACS Nano*, vol. 4, pp. 2964–2968, 2010.

[119] A. Kasry, A. A. Ardakani, G. S. Tulevski, B. Menges, M. Copel, and L. Vyklicky, “Highly Efficient Fluorescence Quenching with Graphene,” *J. Phys. Chem. C*, vol. 116, pp. 2858–

2862, 2012.

[120] M. Dong *et al.*, “Polymerizing dopamine onto Q-graphene scaffolds towards the fluorescent nanocomposites with high aqueous stability and enhanced fluorescence for the fluorescence analysis and imaging of copper ions,” *Sensors Actuators B Chem.*, vol. 232, pp. 234–242, 2016.

[121] Y. Cai *et al.*, “Q-Graphene-loaded metal organic framework nanocomposites with water-triggered fluorescence turn-on: Fluorimetric test strips for directly sensing trace water in organic solvents,” *Chem. Commun.*, vol. 54, pp. 13595–13598, 2018.

[122] H. Wang, S. Li, Y. Si, Z. Sun, S. Li, and Y. Lin, “Recyclable enzyme mimic of cubic Fe3O4 nanoparticles loaded on graphene oxide-dispersed carbon nanotubes with enhanced peroxidase-like catalysis and electrocatalysis,” *J. Mater. Chem. B*, vol. 2, pp. 4442–4448, 2014.

[123] H. Wang *et al.*, “Platinum nanocatalysts loaded on graphene oxide-dispersed carbon nanotubes with greatly enhanced peroxidase-like catalysis and electrocatalysis activities,” *Nanoscale*, vol. 6, pp. 8107–8116, 2014.

[124] R. R. Nair *et al.*, “Fine Structure Constant Defines Visual Transparency of Graphene,” *Science (80-.).*, vol. 320, p. 1308, 2008.

[125] N. Zhang, L. Tong, and J. Zhang, “Graphene-Based Enhanced Raman Scattering toward Analytical Applications,” *Chem. Mater.*, vol. 28, pp. 6426–6435, 2016.

[126] D. Wild, R. John, C. Sheehan, S. Binder, and J. He, *The Immunoassay Handbook*, 4th ed. Amsterdam: Elsevier, 2013.

[127] J. Wu, Z. Fu, F. Yan, and H. Ju, “Biomedical and clinical applications of immunoassays and immunosensors for tumor markers,” *TrAC - Trends Anal. Chem.*, vol. 26, no. 7, pp. 679–688, 2007.

[128] Y. R. Park, Y. Lee, G. Lee, J. H. Lee, and S.-Y. Shin, “Smartphone Applications with Sensors Used in a Tertiary Hospital - Current Status and Future Challenges,” *Sensors*, vol. 15, pp. 9854–9869, 2015.

[129] C. I. L. Justino, A. C. Duarte, and T. A. P. Rocha-Santos, “Critical overview on the application of sensors and biosensors for clinical analysis,” *TrAC - Trends Anal. Chem.*, vol. 85, pp. 36–60, 2016.

[130] M. Kemmler *et al.*, “Compact point-of-care system for clinical diagnostics,” *Sensors Actuators, B Chem.*, vol. 139, no. 1, pp. 44–51, 2009.

[131] P. Mulpur *et al.*, “Amplification of Surface Plasmon Coupled Emission from Graphene-Ag Hybrid Films,” *J. Phys. Chem. C*, vol. 117, pp. 17205–17210, 2013.

[132] B. Law, C. G. Copley, R. A. Biddlecombe, M. J. Warwick, M. D. Malone, and W. J. Jenner, *Immunoassays: A Practical Guide*, vol. 3–4. London: Taylor and Francis Ltd., 2005.

[133] B. Saha, T. H. Evers, and M. W. J. Prins, “How Antibody Surface Coverage on Nanoparticles Determines the Activity and Kinetics of Antigen Capturing for Biosensing,” *Anal. Chem.*, vol. 86, pp. 8158–8166, 2014.

[134] N. M. Green, “The Use of [C14]Biotin for Kinetic Studies and for Assay,” *Biochem. J.*, vol. 89, pp. 585–591, 1963.

[135] J. W. Goodman *et al.*, *Progress in Optics*, 8th ed. Amsterdam: North-Holland Publishing

Company, 1970.

[136] J. R. Lakowicz, “Radiative Decay Engineering: Biophysical and Biomedical Applications,” *Anal. Biochem.*, vol. 298, pp. 1–24, 2001.

[137] W. L. Barnes, “Fluorescence near interfaces: The role of photonic mode density,” *J. Mod. Opt.*, vol. 45, pp. 661–699, 1998.

[138] R. M. Amos and W. L. Barnes, “Modification of spontaneous emission lifetimes in the presence of corrugated metallic surfaces,” *Phys. Rev. B - Condens. Matter Mater. Phys.*, vol. 59, pp. 7708–7714, 1999.

[139] B. Weigelt, J. L. Peterse, and L. J. Van’t Veer, “Breast cancer metastasis: Markers and models,” *Nat. Rev. Cancer*, vol. 5, pp. 591–602, 2005.

[140] P. Mehlen and A. Puisieux, “Metastasis: a question of life or death,” *Nat. Rev. Cancer*, vol. 6, pp. 449–458, Jun. 2006.

[141] N. Mahmood, C. Mihalcioiu, and S. A. Rabbani, “Multifaceted Role of the Urokinase-Type Plasminogen Activator (uPA) and Its Receptor (uPAR): Diagnostic, Prognostic, and Therapeutic Applications,” *Front. Oncol.*, vol. 8, pp. 1–21, Feb. 2018.

[142] M. J. Duffy and C. Duggan, “The urokinase plasminogen activator system: a rich source of tumour markers for the individualised management of patients with cancer,” *Clin. Biochem.*, vol. 37, pp. 541–548, Jul. 2004.

[143] M. J. Duffy, “Urokinase plasminogen activator and its inhibitor, PAI-1, as prognostic markers in breast cancer: from pilot to level 1 evidence studies.,” *Clin. Chem.*, vol. 48, no. 8, pp. 1194–7, Aug. 2002.

[144] H. Pappot, A. N. Pedersen, N. Brünner, and I. J. Christensen, “The complex between urokinase (uPA) and its type-1 inhibitor (PAI-1) in pulmonary adenocarcinoma: Relation to prognosis,” *Lung Cancer*, vol. 51, pp. 193–200, 2006.

[145] H. Taubert *et al.*, “Co-detection of members of the urokinase plasminogen activator system in tumour tissue and serum correlates with a poor prognosis for soft-tissue sarcoma patients,” *Br. J. Cancer*, vol. 102, pp. 731–737, 2010.

[146] S. J. Shin *et al.*, “Expression of E-cadherin and uPA and their Association with the Prognosis of Pancreatic Cancer,” *Jpn. J. Clin. Oncol.*, vol. 35, pp. 342–348, 2005.

[147] E. M. Bekes *et al.*, “Activation of Pro-uPA is Critical for Initial Escape from the Primary Tumor and Hematogenous Dissemination of Human Carcinoma Cells,” *Neoplasia*, vol. 13, pp. 806–821, 2011.

[148] “Cancer,” *World Health Organization*, 2018. [Online]. Available: https://www.who.int/news-room/fact-sheets/detail/cancer.

[149] C.-H. Lu, H.-H. Yang, C.-L. Zhu, X. Chen, and G.-N. Chen, “A Graphene Platform for Sensing Biomolecules,” *Angew. Chemie*, vol. 121, pp. 4879–4881, 2009.

[150] W. Yang, K. R. Ratinac, S. R. Ringer, P. Thordarson, J. J. Gooding, and F. Braet, “Carbon Nanomaterials in Biosensors: Should You Use Nanotubes or Graphene?,” *Angew. Chemie - Int. Ed.*, vol. 49, pp. 2114–2138, 2010.

[151] J. H. Jung, D. S. Cheon, F. Liu, K. B. Lee, and T. S. Seo, “A Graphene Oxide Based Immuno-biosensor for Pathogen Detection,” *Angewandte Chemie - International Edition*, vol. 122. pp. 5844–5847, 2010.

[152] E. Morales-Narváez and A. Merkoçi, "Graphene Oxide as an Optical Biosensing Platform," *Adv. Mater.*, vol. 24, pp. 3298–3308, 2012.

[153] S. Eustis and M. A. El-Sayed, "Why gold nanoparticles are more precious than pretty gold: Noble metal surface plasmon resonance and its enhancement of the radiative and nonradiative properties of nanocrystals of different shapes," *Chem. Soc. Rev.*, vol. 35, pp. 209–217, 2006.

[154] P. K. Jain, X. Huang, I. H. El-Sayed, and M. A. El-Sayed, "Review of Some Interesting Surface Plasmon Resonance-enhanced Properties of Noble Metal Nanoparticles and Their Applications to Biosystems," *Plasmonics*, vol. 2, pp. 107–118, 2007.

[155] R. M. Williams, C. Lee, and D. A. Heller, "A Fluorescent Carbon Nanotube Sensor Detects the Metastatic Prostate Cancer Biomarker uPA," *ACS Sensors*, vol. 3, pp. 1838–1845, 2018.

[156] B. Sharma, S. Chiluwal, and R. Podila, "Analyte-induced disruption of luminescence quenching (AIDLuQ) for femtomolar detection of biomarkers," *Nanoscale*, vol. 11, pp. 14010–14015, 2019.

[157] T. C. Ta and M. T. McDermott, "Mapping Interfacial Chemistry Induced Variations in Protein Adsorption with Scanning Force Microscopy," *Anal. Chem.*, vol. 72, pp. 2627–2634, 2000.

[158] M. Lundqvist, J. Stigler, G. Elia, I. Lynch, T. Cedervall, and K. A. Dawson, "Nanoparticle size and surface properties determine the protein corona with possible implications for biological impacts," *PNAS*, vol. 105, pp. 14265–14270, 2008.

[159] S. Grimme, "Semiempirical GGA-Type Density Functional Constructed with a Long-

Range Dispersion Correction," *J. Comput. Chem.*, vol. 27, pp. 1787–1799, 2006.

[160] S. Grimme, J. Antony, S. Ehrlich, and H. Krieg, "A consistent and accurate ab initio parametrization of density functional dispersion correction (DFT-D) for the 94 elements H-Pu," *J. Chem. Phys.*, vol. 132, p. 154104, 2010.

[161] S. Grimme, S. Ehrlich, and L. Goerigk, "Effect of the Damping Function in Dispersion Corrected Density Functional Theory," *J. Comput. Chem.*, vol. 32, pp. 1456–1465, 2011.

[162] "Why is early diagnosis important?," *Cancer Research UK*, 2018. [Online]. Available: https://www.cancerresearchuk.org/about-cancer/cancer-symptoms/why-is-early-diagnosis-important.